# Characterization of MBE-grown Semiconductor Materials

# for Photovoltaic Applications

by

Dinghao Tang

A Dissertation Presented in Partial Fulfillment
of the Requirements for the Degree
Doctor of Philosophy

Approved April 2014 by the
Graduate Supervisory Committee:

David J. Smith, Chair
Peter A. Crozier
Jingyue Liu
Martha R. McCartney

ARIZONA STATE UNIVERSITY

May 2014

ABSTRACT

The research described in this dissertation involved the use of transmission electron microscopy (TEM) to characterize II-VI and III-V compound semiconductor quantum dots (QDs) and dilute-nitride alloys grown by molecular beam epitaxy (MBE) and intended for photovoltaic applications.

The morphology of CdTe QDs prepared by the post-annealing MBE method were characterized by various microscopy techniques including high-resolution transmission electron microscopy (HR-TEM), and high-angle annular-dark-field scanning transmission electron microscopy (HAADF-STEM). Extensive observations revealed that the of QD shapes were not well-defined, and the QD size and spatial distribution were not determined by the amount of CdTe deposition. These results indicated that the formation of II-VI QDs using a post-annealing treatment did not follow the conventional growth mechanism for III-V and IV-IV materials.

The structural properties of dilute-nitride $GaAsN_x$ films grown using plasma-assisted MBE were characterized by TEM and HAADF-STEM. A significant amount of the nitrogen incorporated into the dilute nitride films was found to be interstitial, and that fluctuations in local nitrogen composition also occurred during growth. Post-growth partial relaxation of strain resulted in the formation of {*110*}-oriented microcracks in the sample with the largest substitutional nitrogen composition.

Single- and multi-layered InAs QDs grown on GaAsSb/GaAs composite substrates were investigated using HR-TEM and HAADF-STEM. Correlation between the structural and optoelectronic properties revealed that the GaAsSb barrier layers had played an important role in tuning the energy-band alignments but without affecting the

overall structural morphology. However, according to both XRD measurement and electron microscopy the densities of dislocations increased as the number of QD layers built up.

An investigation of near-wetting layer-free InAs QDs incorporated with AlAs/GaAs spacer layers was carried out. The microscopy observations revealed that both embedded and non-embedded near-wetting layer-free InAs QDs did not have well-defined shapes unlike conventional InAs QDs. According to AFM analysis and plan-view TEM characterization, the InAs QDs incorporated with spacer layers had smaller dot density and more symmetrical larger sizes with an apparent bimodal size distribution (two distinct families of large and small dots) in comparison with conventional InAs QDs grown without any spacer layer.

*This dissertation is dedicated to my parents,*

*Who made everything possible.*

ACKNOWLEDGMENTS

This dissertation could not have been finished without the help and support from many professors, research staff, graduate students, colleagues and my family. It is my great pleasure to acknowledge people who have given me guidance, help and encouragement.

I would like to first express my most sincere gratitude to my advisor, Regents Professor David J. Smith, for his constant guidance, personal attention, endless encouragement and full support during last four years throughout my doctoral study and research at Arizona State University. His enthusiasm towards doing research has greatly impressed, motivated and educated me.

Special thanks go to my dissertation supervisory committee members, Professors Martha McCartney, Jingyue Liu and Peter Crozier, for their generous time and important suggestions and remarks in this research program and their time and effort in service on my doctoral committee despite their already heavy loads of responsibility.

Additionally, I would like to extend my sincere appreciation to my collaborators: Prof. Jacek Furdyna, Dr. Xinyu Liu, Robert Pimpinella at University of Notre Dame, Prof. Alex Freundlich, Gopi Krishna, Manori Gunasekera at University of Houston, and Prof. Christiana Honsberg, Dr. Nikolai Faleev and Yeongho Kim, for their collaboration and providing the samples used for investigation in this dissertation.

I am grateful for the use of facilities in the John M. Cowley Center for High Resolution Electron Microscopy, and I thank Karl Weiss, Dr. Zhenquan Liu, Dr. Toshihiro Aoki and Dr. John Mardinly who gave me enormous valuable discussions, technical support and hands-on assistance in many aspects of my research.

It has been my pleasure to work with many previous students and colleagues in Molly & Dave Gang (MDG). They are Dr. Lin Zhou, Dr. Kai He, Dr. Wenfeng Zhao, Dr. Lu Ouyang, Dr. Luying Li, Dr. Jaejin Kim and Dr. Michael Johnson, Dr. David Cullen, Dr. Lin Gu, Dr. Hua Wang, Sahar Hihath, Aram Rezikyam for their help during my stay. Moreover, I would like to express my gratitude to many current group-mates: Allison Boley, Ajit Dhamdhere, Zhaofeng Gan, Jing Lu, Sirong Lu, Thomas McConkie, Xiaomeng Shen, Brian Tracy, Majid Vaghayenegar and Desai Zhang. We discussed together, exchanged ideas, and helped each other. Those made my years at ASU the most memorable period in my life. I would also like to wish them the best for success in their doctoral studies.

Finally, I would like to express the most heartfelt gratitude to my parents, for their unconditional love and tremendous support throughout years. Without their blessings and encouragement, I would not have accomplished my PhD with so much positiove energy and enthusiasm. My appreciation is beyond description.

TABLE OF CONTENTS

Page

LIST OF TABLES ... x

LIST OF FIGURES ... xi

CHAPTER

1 INTRODUCTION ... 1

1.1 Introduction to solar energy ... 1

1.2 Fundamentals of photovoltatics ... 2

1.3 Fundamentals of solar radiation ... 4

1.4 Energy efficiency of photovoltaic solar cells ... 5

1.5 Intermediate band solar cells ... 7

1.6 Semiconductor photovoltaic materials ... 8

1.7 Selection criteria for semiconductor PV materials ... 10

1.8 III-V photovoltaic materials ... 10

1.9 II-VI photovoltaic materials ... 13

1.10 Modes of thin film growth ... 14

1.11 Outline of dissertation ... 17

2 EXPERIMENTAL PROCEDURES ... 23

2.1 Molecular beam epitaxy ... 23

2.1.1 MBE growth of CeTe QDs on ZnTe/GaSb ... 25

2.1.2 MBE growth of dilute nitride films on GaAs ... 25

2.1.3 MBE growth of self-assembled InAs QDs embedded in $GaAs_{1-x}Sb_x$ epilayers grown on GaAs (001) substrates ... 26

CHAPTER Page

2.1.4 MBE growth of near-wetting layer-free InAs QDs incorporated with AlAs/GaAs spacer layers on GaAs (001) substrates ... 27

2.2 Transmission electron microscopy ... 27

2.2.1 High-resolution transmission electron microscopy ... 27

2.2.2 Scanning transmission electron microscopy ... 28

2.3 Analytical spectroscopy ... 30

2.3.1 Energy-dispersive X-ray spectroscopy ... 30

2.4 TEM sample preparation ... 30

2.4.1 Combined mechanical polishing and dimpling ... 31

2.4.2 Focused ion beam ... 32

3 STRUCTURAL CHARACTERIZATION OF CdTe QUANTUM DOTS GROWN ON ZnTe/GaSb (001) COMPOSITE SUBSTRATES BY MOLECULAR BEAM EPITAXY ... 35

3.1 Introduction ... 35

3.2 Experimental details ... 37

3.3 Results & Discussion ... 38

3.4 Conclusions ... 46

4 MICROSCOPIC INVESTIGATION OF MBE-GROWN DILUTE-NITRIDE ALLOYS OF GaAsNx ($0.01<x<0.04$) ON GaAs FOR PHOTOVOLTAIC SOLAR CELLS ... 50

4.1 Introduction ... 50

4.2 Experimental details ... 51

CHAPTER Page

4.3 Results & Discussion ........ 52

4.4 Conclusions ........ 59

5 INVESTIGATION OF MONOLAYER/MULTI-LAYER InAs QUANTUM DOTS ON $GaAs_{1-x}Sb_x$/GaAs COMPOSITE SUBSTRATES FOR PHOTOVOLTAIC SOLAR CELLS ........ 63

5.1 Introduction ........ 63

5.2 Results & Discussion ........ 65

5.2.1 Characterization of single-layered InAs/GaAsSb QDs ........ 65

5.2.2 Characterization of multi-layered InAs/GaAsSb QDs with different Sb concentration ........ 68

5.2.3 Characterization of multi-layered InAs/GaAsSb QDs with different layer periods ........ 81

5.3 Conclusions ........ 83

6 MICROSCOPIC CHARACTERIZATION OF InAs QUANTUM DOTS INCORPORATED WITH AlAs/GaAs SPACER LAYERS ........ 85

6.1 Introduction ........ 85

6.2 Results & Discussion ........ 86

6.2.1 Characterization of InAs QDs incorporating with AlAs spacer layer ........ 88

6.2.2 Characterization of InAs QDs incorporating with GlAs spacer layer ........ 94

6.3 Conclusions ........ 102

CHAPTER Page

7 SUMMARY AND FUTURE WORK ........................................................... 105

7.1 Summary ........................................................................................ 105

7.2 Future work ..................................................................................... 107

7.2.1 Minimization of ion-milling damage and re-deposition during ion-milling ......................................................................................... 107

7.2.2 Detection and atomic incorporation of nitrogen atoms in dilute-nitride alloys ............................................................................... 108

7.2.3 Interfacial diffusion and intermixing in II-VI and III-V QD systems ........................................................................................... 109

LIST OF REFERENCES....... ........................................................................... 111

LIST OF TABLES

Table Page

1.1 Lattice constant and band gap of elemental and compound semiconductors used in solar PV applications. ..... 9

2.1 JEOL ADF detector range in JEOL-2010F with commonly used camera lengths. ..... 29

2.2 Convergence semi-angles in JEOL-2010F with different condenser lens (CL) apertures. ..... 30

4.1 Growth conditions, nitrogen concentrations measured using XRD, and band gap measured using PL. ..... 52

5.1 Five single-layered InAs/GaAsSb QD structures incorporated with a Si delta layer, with their corresponding responding δ-doping density, intended Sb content and expected type of energy band alignment. ..... 66

5.2 Measurement of Sb content, relaxation and dislocation density for three multi-layered (10×) InAs/GaAsSb QD samples. ..... 73

6.1 Numerical findings of density, mean height, base length and base width of QDs. ..... 88

LIST OF FIGURES

Figure Page

1.1 The electromagnetic spectrum. .................................................................. 4

1.2 Energy conversion from a two-layered stacked PV cell. ............................ 6

1.3 General energy band structure of an intermediate band solar cell.............. 7

1.4 Conversion efficiency of solar cell materials versus band gap for single junction cells. ........................................................................................ 11

1.5 Band gap versus lattice constant for different III-V materials.................. 12

1.6 Band gap versus lattice constant for different II-VI and III-V materials .. 14

1.7 Schematic of cross-sectional views of the three primary modes of thin film growth. (a) Volmer-Weber (VW: island formation), (b) Frank-van der Merwe (FM: layer-by-layer) and (c) Stranski-Krastanov (SK: layer-plus-island) ... ........................................................................................................... 15

2.1 Functional schematic of a basic MBE system ........................................... 24

2.2 Schematic cross-section of a typical MBE growth chamber ...................... 24

3.1 Schematic of sample structure for CdTe QDs on ZnTe/GaSb composite substrates. Upper: capped CdTe QDs. Lower: non-capped CdTe QDs ...... ........................................................................................................... 38

3.2 Electron micrographs of specimen with capped 4.5 ML CdTe QDs. (a) cross-sectional diffraction-contrast TEM image showing CdTe layer (arrowed) grown on ZnTe/GaSb composite substrate and capped by ZnTe layer; (b) plan-view diffraction-contrast TEM image showing broad distribution of shapes and sizes of CdTe QDs; (c) Enlargement from (b) showing several

Figure Page

CdTe QDs with light/dark contrast indicative of interfacial misfit dislocations. ........................................................................................ 40

3.3 Cross-sectional electron micrographs of uncapped 4.5 ML CdTe QDs. (a) phase-contrast XTEM image showing the general QD morphology; (b) XTEM lattice image showing a typical uncapped 4.5 ML CdTe QD with non-facetted shape. ..................................................................................... 41

3.4 (a) Cross-sectional phase-contrast TEM image of sample with capped 6.5 ML CdTe QD layer. Arrow indicates position of CdTe layer. (b) Enlargement showing several {111}-type stacking faults originating at the CdTe layer (see arrow). ................................................................................................ 42

3.5 (a) Plan-view ADF STEM image of capped 6.5 ML CdTe QDs. Regions of brighter contrast correspond to CdTe QDs with non-well-defined shapes. (b) Plan-view diffraction-contrast TEM image: (c) Enlargement from (b). Several QDs show distinctive contrast due to the presence of interfacial misfit dislocations, similar to that seen in Fig. 1(c). ............................. 43

3.6 (a) Diffraction-contrast TEM image of uncapped 6.5 ML CdTe QDs; (b) Secondary electron image of uncapped 6.5 ML CdTe quantum dots; and (c) AFM image of uncapped 6.5 ML CdTe quantum dots. ......................... 44

3.7 (a) Low-magnification HAADF STEM image of capped 4 ML CdTe QDs; (b) higher magnification HAADF STEM image of the left-hand QD in (a); (c) HAADF STEM lattice image of the same QD. ..................................... 45

Figure Page

4.1 (a) Low-magnification HAADF-STEM image of $GaAsN_{0.0144}$ film grown on GaAs. Two interfaces are observed (as labeled by arrows). (b) HAADF image shows buffer-epi interface area. Two interfaces are visible, although the contrast of the upper one is extremely weak. Contrast of epilayer is slightly higher than that of buffer layer. (c) HAADF-STEM lattice image from lower interface region. Brighter contrast but no lattice fringe disruptions. ........................................................................................ 53

4.2 (a) HAADF-STEM image shows two apparent interfaces between the GaAs buffer layer and the GaAsN epilayer. (b) HAADF-STEM image shows that epilayer contrast is slightly brighter than the buffer layer, which would imply that the nitrogen is interstitial. (c) HAADF-STEM image showing interface region. Brighter lower interface indicates overall higher atomic number material. ........................................................................................ 54

4.3 (a) Conventional phase-contrast TEM image reveals variations in contrast in $GaAsN_x$ epilayer, whereas the contrast in the GaAs buffer layer is uniform by comparison. (b) HAADF-STEM image shows uniform contrast but local changes in contrast are visible in the $GaAsN_x$ epilayer. (c, d) HAADF-STEM lattice images of the interface region...................................................... 55

4.4 (a) HAADF-STEM image shows a typical microcrack present in the epilayer, as sometimes observed in this highly N-doped $GaAsN_x$, which is attributed to the extra strain. (b, c) HAADF-STEM lattice images show interface region. ........................................................................................................ 56

Figure Page

4.5 (a) Structure schematic of dilute-nitride $GaAsN_x$ quantum-well-based solar cell. (b) HAADF-STEM image shows cross-section image showing upper part of fabricated solar cell with layers corresponding to the sample schematic. (c) HAADF-STEM lattice image showing the enlarged region of AlGaAs epilayer. (d) HAADF-STEM image showing four periods of the dilute-nitride asymmetric QW layers. (e) HAADF-STEM lattice image showing an enlarged view of one typical period of the dilute-nitride layer. ........ 57

4.6 PL spectrum from the dilute-nitride $GaAsN_x$ QW-based solar cell. ........ 58

5.1 Structural schematic of single-layered InAs/GaAsSb QD substrates......... 66

5.2 High-resolution HAADF-STEM image of self-assembled single-layered InAs QDs on GaAsSb/GaAs. ........ 67

5.3 Structural schematic of multi-layered (10×) InAs/GaAsSb QD samples. 68

5.4 XRD pattern (blue curve) of sample G13-069 using double crystal ω-2θ scan with its corresponding simulated pattern (red curve) ........ 69

5.5 XRD pattern of sample G13-070 using double crystal ω-2θ scan with its corresponding simulated pattern (red curve)........ 69

5.6 XRD pattern of sample G13-071 using double crystal ω-2θ scan with its corresponding simulated pattern (red curve). ........ 70

5.7 XRD patterns for three multi-layered InAs QD samples (G13-069, G13-070, G13-071) using double crystal ω-2θ scans. ........ 70

Figure Page

5.8 XRD patterns of samples G13-069 (blue), G13-070 (red) and G13-071 (green) used for determining dislocation densities. ........................................... 72

5.9 XRD reciprocal space maps based on (224) asymmetric scan for samples (a) G13-069, (b) G13-070, and (c) G13-071 .............................................. 72

5.10 (a) HAADF-STEM image showing sample 069 with 10 periods of self-assembled InAs QDs on $GaAs_{0.93}Sb_{0.07}$ barrier layers; (b) HAADF-STEM image showing sample 070 owith 10 periods of self-assembled InAs QDs on $GaAs_{0.90}Sb_{0.10}$ barrier layers; (c) HAADF-STEM image showing sample 071 with 10 periods of self-assembled InAs QDs on $GaAs_{0.85}Sb_{0.15}$ barrier layers. ........................................................................................................ 74

5.11 HAADF-STEM image showing a single column of self-assembled InAs QDs on $GaAs_{0.93}Sb_{0.07}$ barrier layers. .......................................................... 75

5.12 HAADF-STEM images showing ten well-aligned InAs QDs on $GaAs_{0.93}Sb_{0.07}$ in the specific QD column observed in Fig. 5.11. .......... 76

5.13 (a) HR-TEM image showing sample 069 with 10 periods of self-assembled InAs QDs on $GaAs_{0.93}Sb_{0.07}$ barrier layers; (b) HR-TEM image showing sample 070 with 10 periods of self-assembled InAs QDs on $GaAs_{0.90}Sb_{0.10}$ barrier layers; (c) HR-TEM image showing sample 071 with 10 periods of self-assembled InAs QDs on $GaAs_{0.85}Sb_{0.15}$ barrier layers. .................. 78

5.14 cw-PL spectra of samples 069 (black curve), 070 (red curve) and 071 (blue curve) recorded at 10 K. Peak shift to lower energy corresponds to longer wavelength emission. ................................................................... 79

Figure Page

5.15 Power-dependent PL spectras of samples (a) 069, (b) 070 and (c) 071. ...... ........................................................................................................ 80

5.16 Structural schematic of multi-layered InAs/$GaAs_{0.8}Sb0_{.2}$ QDs with different numbers of QD stacks. ............................................................................ 81

5.17 HAADF-STEM image of 5× InAs/$GaAs_{0.8}Sb_{0.2}$ QDs............................ 82

5.18 HAADF-STEM image of 20× InAs/$GaAs_{0.8}Sb0_{.2}$ QDs .......................... 83

6.1 (a) RHEED pattern for conventional InAs QDs on GaAs (100) (b) RHEED pattern for InAs QDs incorporated with GaAs spacer layer on GaAs (100). ........................................................................................................ 87

6.2 (a) AFM image showing conventional InAs QDs grown on GaAs (100). (b) AFM image showing InAs QDs incorporated with 3 ML GaAs spacer layer on GaAs (100). (c) AFM image showing InAs QDs incorporated with 3 ML AlAs spacer layer on GaAs (100). Scales of three AFM images are 0.05 µm × 0.05 µm. ...................................................................................... 88

6.3 Structural schematic of sample #1 containing embedded conventional SK-type InAs QDs, embedded VW-type InAs QDs incorporated with AlAs spacer layer, and uncapped VW-type InAs QDs incorporated with AlAs spacer layer. ................................................................................................ 89

6.4 HR-TEM image of sample #1 containing uncapped VW-type InAs QDs (1st layer), capped near-wetting layer-free InAs QDs (2nd layer) and conventional embedded SK-type InAs QDs (3rd layer)........................ 90

Figure Page


6.5 (a) Low-magnification HAADF-STEM image showing the structure of sample #1. (b) EDS line-scan profile along the direction of blue arrow in (a). . 91

6.6 (a) Medium-magnification HAADF-STEM image showing the embedded near-wetting layer-free InAs QDs and embedded conventional SK-typed QDs. (b) HAADF-STEM lattice image showing the AlAs spacer layer for near-wetting layer-free InAs QDs. ........................................................ 92

6.7 (a) Medium-magnification HAADF-STEM image showing embedded InAs QDs incorporated with AlAs spacer layer. (b) Medium-magnification HAADF-STEM image showing conventional embedded InAs QDs..... 93

6.8 (a) Diffraction-contract TEM image showing typical near-wetting layer-free InAs QD incorporated with AlAs spacer layer (upper) and conventional SK-type InAs QD (lower). (b) TEM image showing a typical conventional SK-type InAs QD with <111> stacking fault and dislocation. ..................... 94

6.9 Structural schematic of sample #2 containing embedded VW-type InAs QDs incorporated with GaAs spacer layer, and uncapped VW-type InAs QDs incorporated with GaAs spacer layer. ................................................... 95

6.10 Low-magnification HAADF-STEM image of sample #2 containing embedded VW-type InAs QDs incorporated with GaAs spacer layer, and uncapped VW-type InAs QDs incorporated with GaAs spacer layer. ................... 96

6.11 (a) Medium-magnification HAADF-STEM image of embedded InAs QDs. (b) Medium-magnification TEM image of embedded InAs QDs ......... 97

Figure Page

6.12 (a) HAADF-STEM image showing the uncapped InAs QDs with size variation; (b) HAADF-STEM lattice image showing a typical InAs QD; (c) HAADF-STEM lattice image showing a typical InAs QD overlapping with a bigger QD. ........................................................................................ 99

6.13 (a) TEM image showing the near-wetting layer-free InAs QDs incorporated with GaAs spacer layer. (b) HR-TEM image showing the left QD on (a). (c) HR-TEM image showing the right QD on (a). (d) HR-TEM image showing a typical dislocation in the larger InAs QDs incorporated with GaAs spacer layer.............................................................................................. 101

6.14 (a) Plan-view TEM image showing the near-wetting layer-free InAs QDs incorporated with GaAs spacer layer. (b) Plan-view HAADF-STEM image showing the near-wetting layer-free InAs QDs incorporated with GaAs spacer layer. ........................................................................................ 102

# CHAPTER 1

# INTRODUCTION

## 1.1 Introduction to solar energy

Energy is required for a wide range of applications in industry, agriculture, household, and transportation, in various forms such as heat energy, electrical energy, chemical energy, nuclear energy and so on. Among these, electrical energy is the most convenient since it can be easily converted to many other forms of energy, and it is the most versatile from the point of view of transmission, distribution and control.

With the rapid increase in energy usage since the 1800s, the trend in energy consumption has become neither secure nor sustainable over the past several decades. The rising consumption of fossil fuels (coal and petroleum) has generated increasing amounts of greenhouse gases that impact our surroundings and the global environment.[1] The emission of harmful gases due to fossil-fuel consumption also threatens the health of all living species including human beings. In addition, the finite supply of fossil energy resources is widely recognized. Therefore, developing clean, secure, sustainable and affordable energy sources is a high priority in this century. With this goal in mind, many possible sources in terms of renewable energy, as alternatives to fossil fuels, have been explored, including wind, biomass, solar thermal, and solar photovoltaics (PV).[1-3]

Solar energy is the obvious source for supplying clean energy, and it also has many advantages over conventional energy sources. Some advantages of using solar energy are listed below:[3]

- Solar energy is inexhaustible and renewable.
- Solar energy is clean, and has no potential for damage to the environment.

- Solar energy is the largest accessible source of energy on our planet. It amounts to about $1.8 \times 10^{11}$ MW, which is many thousands of times greater than current power consumption from all sources.
- Solar energy is free, and widely available compared with the uneven distribution of coal and petroleum.

These advantages of solar energy provide sufficient motivation for pursuing the conversion of solar energy into controllable and useful energy forms such as electricity.

The most well developed solar energy source so far is solar thermal energy, which is the technology used for converting solar energy to thermal energy (heat).[2] In this process, solar radiation is first converted into heat by using solar thermal collectors, and that heat is then further used to run heat engines, which turn generators to make electricity. Due to installation limitations, costs, and conversion efficiency, more effective ways of converting solar energy into electricity need to be investigated.

## 1.2 Fundamentals of photovoltatics

The photovoltaic (PV) effect is direct conversion of energy from sunlight to flow of electrons.[2] In contrast to solar thermal technology, photovoltaic solar cells do not require intermediate heat engines, hence they are expected to have higher energy efficiency. The operation of solar cells behind the PV effect involves two key processes. The first is generation of charge carriers (electron-hole pairs) due to the absorption of incident photons. The second is separation of the charge carriers by a *p-n* junction, which prevents recombination of the electron-hole pairs.[2]

Commercial solar cells in the current PV market are dominated by bulk crystalline silicon (*c*-Si),[4] partly due to the prominence of silicon in the semiconductor industry. However, silicon does not have the optimum parameters for PV applications, particularly because the Si band gap ($E_g$ ~ 1.1 eV) is indirect, and slightly below the ideal value (~1.5 eV) for PV solar cells, which results in a low absorption coefficient. This low absorption can be improved by light trapping and surface passivation, but requires the solar cell material to be about 100μm thick. Thicknesses between 200 μm and 500 μm are normally used, due to practical issues in making and handling the *c*-Si wafers. The continuously increasing demand for PV modules and the need for low-cost PV options have exposed several inherent disadvantages of bulk *c*-Si technology, such as the scarcity of source material and the costly expense of materials processing and device fabrication. It is generally accepted that bulk *c*-Si solar PV technology will be unable to achieve the low-cost goal, whereas thin-film PV technologies have the potential to serve as viable alternatives in the near future.[5] From the large variety of materials under consideration in the 1950s, only four thin-film technologies, namely amorphous (*a*-) hydrogen-alloyed Si:H and the polycrystalline heterojunction systems $CdS/Cu_xS$, CdS/CdTe, and $CdS/CuInSe_2$, have entered pilot production.[4,5] $CdS/Cu_xS$ PV system stopped being produced in early 1980s due to stability problems, while (*a*-) Si:H became the front runner in thin-film PV technologies with about 10% of total PV market, with 90% kept by bulk crystalline Si. Despite the high-efficiency potential, heterojunction $CdS/Cu_xS$, CdS/CdTe systems failed to have an important impact until the turn of this century.

## 1.3 Fundamentals of solar radiation

In order to design high-efficiency PV solar cells, the properties of sunlight need to be understood, particularly that part of the solar spectrum that is incident on the earth surface. Sunlight consists of electromagnetic radiation and visible light is only a small fraction of the solar spectrum, as shown in figure 1.1.

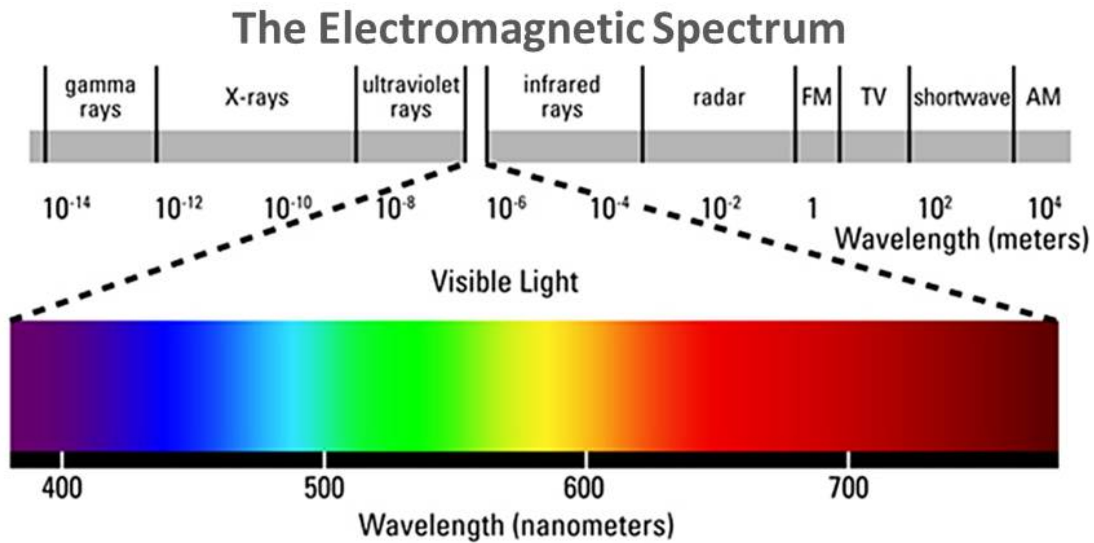


Fig. 1.1 The electromagnetic spectrum.[6]

Photons are characterized in terms of wavelength (λ) or equivalently energy (E). The relationship between the wavelength and energy of a photon is given by the expression.[2]

$$E = \frac{hc}{\lambda} \tag{1.1}$$

where h is Planck's constant and c is the speed of light. The values of these constants are $h=6.63\times10^{-34}$ joule·s, $c=3.00\times10^{8}$ m/s. The commonly used unit of energy for photons is the electron-volt (eV), which is the energy required to raise an electron through a potential of 1 volt. By expressing the equation for photon energy in units of eV and μm,

the commonly used expression which relates the energy and wavelength of a photon can be derived, as shown in the following:[2]

$$E\ (eV) \approx \frac{1.24}{\lambda\ (\mu\text{m})} \tag{1.2}$$

1.4. Energy efficiency of photovoltaic solar cells

The major constraint on the efficiency of PV solar cells is related to the band gap of the PV material. In simple terms, a photon of light with energy equal to or larger than the band gap of the PV material is able to excite a single electron when it is absorbed into the material. However, photons that have energy less than the material band gap are not useful for generating electricity. The excess energy is simply converted into heat, which warms up the PV device. The actual efficiencies of PV solar cells is lower than theoretical values because of other constraints, such as the reflection of light from the cell surface, shading of the cell due to current-collecting contacts, internal resistance of the cell, and the recombination of electrons and holes before they are extracted as electrial current.

The maximum energy conversion efficiency ($\eta$) of a PV solar cell consisting of single semiconductor material layer with band gap energy $E_g$ can be described by the Shockley-Queisser (SQ) limit,[7] which is

$$\eta = \frac{-\max\left(J(V)V\right)}{P_{opt}} = \frac{-\max\left(J(V)V\right)}{\int_0^{\infty} E\phi_{sun}(E)dE} \tag{1.3}$$

The limit imposed by the band gap of the PV material can be partially overcome by using multilayered structures, with the composition of each layer having a band gap higher than the layer beneath it. Taking a binary-layer solar cell for example as

illustrated in Fig. 1.2:[8] if the top layer is made of composition A (band gap corresponding to $\lambda_A$) and the bottom layer is made of composition B (band gap corresponding to $\lambda_B$, and $\lambda_A<\lambda_B$), the solar radiation with wavelengths less than $\lambda_A$ would be absorbed to give output equal to the hatched area A. Solar radiation with wavelength greater than $\lambda_A$ would pass through A and be converted to give an output equal to the hatched area B. The total output and hence the efficiency of this tandem cell would be higher than the output and efficiency of each individual cell. Theoretically, efficiencies above 50% could be easily achieved for a multijunction cell, which is much higher than for a corresponding single cell. The efficiency could also increase with the number of layers, by extending the radiation absorption to cover more of the solar spectrum. For this concept to work in practice, the absorber material of an actual PV cell requires that each layer must be as thin as possible in order to allow all solar radiation to penetrate the absorber, although this makes for a difficult process for fabricating the desired absorber PV material.

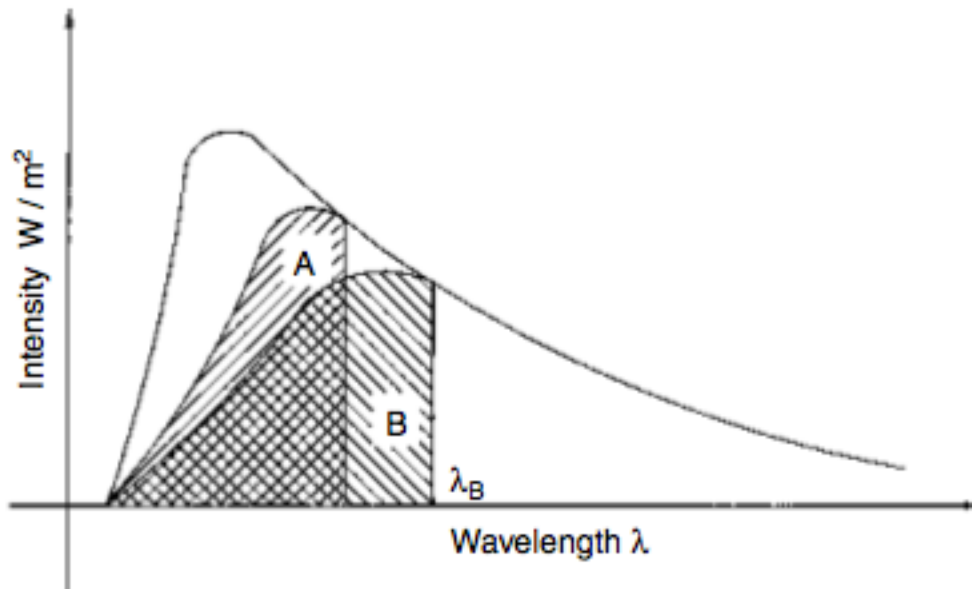


Fig. 1.2 Energy conversion from a two-layered stacked PV cell.[8]

## 1.5 Intermediate band solar cells

The intermediate band solar cell (IBSC) is designed to provide a large photogenerated current while maintain a high output voltage. It aims to exploit the energy of below-bandgap-energy photons using an additional energy band located in between the conduction and valence band. Figure 1.3 sketches the basic structure of an IBSC that consists of the so-called intermediate band material sandwiched between conventional p- and n-type semiconductors (emitters). The intermediate band material functions via the existence of a set of energy levels located inside the semiconductor bandgap and separated from the conduction band (CB) and valence band (VB) by a null density of states.

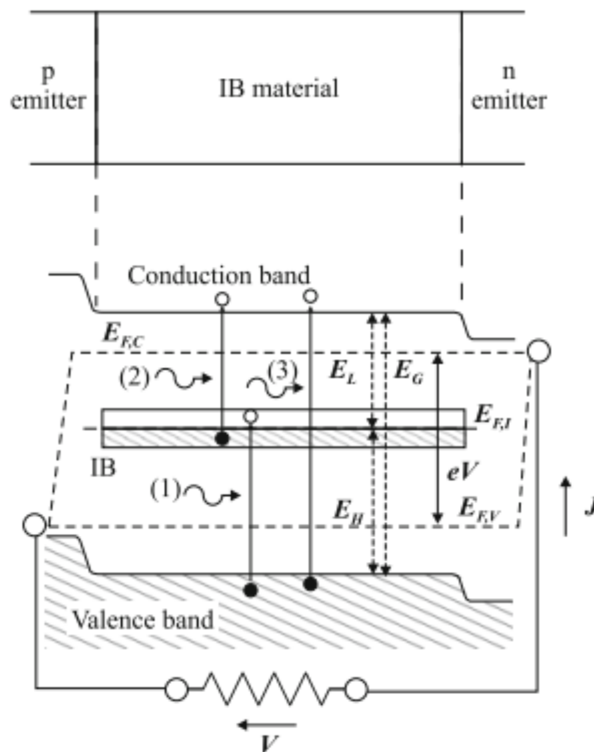


Fig. 1.3 General energy band structure of an intermediate band solar cell.

## 1.6 Semiconductor photovoltaic materials

The interaction between solar radiation and matter as well as the energy conversion process itself depend heavily on the material properties. PV conversion requires an increase in potential energy of the electron, which requires that the PV material possesses charge that can be extracted as output before electron-hole recombination occurs. In this regard, metals and insulators cannot be utilized for PV applications because metals have continuous energy bands, while the energy bands in insulators are too far apart so that any solar photons that reach the PV material surface do not have enough energy to excite electrons to higher energy levels.

Energy bands in semiconductors are separated from each other in the desired manner. Their conductivities fall between those of metals and insulators, and their band gaps vary with changes in composition. Adding impurities or integrating different compositions, so-called band-gap engineering, makes them suitable for various optoelectronic applications such as photovoltaics.

Semiconductor materials that are formed from elements in group-II to group-VI in the Periodic Table are of interest to solar photovoltaics. Semiconductors can be classified into elemental and compound categories. The former are composed of a single species of a group-IV element, such as Si or Ge. The latter are combinations of more than one different species in group-III and group-V or group-II and group-VI, such as GaAs (binary compound), InGaAs (ternary compound) and AlInGaAs (quaternary compound). The large variety of semiconductors provides great flexibility and range in terms of their electrical transport (conductivity, mobility, drift velocity, carrier lifetime, etc.) and optical properties (absorption, radiation, reflection, transmission, plasmonic, etc), while

their variable band gaps serve a central role in the photo-to-electricity conversion process. The band gaps of common elemental and compound semiconductors are summarized in Table 1.1. These different materials with desirable band gaps are being investigated for making multijunction PV solar cells.

Table 1.1: Lattice constant and band gap of elemental and compound semiconductors used in solar PV applications.

| Element or Compound | Name | Lattice constant (A) | Band gap (eV) |
|---|---|---|---|
| **Elemental** | | | |
| **Si** | Silicon | 5.430 | 1.12 |
| **Ge** | Germanium | 5.646 | 0.66 |
| **Binary compound** | | | |
| **GaAs** | Gallium arsenide | 5.653 | 1.42 |
| **InAs** | Indium arsenide | 6.058 | 0.36 |
| **CdTe** | Cadmium telluride | 6.482 | 1.56 |
| **GaN** | Gallium nitride | 5.186 | 3.4 |
| **Ternary compound** | | | |
| **$Al_xGa_{1-x}As$** | Aluminum gallium arsenide | 5.653-5.661 | 1.42 - 2.16 |
| **Quaternary compound** | | | |
| **InAlGaAs** | Indium aluminum gallium arsenide | 5.653-6.058 | 0.35-2.16 |

## 1.7 Selection criteria for semiconductor PV materials

The criteria for the selection of PV materials can be subdivided into physical and technical:[9]

(i) suitable band gap of $1.0 < E_g < 2.0$ eV;

(ii) high absorption coefficient $\alpha$ ($h\nu > E_g$) $> 5 \times 10^4$ $cm^{-1}$;

(iii) lifetime / mobility, respectively, drift lengths / diffusion lengths of minority carriers ($X_s$, $L > 2/\alpha$);

(iv) low surface recombination velocity and/or suitability for passivation of surface states;

(v) suitability for *n*- or *p*-type doping;

(vi) availability of necessary elements;

(vii) suitability for deposition on inexpensive substrates;

(viii) reproducibility of deposition process;

(ix) energy balance/energy pay-back time;

(x) safety issues during production and operation of devices.

## 1.8 III-V photovoltaic materials

Silicon has been investigated extensively in academia and industry for PV applications, but from the solid-state-physics point of view, Si is not the ideal material for PV conversion because it is an indirect-gap semiconductor so that light absorption is much weaker. According to the curve of efficiency versus band gap (Fig. 1.4), it can be seen that silicon is not at the maximum but GaAs is relatively close.[10] It has been shown

that it takes only 1 μm of GaAs (a direct band gap semiconductor) to achieve 90% light absorption compared with 100 μm of Si. [10]

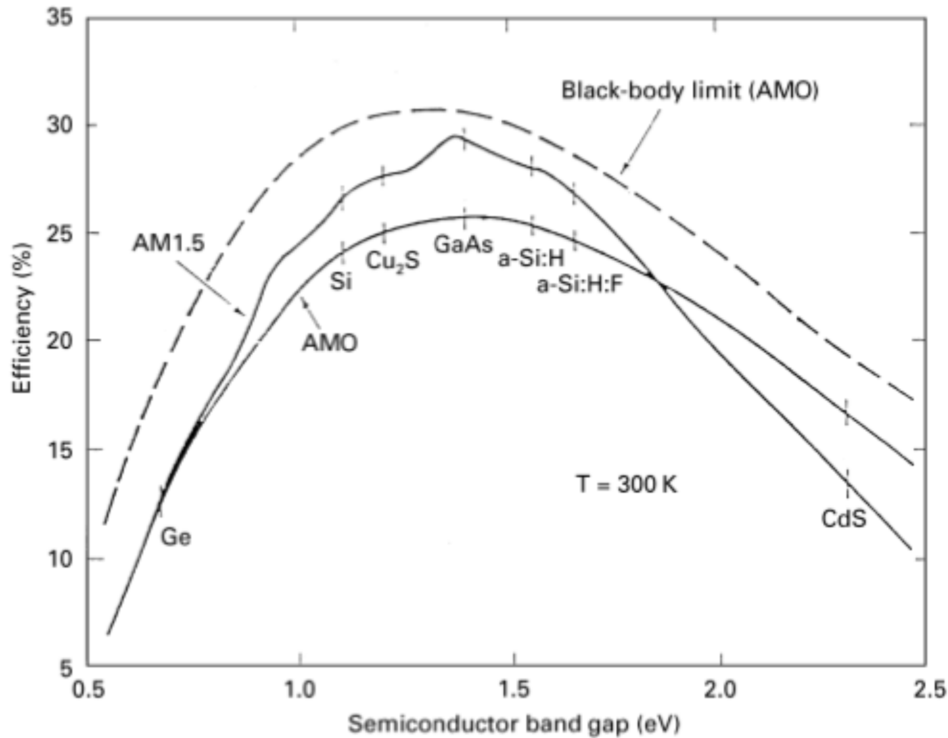


Fig.1.4 Conversion efficiency of solar cell materials versus band gap for single junction cells.[10]

III-V semiconductor materials, such as GaAs and related compound alloys, have higher theoretical and practical efficiencies than Si.[11] e.g. GaAs has already shown an efficiency of 28.8% compared to 25.0% in the case of Si.[12] III-V semiconductor devices have almost completely replaced silicon as the major component for space flat-PV modules.[11] In addition, the broad spectrum of ternary and quaternary III-V compounds, that can be grown lattice-matched on GaAs or Ge substrates, offers a wide range of band-gap possibilities for mono-/multi- junction solar cells, as shown in Fig. 1.5.[13]

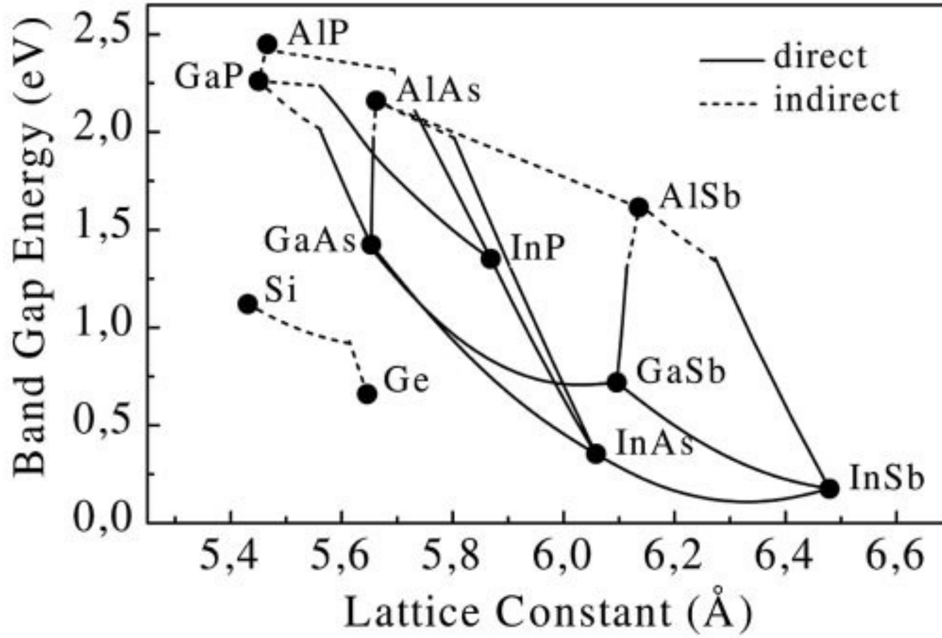

Fig.1.5 Band gap versus lattice constant for different III-V materials.[13]

As an important member of the III-V semiconductor family, GaAs and its ternary and quaternary alloys compounds possess desirable electronic properties that are superior to those of Si for photovoltaic applications.[14] GaAs has a direct band gap of 1.42 eV and allows absorption of the entire solar spectrum in a thickness of less than 3 μm[11]. However, compared with Si, PV applications using III-V semiconductors have experienced slower development due to the difficulties of material growth and device optimization. The first GaAs solar cells with an efficiency of 3% were developed in 1960,[11] and the first important GaAs PV application was achieved in space: the Russian spacecrafts Venera-2 and Venera-3 reached Venus in 1964 and were powered by GaAs solar cells.[11] The difficulties in III-V crystal growth technologies prevented III-V development until the 1980s, when epitaxial deposition techniques such as metalorganic vapor phase epitaxy (MOVPE) and molecular beam epitaxy (MBE) began to be used extensively to deposit thin films on GaAs and Ge substrates following the pioneering work of Manasevit *et al.*

on GaAs using MOVPE.[15] Several years later, more complex heterostructures based on arsenide and phosphide multijunction solar cells were developed. Important improvements achieved in the 1990s permitted the 20% efficiency rate to be surpassed and provided a significant boost in satellite power sources. By the end of the year 2000, the 30% efficiency goal was reached using a triple-junction InGaP/GaAs/Ge device. Nowadays, III-V based multijunction solar cells have already shown efficiencies beyond 40% and are expected to reach the 45% barrier in the near future.[12]

## 1.9 II-VI photovoltaic materials

The use of II-VI compounds and their ternary/quaternary alloys in thin film layers is another promising approach to economically viable photovoltaic solar cells. The II-VI compounds crystallize primarily in the zincblende and wurtzite structures and polymorphic modifications between the two. Many common II-VI compounds have zincblende crystal structure in epitaxial growth, with lattice parameters ranging from 0.567 nm (ZnSe) to 0.648 nm (CdTe) ,[16] as shown in Fig.1.6.

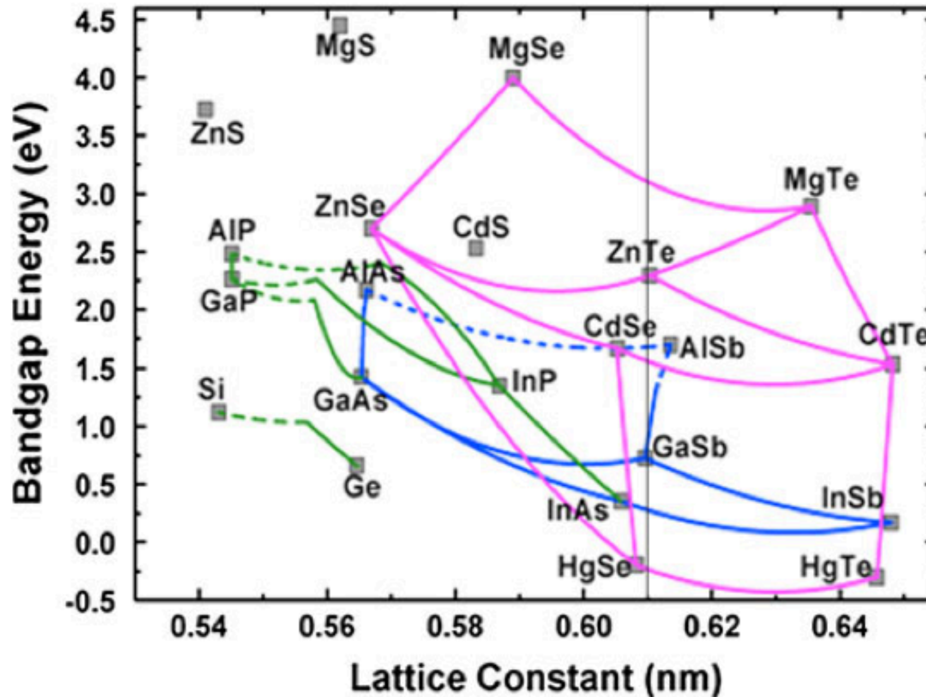

Fig. 1.6. Band gap versus lattice constant for different II-VI and III-V materials.[16]

Most group II–VI materials are direct band gap semiconductors with high optical absorption and emission coefficients. Cadmium telluride (CdTe) is a leading candidate for solar cell applications. CdTe is a direct band gap (1.45 eV) semiconductor and it has high optical absorption coefficient. A thin film of CdTe with thickness of ~ 2 μm will absorb nearly 100% of the incident solar radiation.[17] CdTe and other II-VI compounds can be easily deposited by several methods including vacuum evaporation, electrodeposition, PVD/CVD and MBE.[18]

## 1.10 Modes of thin film growth

In order to fabricate multijunction PV solar cells, understanding and controlling the growth of the heterostructured semiconductor thin film is critical. The growth of

epitaxial thin films on a single crystal surface depends critically on the interaction strength between adatoms and the surface. Most epitaxial growth occurs via a vapor-phase technique such as molecular beam epitaxy (MBE). Heteroepitaxial growth of thin films can be classified in three primary modes by which thin films grow epitaxially at a crystal surface or interface, Volmer-Weber (VW) mode (or 3D island), Frank-van der Merwe (FM) mode (or layer-by-layer), and Stranski-Krastanow (SK) mode (or 3D island-on-wetting-layer growth).[19] The basis of each growth mode is illustrated in figure 1.7, which is a schematic showing these three primary modes of thin film growth.

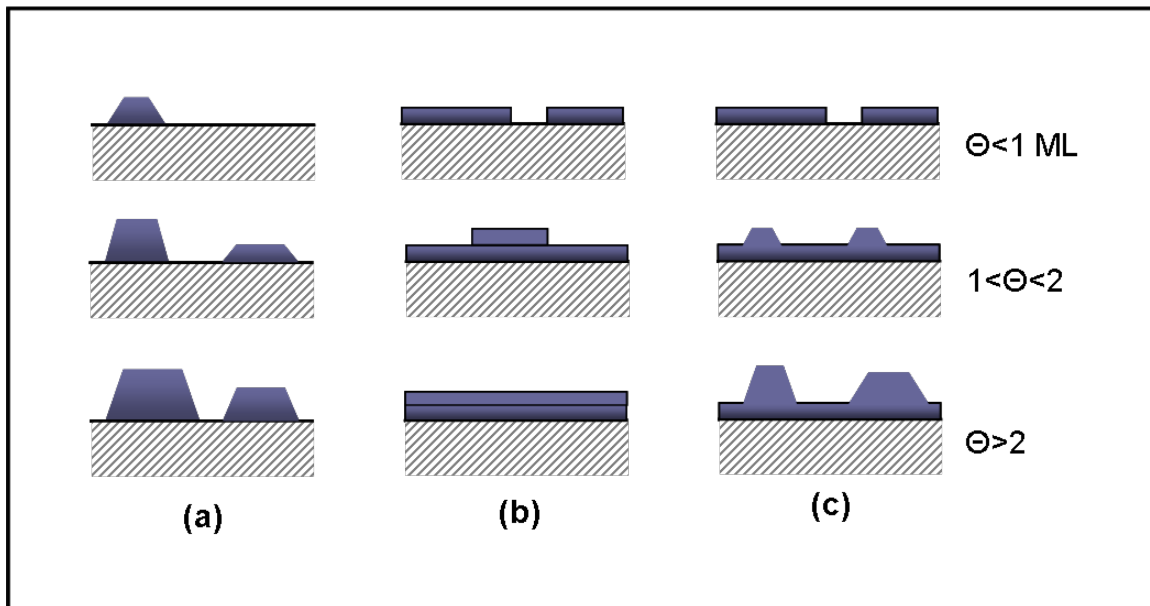


Fig.1.7. Schematic of cross-sectional views of the three primary modes of thin film growth.[20] (a) Volmer-Weber (VW: island formation), (b) Frank-van der Merwe (FM: layer-by-layer) and (c) Stranski-Krastanov (SK: layer-plus-island).

The surface/interface morphology of epitaxial thin films is highly dependent on the lattice parameters of the materials, and lattice mismatch has a marked effect. The strain resulting from lattice mismatch contributes to the interfacial energy, which is a key parameter in determing the growth mode. Additionally, the surface free energies for the

substrate and film material affect the growth mode. In VW mode, adatom-adatom interactions are stronger than those of the adatom with the surface, leading to the formation of three-dimensional adatom clusters or islands.[21] Growth of these islands will cause rough multi-layer films to grow on the substrate surface. In FM mode, the interatomic interactions between substrate and epitaxial film are stronger than those between the atomic species, which is the opposite of the VW mode. SK mode occurs for interaction strengths somewhere between the VW and FM modes.[22]

The energetics of film growth can be described in a simple form under the assumption of equilibrium between the film components in the gas phase and those on the film surface. In this formalism, layer-by-layer growth of A on B requires that: [21]

$$\Delta\gamma = \gamma_A + \gamma_i - \gamma_B$$

where $\gamma_A$ and $\gamma_B$ are the surface free energies of A and B, respectively, and $\gamma_i$ the interfacial free energy. The latter quantity depends on the strain and the strength of chemical interactions between A and B at the interface. This equation means in effect that the sum of the film surface energy and the interface energy must be less than the surface energy of the substrate in order for wetting to occur. Alternatively, it becomes easier for layer-by-layer growth to occur as the surface energy of the substrate increases. Thus, FM growth is expected when this equation is obeyed. However, the strain energy, which is a term in $\gamma_i$, increases linearly with the number of strained layers. At some critical thickness, $\gamma_A$+$\gamma_i$ exceeds $\gamma_B$ and the growth mode transforms from FM to SK resulting in 3D islands on top of the 2D wetting layer. Alternatively, $\gamma_A$ may be sufficiently in excess of $\gamma_B$ that this condition is never fulfilled even for a strong attractive interaction between A and B and little strain ($\gamma_i$<0). In this case, 3D islands nucleate from the onset, resulting

in VW growth. Finally, in the limit of zero lattice mismatch and weak chemical interactions between A and B at the interface ($\gamma_i \cong 0$), the growth mode is determined entirely by the surface free energies of the film and substrate material.[22]

The growth of most heterostructural thin films follow the FM mode. However, the formation of lattice-mismatched QDs is dominated by either SK or VW mode. Controlling the growth mode in epitaxial growth is critical for modifying the structural and compositional integration of heterostructural thin films, which further tunes the materials properties. All the studies of QDs formations presented in this dissertation are closely related to the growth mode of SK or VW. Detailed investigations are discussed in the following chapters.

## 1.11 Outline of dissertation

Material and device characterization becomes an important task not only for quality control in the expanding PV industry but it also remains at the very heart of research and development of future PV materials. This doctoral research concentrates on TEM characterization of MBE-grown semiconductor materials and devices, especially II-VI and III-V compound semiconductor thin films and multilayers, for fabricating PV solar cells.

In chapter 2, essential information about molecular beam epitaxy (MBE), is provided. TEM and related spectroscopy techniques are briefly introduced. The sample preparation methods for TEM characterization involved in this research are also described.

In chapter 3, a systematic investigation of CdTe QDs on ZnTe/GaSb composite substrate, as a function of CdTe wetting layer deposition thickness is presented. CdTe QDs, with or without ZnTe capping layers, have been grown by MBE using composite substrates consisting of ZnTe epilayers deposited on GaSb(001) substrates. The CdTe layers were deposited at 280°C using alternating Cd and Te deposition and the total CdTe deposition thickness was varied in the range from 3 to 7.5 monolayers. QD formation was then induced by desorption of an amorphous Te overlayer after annealing at 300°C. Cross-sectional electron microscopy enabled the shapes of the CdTe QDs to be determined, and indicated that the QDs generally had irregular or poorly defined morphology regardless of the CdTe deposition thickness and the presence or absence of the ZnTe capping layer. Plan-view observations were also used to investigate the morphology and surface density of the CdTe QDs, and it was confirmed that the dots had very high densities and not-well-defined shapes, consistent with the cross-sectional observations.

In chapter 4, a detailed investigation of dilute-nitride $GaAsN_x$ thin films using electron microscopy is described. Dilute-nitride $GaAsN_x$ epilayers were grown on GaAs (001) substrates at temperatures of ~450 ˚C using a radio-frequency plasma-assisted M/CBE system. The nitrogen concentration incorporated into the films according to X-ray diffraction varied in the range between 0.01 and 0.04. High-resolution electron microscopy was used to determine the cross-sectional morphology of the epilayers, and Z-contrast imaging showed that the incorporated nitrogen was primarily interstitial. {110}-oriented micro-cracks, which were associated with the relaxation of strain, were observed in the sample with the highest N concentration ([N]~3.7%). Additionally, Z-

contrast imaging indicated the formation of thin, high-N quantum-well-like layers associated with initial ignition of the N-plasma. Significant N contamination of the GaAs barrier layers was observed in all samples, and could severely affect the carrier extraction and transport properties of targeted devices. Dilute-nitride quantum-well-based photovoltaic solar cells having a bandgap energy of 1.19 eV attributable to the dilute-nitride layer were studied.

In chapter 5, an extensive study investigating the structure-performance properties of single-layered and multi-layered InAs/$GaAs_{1-x}Sb_x$ QD system as a function of varying Sb concentrations and layer periods is presented. Three groups of InAs/$GaAs_{1-x}Sb_x$ QD samples with different Sb concentration and number of layers were grown on (001) undoped GaAs substrates via Stranski-Krastanov growth mode. It was found that the residual strain of the InAs QDs could be partially offset by GaAsSb barrier layers. However, the dislocation density increases as the number of QD layers builds up, according to both XRD measurement and electron microscopy. Additionally, the shape of the InAs QDs evolved from well-defined to not-well-defined, which was attributed to residual strain beneath the QDs, which may be the starting point for generating defects that would further degrade the performance of the QD-based applications.

In chapter 6, a study of near-wetting layer-free InAs QDs incorporated with AlAs/GaAs spacer layers grown on (001) GaAs substrates via Volmer-Weber growth mode is described. The growth of near-wetting layer-free InAs QDs was carried out using the approach of inserting of AlAs or GaAs spacer layers between InAs wetting layers and subsequent QDs. Using electron microscopy, it was revealed that conventional SK-type InAs QDs had a more well-defined triangular shape whereas the InAs QDs incorporated

using the AlAs spacer layer had a relatively less-well-defined shape. Additionally, it was found that the InAs QDs incorporated with a spacer layer had smaller dot density and more symmetrical large sizes with an apparent bimodal size distribution (two distinct families of large and small dots) compared with conventional InAs QDs without spacer layers.

In chapter 7, a summary of the important conclusions and advances achieved in this study is presented. Prospective scope and comments for future work, particular the further improvement of TEM characterization, are also provided.

REFERENCES


[1] J. R. Balfour, M. L. Shaw, and S. Jarosek, *Introduction to photovoltaics*. (Jones & Bartlett Learning, Burlington, 2013).

[2] C. S. Solanki, *Solar photovoltaics : fundamentals, technologies and applications*, Second edition ed. (PHI Learning, New Delhi, 2011).

[3] A. Luque and S. Hegedus, *Handbook of photovoltaic science and engineering*, 2nd ed. (Wiley, Chichester, West Sussex, U.K., 2011).

[4] A. G. Aberle, Thin Solid Films **517** (17), 4706 (2009).

[5] S. K. Deb, Renew Energ **8** (1-4), 375 (1996).

[6] http://www.solarlightaustralia.com.au/.

[7] U. Rau, D. Abou-Ras, T. Kirchartz, and MyiLibrary., (Wiley-VCH,, Weinheim, Germany, 2011).

[8] D. Y. Goswami, F. Kreith, J. F. Kreider, and F. Kreith, *Principles of solar engineering*, 2nd ed. (Taylor & Francis, Philadelphia, PA, 2000).

[9] G. H. Bauer, Appl Surf Sci **70-1**, 650 (1993).

[10] A. Goetzberger and C. Hebling, Sol Energ Mat Sol C **62** (1-2), 1 (2000).

[11] M. Bosi and C. Pelosi, Progress in Photovoltaics: Research and Applications **15** (1), 51 (2007).

[12] M. A. Green, K. Emery, Y. Hishikawa, W. Warta, and E. D. Dunlop, Progress in Photovoltaics: Research and Applications **21** (1), 1 (2013).

[13] A. W. Bett, F. Dimroth, G. Stollwerck, and O. V. Sulima, Appl Phys a-Mater **69** (2), 119 (1999).

[14] M. R. Brozel, G. E. Stillman, and INSPEC (Information service), *Properties of gallium arsenide*, 3rd ed. (INSPEC, London, 1996).

[15] H. M. Manasevit, Journal of Crystal Growth **55** (1), 1 (1981).

[16] D. J. Smith, Journal of Electronic Materials **42** (11), 3168 (2013).

[17] C. S. Ferekides, U. Balasubramanian, R. Mamazza, V. Viswanathan, H. Zhao, and D. L. Morel, Solar Energy **77** (6), 823 (2004).

[18] M. Afzaal and P. O'Brien, Journal of Materials Chemistry **16** (17), 1597 (2006).

[19] J. Venables, *Introduction to surface and thin film processes*. (Cambridge University Press, Cambridge, UK ; New York, 2000).

[20] http://en.wikipedia.org/wiki/Stranski-Krastanov_growth.

[21] K. Oura, V. G. Lifshits, A. A. Saranin, A. V. Zotov, and M. Katayama, *Surface science : an introduction*. (Springer, Berlin etc., 2010).

[22] A. Pimpinelli and J. Villain, *Physics of crystal growth*. (Cambridge University Press, Cambridge, 1998).

[23] K. Oura, *Surface science : an introduction*. (Springer, Berlin ; New York, 2003).

# CHAPTER 2

# EXPERIMENTAL PROCEDURES

This chapter presents a brief overview of relevant materials growth methods and the major characterization techniques, specifically transmission electron microscopy (TEM) and scanning transmission electron microscopy (STEM), that were extensively used in the experimental studies of this dissertation research.

## 2.1 Molecular beam epitaxy

Molecular beam epitaxy (MBE), which was invented in the late 1960s at Bell Telephone Laboratories,[1] is one of many methods used for depositing epitaxial thin films. MBE utilizes an advanced ultrahigh-vacuum facility (base pressure $10^{-9} \sim 10^{-10}$ Torr) to grow compound semiconductor and oxide materials with great precision (< 0.1 nm) and high purity (> 99.999%). MBE growth has produced many types of complex layered structures which are further processed to fabricate a wide range of electronic and optoelectronic devices, including high-speed transistors, light-emitting diodes, high-efficiency solar cells and solid-state lasers.

A typical MBE system is schematically illustrated in Fig. 2.1.[2] It usually consists of a growth chamber, auxiliary chambers and a load-lock. The growth chamber is shown in more detail in Fig. 2.2.[2] It includes sources of molecular beams, a manipulator for heating, a cryoshroud surrounding the growth region, shutters to occlude the molecular beams, a suitable gauge to measure chamber base pressure and molecular beam fluxes, a reflection-high-energy electron diffraction (RHEED) gun and fluorescent screen to

monitor film surface structure, and a quadruple mass analyzer to monitor specific background gas species or molecular beam flux composition.[2]

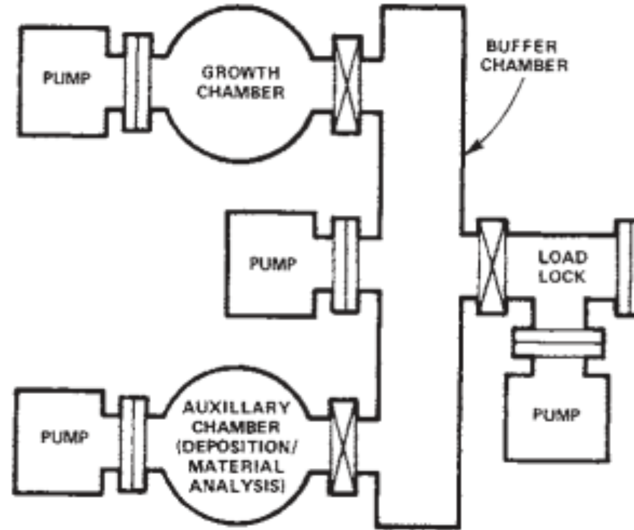


Fig. 2.1 Functional schematic of a basic MBE system.[2]

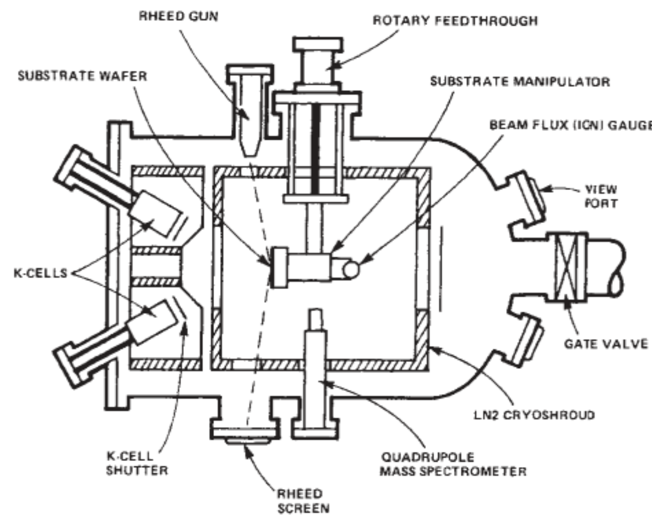


Fig. 2.2 Schematic cross-section of a typical MBE growth chamber.[2]

MBE offers several advantages over other epitaxial growth techniques, such as precise control of the growth rate, rapid change in atomic composition and atomically abrupt crystalline interfaces. The samples investigated in this dissertation were primarily

grown using MBE, and details of the specific growth conditions for each materials system are described in the following.

2.1.1 MBE growth of CeTe QDs on ZnTe/GaSb

The growth of self-assembled CdTe quantum dots (QDs) was carried out at University of Notre Dame. The CdTe QDs were formed by depositing CdTe layers on thick ZnTe buffer layers that had been deposited on GaSb (001) substrates,[3] using the method of Te overlayer desorption.[4] First, a 100-nm-thick GaSb buffer layer was deposited on a commercial GaSb (001) substrate, and then a high quality 300-nm-thick ZnTe epilayer was grown. Several monolayers of CdTe were subsequently deposited using atomic layer epitaxy (ALE), with alternating depositions of 0.5 ML of Cd and 0.5 ML of Te to form CdTe layers of the desired thickness. A series of CdTe layers were grown in this manner, with CdTe deposition thicknesses ranging from 3 to 7.5 ML.[3] The strained CdTe epilayers were cooled down to room temperature in the MBE chamber, followed by capping with an amorphous Te layer, and then annealing at 300 ˚C for several minutes. Due to surface energy variations, desorption of the Te overlayer induced the formation of CdTe QDs,[4] which is attributed to the Stranski-Krastanov growth mode.[5] To obtain capped CdTe QD samples, the growth procedure was completed by deposition of 100-nm-thick ZnTe capping layers.

2.1.2 MBE growth of dilute-nitride films on GaAs

The growth of dilute-nitride $GaAsN_x$ films was carried out at University of Houston. The dilute-nitride films were grown using a radio-frequency (RF) plasma-assisted molecular/chemical beam exitaxy system (M/CBE) in a Riber 32[TM] reactor, as described in detail elsewhere.[6] Ultrahigh-purity nitrogen gas was injected using an EPI

UNI-Bulb™ RF plasma source operating at a frequency of 13.56 MHz. All samples were fabricated on nominal (001) orientation GaAs wafers. A 0.5-μm-thick undoped GaAs buffer layer was first deposited at 520 ˚C before growth of the dilute-nitride films. The $GaAsN_x$ epilayers were grown on the buffer layer at 450 ˚C at a rate of 1 μm/h. In order to minimize unintentional N contamination, the RF plasma power was switched off during growth of the GaAs buffer layer, and the plasma was ignited immediately before commencing growth of the dilute-nitride films. [6]

2.1.3 MBE growth of self-assembled InAs QDs embedded in $GaAs_{1-x}Sb_x$ epilayers grown on GaAs (001) substrates

The growth of self-assembled InAs QDs was carried out at Arizona State University. The structures were grown on undoped (001) GaAs substrates in an Applied Epi GEN III MBE system with As and Sb valved cracker cells. The onset of deoxidation of the GaAs substrates at 580 ºC was confirmed by monitoring RHEED patterns. Throughout growth, the surfaces of the growing structures were also monitored by RHEED to ensure high-quality (2×4) GaAs reconstruction, and to observe the transition of InAs growth from layer-by-layer to QD formation. After deoxidation of the substrate for 10 min at 620 ºC, a thick GaAs buffer layer (~200 nm) was grown at 580 ºC. The substrate temperature was then ramped down to 500 ºC and a thin (~5 nm) layer of GaAs was deposited. Two MLs of InAs were then deposited at a growth rate of ~0.04 ML/s, followed by a 20-nm-thick GaAsSb capping layer (~20 nm) with the same Sb/As flux ratio used for the GaAsSb buffer layer. The structures were completed by the growth of a 50-nm-thick GaAs capping layer.

### 2.1.4 MBE growth of near-wetting layer-free InAs QDs incorporated with AlAs/GaAs spacer layers on GaAs (001) substractes

Self-assembled InAs quantum dots were grown on GaAs (001) by molecular beam epitaxy. Prior to InAs/GaAs deposition, the native oxide layer was thermally removed in $As_2$ ambient at 580 ºC. Next, a GaAs buffer layer of thickness 340 nm was grown at 560 ºC in $As_2$ overflow at a growth rate of 1 ML/s. Finally, InAs was deposited on the GaAs buffer layer at temperatures ranging from 440 ºC to 520 ºC at a growth rate of 0.1 ML/s. During the InAs deposition, *in-situ* RHEED observation was carried out along [1-10] & [1-30] crystallographic directions. Real time probing of chevron angle of the QDs was performed by acquiring multiple images using KSA 400 RHEED data acquisition software. QD average sizes and average size distribution were extracted in real time by analyzing the evolution of RHEED chevron intensity fringes, whereas the dot density was extracted through the evolution of the intensity of the 02 diffraction spot during the growth process.

## 2.2 Transmission electron microscopy

### 2.2.1 High-resolution transmission electron microscopy

Image formation in conventional TEM uses amplitude contrast with a small objective aperture, whereas HRTEM imaging uses phase contrast resulting from the interference of several diffracted beams over a wider range of scattering angles. High-resolution transmission electron microscopy (HRTEM) can nowadays provide structural information with spatial resolution better than 0.1 nm.[7-10] In most crystalline semiconductors, the projections of individual atomic columns can be resolved in low-index zones.[11] The electron microscopy observations reported in this dissertation were

mostly carried out using a JEOL JEM-4000EX high-resolution transmission electron microscope (HR-TEM), operated at 400 keV and equipped with a double-tilt, top-entry sample holder which can provide better stability against sample drift. Both phase-contrast and diffraction-contrast imaging were typically used to characterize the thin-film solar cell samples.

2.2.2 Scanning transmission electron microscopy

High-angle annular-dark-field scanning transmission electron microscopy (HAADF-STEM) is an alternative imaging technique that allows structural information to be obtained by scanning an atomic-scale focused probe across the sample.[12] STEM image formation is fundamentally different from conventional TEM image formation. One potential advantage for STEM is that defects in the imaging lenses do not affect image resolution. Hence chromatic aberrations, which can limit TEM image resolution, are considered to be less important in STEM.[13] Therefore, STEM imaging can have a slightly better spatial resolution than TEM imaging under optimum illumination conditions, and it is often preferred for characterizing relatively thicker specimens.[13] Another advantage of HAADF-STEM imaging is that it provides images free of contrast reversal over a large range of thickness and defocus, thereby overcoming some of the problems of image interpretation in HRTEM caused by dynamical diffraction. [12,13]

Different types of STEM images can be formed by using electrons with different scattering angles. In general, the typical collection semi-angle is about 0-20 mrad for bright-field (BF) imaging, 20-30 mrad for annular bright-field (ABF) imaging, and 30-200 mrad for annular-dark-field (ADF) imaging. Among all STEM imaging techniques, high-angle annular-dark-field (HAADF) imaging is a type of Z-sensitive method

involving collection of scattered electrons with an ADF detector with typical collection range of 75-200 mrad. The HAADF-STEM signal depends strongly on the average atomic weight as a function of $Z^n$, where n is about 1.5-2.[12] Most HAADF-STEM images presented in this dissertation were recorded using a JEOL-2010F field emission STEM operated at 200 keV, which provided a nominal probe diameter of ~2 Å. This microscope is equipped with a field-emission electron gum, double-tilt sample holder, charge-coupled-device (CCD) camera, annular-dark-field (ADF) detector, EDX and EELS detectors. It has a structural resolution of 2.3 Å in TEM imaging mode and an instrumental resolution of 1.4 Å in ADF-STEM imaging mode. The inner/outer detector semi-angles and electron-beam convergence semi-angles for the JEOL-2010F at ASU had been measured previously and are summarized for convenience in Tables 2.1 and 2.2.

Table 2.1 JEOL ADF detector range in JEOL-2010F with commonly used camera lengths.

| Camera length (cm) | Inner detector angle (mrad) | Outer detector angle (mrad) |
|---|---|---|
| 6 | 41.8 | 158.5 |
| 8 | 45.1 | 171.2 |
| 10 | 33.6 | 127.0 |
| New 6 | 51.8 | 196.6 |

Table 2.2 Convergence semi-angles in JEOL-2010F with different condenser lens (CL) apertures.

| CL aperture (#: µm) | Convergence semi-angle (mrad) |
|---|---|
| #2: 40 | 12.5 |
| #3: 30 | 8.3 |
| #4: 10 | 3.0 |

## 2.3 Analytical spectroscopy

### 2.3.1 Energy-dispersive X-ray spectroscopy

Energy-dispersive X-ray spectroscopy (EDXS or EDS) is an analytical technique used for chemical analysis or elemental detection of a sample, which is widely available with modern SEM, TEM and STEM. An atom contains ground state electrons in discrete energy levels. The incident electron beam may excite electrons in an inner shell, ejecting them from the shell while creating holes where the electrons were located. Electrons from higher-energy outer shells then fill the holes by releasing X-rays. The emitted X-ray carries characteristic information about the element.[13] STEM makes a great addition to EDXS microanalysis for the reason that STEM-EDXS provides composition distributions across the entire sample region of interest.[14] In this research, STEM-EDXS was performed to analyze composition distributions usually across structural interfaces.

## 2.4 TEM sample preparation

The goal of TEM sample preparation is to obtain specimens that are electron-transparent, with thicknesses ranging from a few to several hundreds of nanometers.[13]

Most specimens intended for cross-sectional and plan-view electron microscopy observations in this research were prepared using a combination of mechanical polishing, dimpling and argon-ion-milling, and a few samples were sectioned using a dual-beam focused ion beam (FIB) also equipped with a scanning electron microscope.

### 2.4.1 Combined mechanical polishing and dimpling

A piece of solar cell wafer was placed on a glass slide and mounted by wax on a hot plate set to 160 °C. It was then cleaved into small pieces about 3 mm in width using a diamond blade cutter. Two small pieces were then glued with film layers face-to-face using epoxy glue (M-bond adhesive) in the case of cross-sectional samples. The samples had to be gently pressed with a specimen clamp to remove excess glue from between the two pieces. The specimens were then placed in an oven for curing for a period of 30 minutes or longer with a temperature of about 90 °C.

After curing, standard mechanical polishing and dimpling were applied for further thinning. The first side of the cross-section specimen was gently polished down by a few millimeters using the Allied MultiPrep polishing system. Most visible scratches around the target area of interest should be removed with diamond lapping films. The specimen was then flipped over and the second side was polished down to a total thickness of ~80-120 μm. This treatment was followed by dimpling with a Cu-wheel and/or a cloth-wheel until the thickness of the specimen was less than ~ 10 μm. The specimen was then glued onto a copper/molybdenum grid with M-bond since the specimen was still on a glass stub. After curing in a low temperature oven (90°C), the specimen would be placed in fresh acetone for several hours to remove the specimen from the glass stub. The specimen was finally argon-ion-milled at 2.5-3.5 keV and in the range of 6 to 8 degrees, while held

at liquid nitrogen temperature using Gatan Model 691 PIPS system until hole perforation was achieved. Low-angle (6 degree), low-energy (approximately 1.8 keV) milling was often used for final thinning to minimize the formation of any amorphous surface or interfacial layers. Using this approach, the result is a specimen with a hole at the interface between the solar-cell stripes. i.e., in side view, the specimen has the shape of a wedge, with decreasing thickness toward the hole.

### 2.4.2 Focused ion beam

The focused ion beam (FIB) is well known for its versatility in semiconductor research and industry. It is used, for example, in imaging, ion-induced deposition, gas-assisted etching, implantation, and milling.[15] An important application of FIB is that the technique can prepare samples with excellent positional accuracy and site specificity for TEM characterization. The most useful sample preparation approach is called FIB lift-out.

The FIB equipment used in this dissertation was a FEI Nova 200 NanoLab equipped with an ultrahigh-resolution field emission scanning electron microscope (SEM) and a precise focused ion beam generator. This combination enabled the operator to view the milling process in real-time and make adjustments with immediate effect if necessary. The procedure for FIB lift-out process is described in the following paragraph.

Locate the sample and choose the area to investigate (ROI). After selecting the ROI, a micron thick strip of platinum is electro-deposited to protect the target area beneath from being damaged by the Ga ions used for milling. The selection is made by milling away the specimen on both sides of the Pt strip using the Gallium ion beam

maintained at 30 kV with a typical current of 7 nA. Further specimen thinning on either side of the Pt strip is then carried out at a reduced ion current of 3 nA. The sample is then tilted to 7º (from horizontal) and areas for the release cuts are marked, and the approximate Z-depth (on the order of the thickness of the thinned slab) is entered and the selected areas are cut. Next, a probe is affixed to the side of the specimen, and then Pt deposition at the probe tip binds it tightly to the strip. Final release cuts are then made to free the specimen from the underlying bulk. These cuts are made at very low current of 10 pA. The final polishing of TEM specimen is made to thin the specimen even further with an ion beam current of 100 pA.

REFERENCES


[1] J. R. Arthur, Surf Sci **500** (1-3), 189 (2002).

[2] K. Seshan, *Handbook of thin-film deposition processes and techniques : principles, methods, equipment and applications*, 2nd ed. (Noyes Publications / William Andrew Pub., Norwich, N.Y., 2002).

[3] R. E. Pimpinella, A. M. Mintairov, X. Liu, T. H. Kosel, J. L. Merz, J. K. Furdyna, and M. Dobrowolska, J Vac Sci Technol B **29** (3) (2011).

[4] F. Tinjod, B. Gilles, S. Moehl, K. Kheng, and H. Mariette, Applied Physics Letters **82** (24), 4340 (2003).

[5] L. Krastanow and I. N. Stranski, Z Kristallogr **99** (5), 444 (1938).

[6] M. A. Pinault, A. Freundlich, J. A. H. Coaquira, and A. Fotkatzikis, Journal of Applied Physics **98** (2), 023522 (2005).

[7] D. J. Smith, Ultramicroscopy **108** (3), 159 (2008).

[8] D. J. Smith, Microscopy and Microanalysis **14** (1), 2 (2008).

[9] D. J. Smith, Micron **43** (4), 504 (2012).

[10] D. J. Smith, T. Aoki, J. Mardinly, L. Zhou, and M. R. McCartney, Microscopy **62**, S65 (2013).

[11] P. R. Buseck, J. M. Cowley, and L. Eyring, *High-resolution transmission electron microscopy and associated techniques*. (Oxford University Press, New York ; Toronto, 1992).

[12] S.J. Pennycook, P.D. Nellist, Microscopy and Microanalysis **6** (04), 343 (2000).

[13] D. B. Williams and C. B. Carter, *Transmission electron microscopy : a textbook for materials science*, 2nd ed. (Springer, New York, 2008).

[14] S. J. Pennycook and P. D. Nellist, *Scanning transmission electron microscopy : imaging and analysis*. (Springer, New York, 2011).

[15] L. A. Giannuzzi, *Introduction to focused ion beams : instrumentation, theory, techniques, and practice*. (Springer, New York, 2005), p.357 S.

# CHAPTER 3

# STRUCTURAL CHARACTERIZATION OF CdTe QUANTUM DOTS GROWN ON ZnTe/GaSb (001) COMPOSITE SUBSTRATES BY MOLECULAR BEAM EPITAXY

This chapter describes a systematic structural characterization of CdTe quantum dots grown by molecular beam epitaxy (MBE) on ZnTe/GaSb composite substrates. The work was carried out in collaboration with the group of Professor Jacek Furdyna at University of Notre Dame. Robert E. Pimpinella and Dr. Xinyu Liu at University of Notre Dame performed the sample growth. My role has been the microstructural characterization using electron microscopy. The major results of this collaborative research have been submitted for publication.

## 3.1. Introduction

Tuning the band gaps of semiconductor alloys by adjusting composition or by depositing multilayered structures is a routine approach for modifying transport and optoelectronic properties. In this respect, however, integrating different II-VI and III-V materials, such as CdSe/ZnSe and InAs/GaAs, by growing layered structures is often difficult to achieve due to their large lattice mismatch. Thus, in order to relax lattice strain and reduce the density of defects formed in highly-strained systems, self-assembled quantum dots (QDs) are considered as an attractive alternative approach for integrating materials with highly mismatched lattice parameters.[1] Self-assembled quantum dots have recently attracted much interest for the development of novel II-VI devices, especially because of their promising optoelectronic properties.[2] Many studies relating to self-

assembled quantum dots have been carried out on III-V (e.g. GaN/AlN, InAs/GaAs), and IV-IV (e.g. Si/Ge) materials, but the II-VI materials combinations remain much less explored.

As an important member of the II-VI semiconductor family, cadmium telluride (CdTe) is an attractive material for near-infrared applications due to its relatively low band gap of 1.44 eV at room temperature,[3] which is nearly the same as that of CdSe and InAs. CdTe can be grown epitaxially on other II-VI materials, such as zinc telluride (ZnTe),[4] but it can be difficult to grow high-quality CdTe layers on ZnTe because of the interfacial strain resulting from the large lattice mismatch (6.4%). In order to relax the strain and reduce the density of defects in the highly-strained CdTe/ZnTe system, the growth of CdTe QDs has been pursued as an alternative approach for integrating CdTe with ZnTe.[1] Thus, a study of the structure and morphology of CdTe QDs grown on ZnTe is important for understanding the structure-growth relationship of the two materials, which is an essential pre-requisite before these QD structures can be utilized in actual device applications.[5] This objective is the primary motivation of the present study.

The growth and characterization of self-assembled CdTe QDs on ZnTe epilayers by different techniques has been previously reported by several groups.[1,2,5-16] For example, Jang *et al.* described MBE growth of CdTe QDs at 315°C, and reported a 2D-3D shape transition occurring at a CdTe layer thickness of ~1.5-2.0 ML,[10] while Lee *et al.* later showed AFM images of larger CdTe pyramids (~56nm wide × ~33nm high) grown by atomic layer epitaxy (ALE) with a substrate temperature of 310°C,[11] and No *et al.* showed an atomic-force microscopy (AFM) image of CdTe 'dots' grown at 320°C by ALE.[12] Lee *et al.* have since reported MBE growth at substrate temperatures in the range

from 310 to 350°C.[13] These later results were explained in terms of a Volmer-Weber (VW) growth mode, meaning that the 3D QD growth occurred spontaneously without requiring any prior 2D growth, while the QD size/density were reported to be controlled by both deposition thickness and substrate temperature.[13] Terai *et al.* have also reported ALE growth of CdTe QDs (~20nm wide, ~2.7nm high, with a QD density of ~ $8x10^{12}$ / $cm^2$) at a substrate temperature of 300°C, using a ZnTe/GaAs(001) composite substrate.[7] The approach adopted in the present study follows instead from the work of Marsal et al,[14] and Tinjod et al,[1] who used ALE deposition at lower temperatures (270-290°C) where the 2D growth mode was found to persist to well beyond the normal 2D-3D growth transition that occurs at ~3ML for standard MBE growth at the same temperature. This chapter reports transmission electron microscope (TEM) studies of self-assembled CdTe QDs deposited by the ALE technique on ZnTe/GaSb (001) composite substrates.[5]

## 3.2. Experimental Details

The self-assembled CdTe QDs were formed by depositing CdTe layers using ALE on thick ZnTe epilayers that had been deposited on GaSb (001) substrates,[16] using the method of Te overlayer desorption.[15] Two types of CdTe QDs samples (capped and non-capped) were prepared in this study, as illustrated in Fig. 3.1. Details of the sample structures and growth conditions were given in section 2.1.1 of Chapter 2.

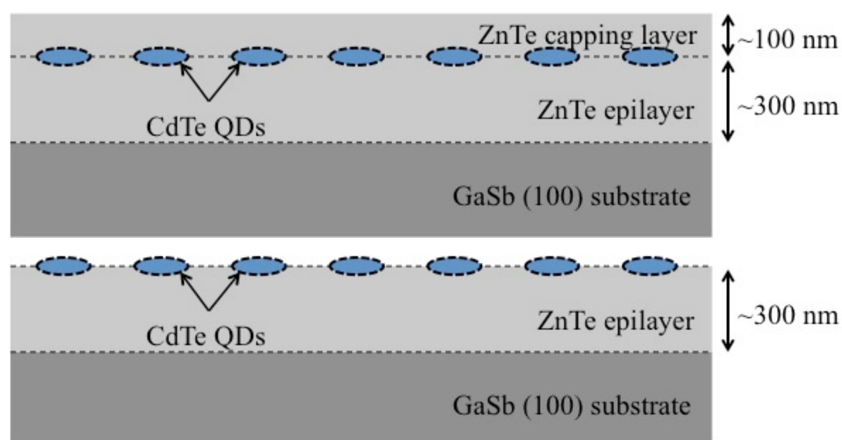


Figure 3.1 Schematic of sample structure for CdTe QDs on ZnTe/GaSb composite substrates. Upper: capped CdTe QDs. Lower: non-capped CdTe QDs.

For TEM studies, the samples were prepared for both cross-sectional and plan-view observation using mechanical polishing and dimpling followed by argon ion-milling, as described in section 2.4 of Chapter 2. Diffraction-contrast and high-resolution phase-contrast TEM images were taken using a JEM-4000EX high-resolution transmission electron microscope (TEM) operated at 400 keV, with a structural resolution of 1.7 Å. The samples were also examined using high-angle annular-dark-field (HAADF) imaging with a JEOL-2010F field-emission scanning transmission electron microscope (STEM) operated at 200 keV and having a nominal probe diameter of ~2Å.

## 3.3. Results & Discussion

The self-assembled CdTe QDs examined here were previously investigated using AFM and photoluminescence.[16] The sizes of uncapped CdTe QDs were reported to range from ~10 to ~30nm in diameter, with the larger QDs corresponding to greater CdTe deposition thicknesses. The QD surface densities were estimated to be ~ $1.5 \times 10^{10}$ / $cm^2$.

Figure 3.2(a) is a low-magnification diffraction-contrast TEM image showing a cross-sectional specimen of the capped 4.5 ML QD sample, which reveals a very high quality ZnTe epilayer on top of the GaSb buffer. The interface between the GaSb substrate and the ZnTe layer is observed to be coherent and virtually defect-free, as would be anticipated from the small (~0.13%) lattice mismatch between the two materials. The CdTe wetting layer (marked by arrow) and the capped CdTe QDs deposited on the ZnTe epilayer are also visible. After examining images of many individual CdTe QDs, it became apparent that the shapes of the CdTe QDs were generally not well-defined.

The morphology of the capped 4.5 ML CdTe QD sample was also characterized in plan-view, as illustrated by the representative image shown in Fig. 3.2(b). This diffraction-contrast image reveals the very high density and the not-well-defined shapes of these capped CdTe QDs, which is consistent with the cross-sectional observations and the earlier AFM study.[16] The enlargement in Fig. 3.2(c) shows several of the CdTe QDs with greater clarity. The distinctive light/dark contrast visible as a line through some of these QDs is reminiscent of the contrast observed in plan-view images of Ge/Si QDs caused by interfacial dislocations lying along [110]-type directions.[19] Overall, the observed morphology of the CdTe/ZnTe QD system (not-well-defined shapes, and the absence of well-defined facets) is quite similar to that reported earlier for the CdSe/ZnSe system,[20] suggesting that this general structural appearance could be a characteristic that distinguishes II-VI nanostructures from analogous III-V or IV-IV nanostructures.

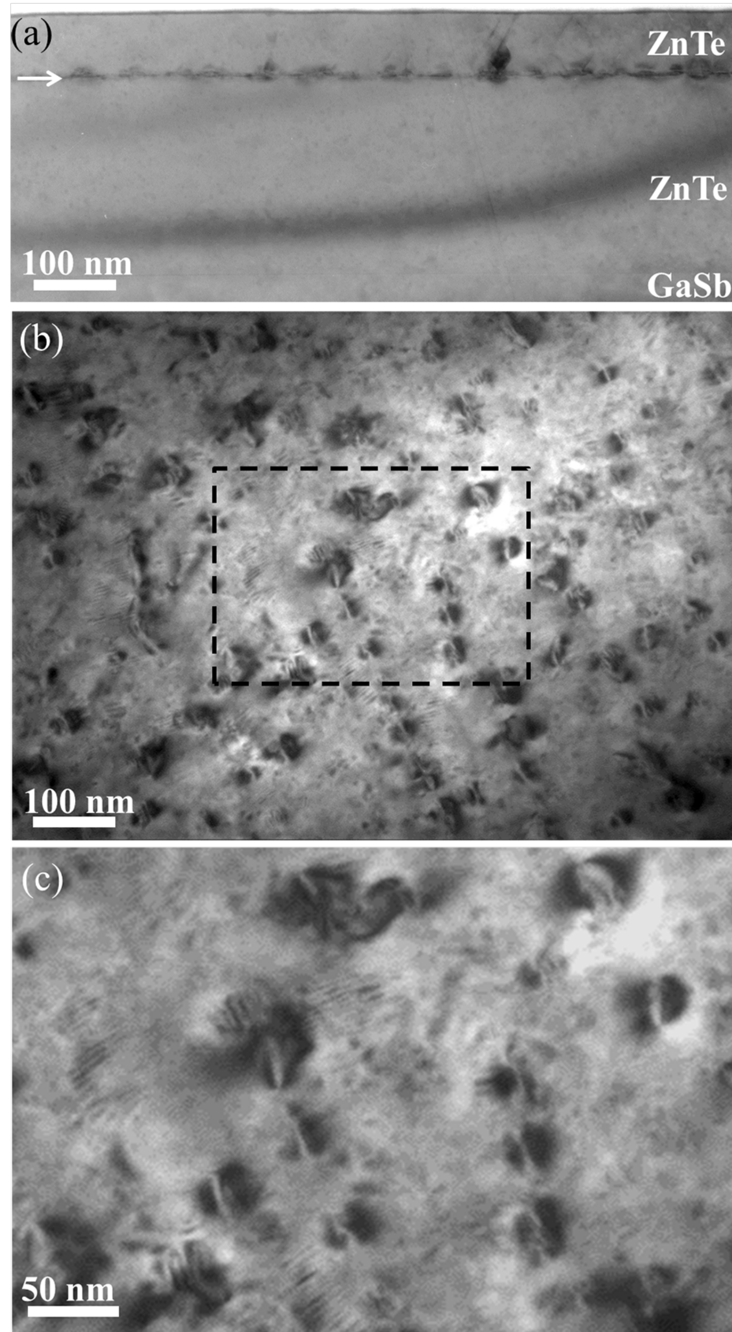


Fig. 3.2. Electron micrographs of specimen with capped 4.5 ML CdTe QDs. (a) cross-sectional diffraction-contrast TEM image showing CdTe layer (arrowed) grown on ZnTe/GaSb composite substrate and capped by ZnTe layer; (b) plan-view diffraction-contrast TEM image showing broad distribution of shapes and sizes of CdTe QDs; (c) Enlargement from (b) showing several CdTe QDs with light/dark contrast indicative of interfacial misfit dislocations.

An uncapped 4.5 ML CdTe QD sample was also prepared for cross-sectional observation. Figure 3.3(a) shows a low-magnification image of several closely-spaced CdTe QDs, and Fig. 3.3(b) shows a higher magnification lattice image of a typical uncapped CdTe QD. These images confirm that the sample grown with 4.5 ML CdTe but without ZnTe capping also has poorly defined QD shapes, similar to the capped QDs. The results suggest that these self-assembled CdTe QDs do not have any preferred surface facets, which is in contrast with QDs of other epitaxial systems, such as InAs/GaAs or Ge/Si. In addition, it appears that deposition of the ZnTe capping layer does not significantly affect the morphology of the CdTe QDs.

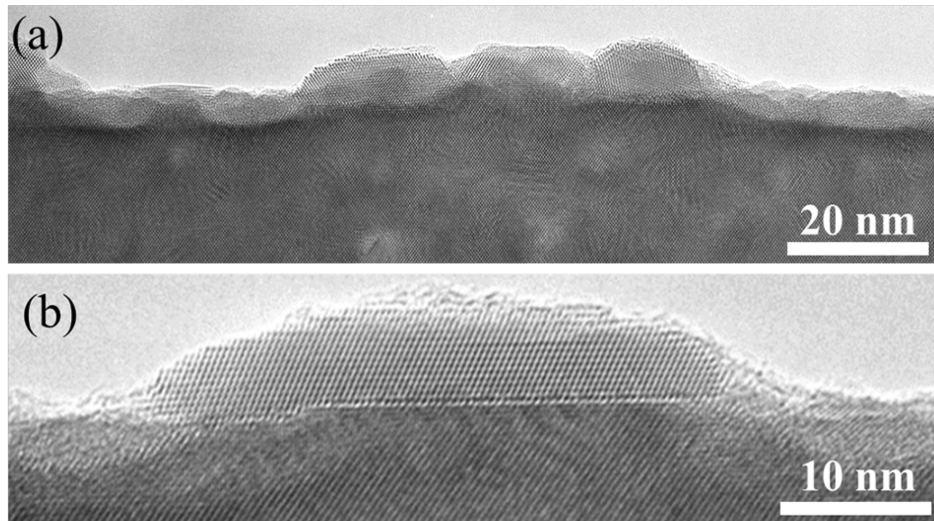


Fig. 3.3. Cross-sectional electron micrographs of uncapped 4.5 ML CdTe QDs. (a) phase-contrast XTEM image showing the general QD morphology; (b) XTEM lattice image showing a typical uncapped 4.5 ML CdTe QD with non-facetted shape.

Figure 3.4 shows low-magnification, cross-sectional images of the sample with capped 6.5 ML CdTe QDs. Similar to the previous case for 4.5 ML CdTe QDs that are not well-defined, these 6.5 ML CdTe QDs also have very high density, which indicates that the increased thickness of CdTe deposition does not have any substantial impact on

the QD morphology and density. However, more <110> stacking faults are observed in this case to be present in the ZnTe capping layer compared with the capped 4.5 ML CdTe QD sample. Plan-view TEM images of the 6.5 ML CdTe QD sample were also obtained with the [100] zone axis of the substrate aligned closely parallel to the incident electron beam direction. Figures 3.5(a) and 3.5(b), respectively, show plan-view ADF STEM and bright-field TEM images of the capped 6.5 ML CdTe QDs, again revealing the non-well-defined shape and high density of the CdTe QDs. Figure 3.5(c) is an enlargement from fig. 3.4(b), which shows the distinctive light/dark contrast of several of these QDs, similar to those visible in Fig. 3.2(c) showing the 4.5ML QD sample.

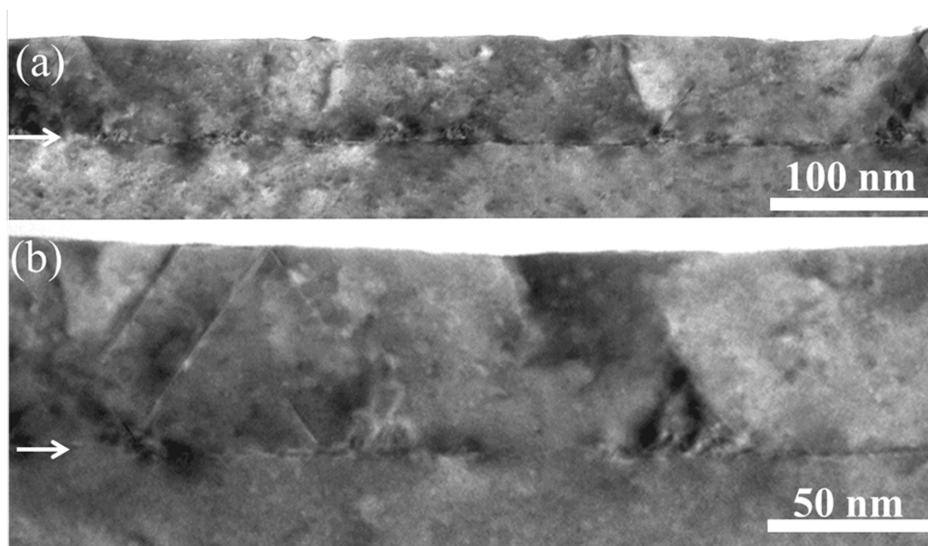


Fig. 3.4. (a) Cross-sectional phase-contrast TEM image of sample with capped 6.5 ML CdTe QD layer. Arrow indicates position of CdTe layer. (b) Enlargement showing several {111}-type stacking faults originating at the CdTe layer (see arrow).

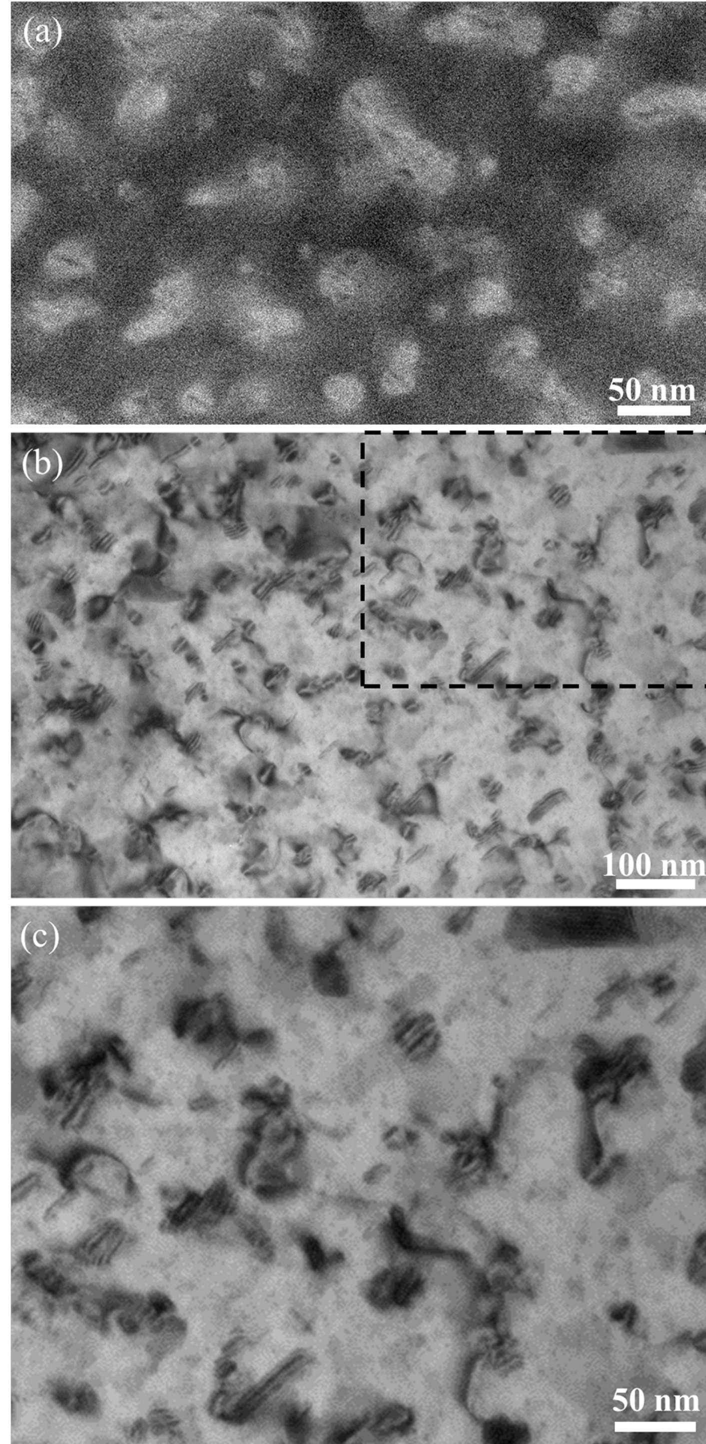


Fig. 3.5. (a) Plan-view ADF STEM image of capped 6.5 ML CdTe QDs. Regions of brighter contrast correspond to CdTe QDs with non-well-defined shapes. (b) Plan-view diffraction-contrast TEM image: (c) Enlargement from (b). Several QDs show distinctive contrast due to the presence of interfacial misfit dislocations, similar to that seen in Fig. 1(c).

Figure 3.6(a) is a TEM image that shows a typical cross-section of the uncapped 6.5 ML CdTe QD sample, again demonstrating the non-well-defined QD shape and high density. The plan-view morphology of this sample was further examined using both secondary electron imaging and atomic force microscopy. Figure 3.6(b) is a plan-view SEM image of the 6.5 ML uncapped CdTe QD sample, and 6(c) is an AFM image. Both images confirm the non-well-defined QD shapes and high surface density.

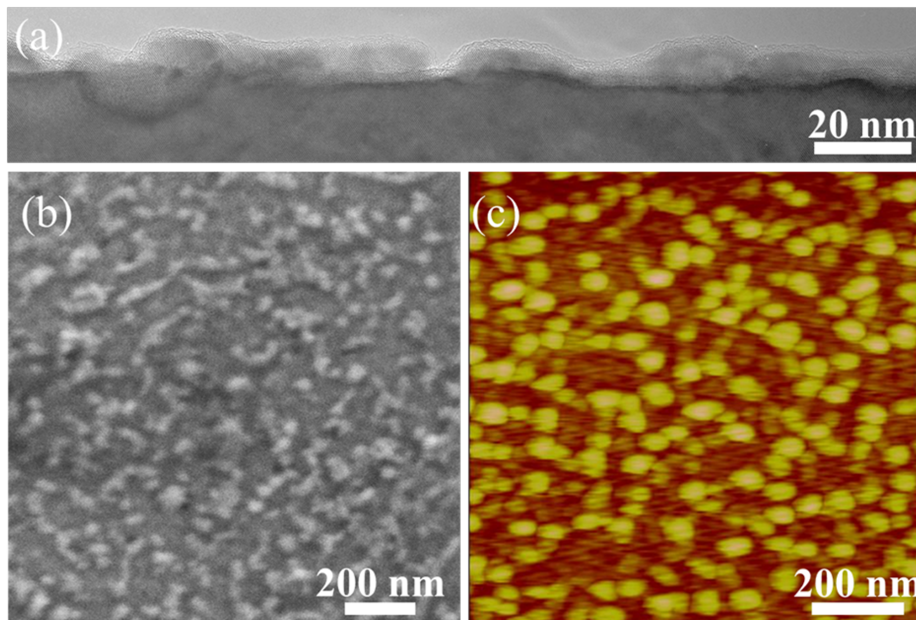


Fig. 3.6. (a) Diffraction-contrast TEM image of uncapped 6.5 ML CdTe QDs; (b) Secondary electron image of uncapped 6.5 ML CdTe quantum dots; and (c) AFM image of uncapped 6.5 ML CdTe quantum dots.

In addition to the 4.5 ML and 6.5 ML CdTe QD samples, several other samples of capped QDs, with deposition thickness ranging from 3 ML to 7.5 ML, were prepared for TEM investigation. Figure 3.7(a) shows a cross-sectional HAADF STEM (Z-contrast) image of a capped 4 ML CdTe QD sample, where the CdTe wetting layer is visible with brighter contrast. Figure 3.7(b) is a higher magnification HAADF STEM image of the

same sample showing two typical capped 4 ML CdTe QDs. Figure 3.7(c) is a HAADF-STEM lattice image of the left-hand QD from Fig. 3.7 (b), which again reveals that the CdTe QD shape is not regular. Additionally, it is apparent that the interfaces between the CdTe QD and the ZnTe layers are barely visible in Z-contrast images, suggesting the occurrence of Cd interdiffusion between CdTe and ZnTe, similar to that reported previously for the CdSe/ZnSe system.[20] This interdiffusion may be a key factor in causing the ill-defined shapes of the CdTe QDs as well as other II-VI materials.

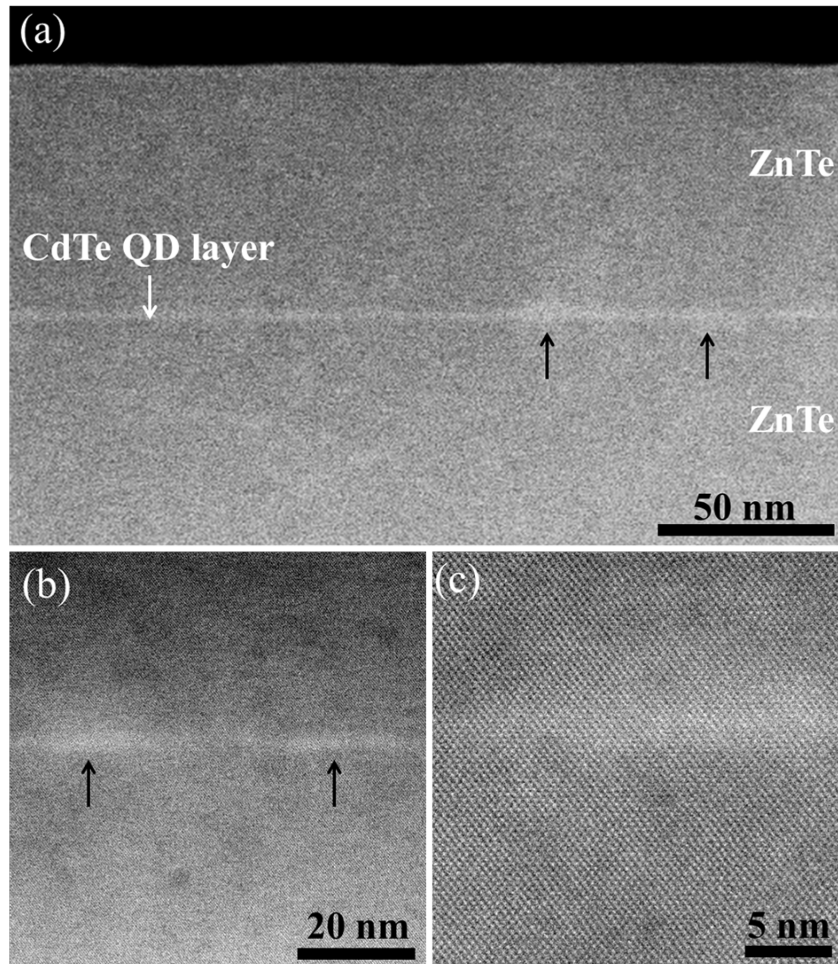


Fig. 3.7. (a) Low-magnification HAADF STEM image of capped 4 ML CdTe QDs; (b) higher magnification HAADF STEM image of the left-hand QD in (a); (c) HAADF STEM lattice image of the same QD.

These TEM observations indicate that CdTe QDs grown on ZnTe from CdTe layers via Te desorption do not have well-defined facets or shapes, in contrast to QDs formed from IV-IV or III-V materials, such as Si/Ge [19, 21] and GaN/AlN.[22] Our results also suggest that the CdTe deposition thickness is not an important factor in determining the shapes and densities of the CdTe QDs. This observation seems in direct contrast to the earlier study of CdTe QDs formed by the Volmer-Weber (VW) growth mode, in which the CdTe deposition thickness appeared to play an important role in controlling the sizes/densities of QDs.[13] This discrepancy is possibly due to a competing 2D growth mechanism via the Stranski-Krastanov (SK) growth mode.

### 3.4. Conclusions

CdTe quantum dots (QDs), with or without ZnTe capping layers, have been grown by molecular beam epitaxy using composite substrates consisting of thick ZnTe (~300 nm) epilayers deposited on GaSb(001) substrates. A series of self-assembled CdTe QDs was formed on ZnTe epilayers by depositing CdTe layers of various thicknesses in the range from 3 to 7.5 monolayers, capping with a layer of amorphous Te, and then annealing at 300°C. Analysis of cross-sectional and plan-view transmission electron micrographs revealed that CdTe QDs formed by this process had shapes that were not well-defined and similar high densities regardless of the amount of CdTe deposition. Thus, the CdTe/ZnTe QD system resembles the CdSe/ZnSe QDs studied earlier.[3] The sizes of the CdTe QDs were found to increase with increasing CdTe deposition, and in the case of capped QDs, the density of <110> stacking faults in the ZnTe capping layer also increased with increasing thickness of the CdTe layer. Overall, the irregular shapes

and the absence of crystalline facets in the CdTe QDs observed in this study strongly suggest that the process of self-assembly of II-VI semiconductor materials is quite different from the prevailing mechanism for III-V and IV-IV materials. It is clear that further extensive studies are required before optoelectronic devices based on this QD system can be realized.

REFENCES

[1] F. Tinjod, B. Gilles, S. Moehl, K. Kheng, and H. Mariette, Appl. Phys. Lett. 82 (2004) 4340.

[2] G. Karczewski, S. Mackowski, M. Kutrowski, T. Wojtowicz, and J. Kossut, Appl. Phys. Lett. 74 (1999) 3011.

[3] Collaboration: Authors and editors of the volumes III/17B-22A-41B: *Cadmium telluride (CdTe) band structure*. Madelung, O., Rössler, U., Schulz, M. (ed.). SpringerMaterials - The Landolt-Börnstein Database (http://www.springermaterials.com). DOI: 10.1007/10681719_621.

[4] S. Wang, D. Ding, X. Liu, X.-B. Zhang, D.J. Smith, J.K. Furdyna, and Y.-H. Zhang, J. Cryst. Growth 311 (2009) 2116.

[5] R. E. Pimpinella, A. M. Mintairov, X. Liu, T. H. Kosel, J. L. Merz, J. K. Furdyna, and M. Dobrowolska, J. Vac. Sci. Technol. B 29 (2011) 03C119.

[6] G. Karczewski, S. Mackowski, M. Kutrowski, T. Wojtowicz and J. Kossut, Appl. Phys. Lett. 74 (1999) 3011.

[7] Y. Terai, S. Kuroda, K. Takita, T. Okuno, and Y. Masomoto, Appl. Phys. Lett. 73 (1998) 3757.

[8] S. Mackowski, G. Karczewski, T. Wojtowicz, J. Kossut, S. Kret, A. Szczepanska and P. Dluzewski, Appl. Phys. Lett. 78 (2001) 3884.

[9] H. Kuwabara, A. Unno, K. Kouga, T. Watanabe, W. Tomoda, Y. Nakanishi, and H. Tatsuoka, Appl. Surf. Sci. 175-176 (2001) 643.

[10] M.S. Jang, S.H. Oh, H.S. Lee, J.C. Choi, H.L. Park, T.W. Kim, D.C. Choo, and D.U. Lee, Appl. Phys. Lett. 81 (2002) 993.

[11] E.H. Lee, K.H. Lee, J.S. Kim, H.L. Park, and T.W. Kim, Appl. Phys. Lett. 83 (2003) 5536.

[12] Y.S. No, T.W. Kim, H.S. Lee, and H.L. Park, Appl. Surf. Sci. 243 (2005) 143.

[13] H.S. Lee, H.L. Park, and T.W. Kim, J. Cryst. Growth 291 (2006) 442.

[14] L. Marsal, L. Besombes, F. Tinjod, K. Kheng, A. Wasiela, B. Gilles, J.-L. Rouviere and H. Mariette, J. Appl. Phys. 91 (2002) 4936.

[15] F. Tinjod, B. Gilles, S. Moehl, K. Kheng, and H. Mariette, Appl. Phys. Lett. 82 (2003) 4340.

[16] R.E. Pimpinella, X. Liu, J. K. Furdyna, M. Dobrowolska, A. M. Mintairov, and J. L. Merz, J. Electron. Mater. 39 (2010) 992.

[17] I.N. Stranski and L. Krastanow, Sitzungsber. Akad. Wiss. Wien, Math.-Naturwiss. Kl., Abt. IIb 146 (1938) 797.

[18] C. Wang, D. J. Smith, S. Tobin, T. Parodos, J. Zhao, Y. Chang, and S. Sivananthan, J. Vac. Sci. Technol. A 24 (2006) 995.

[19] D. J. Smith, D. Chandrasekhar, S. A. Chaparro, P. A. Crozier, J. Drucker, M. Floyd, M.R. McCartney, and Y. Zhang, J. Cryst. Growth 259 (2003) 232.

[20] C.S. Kim, M. Kim, J.K. Furdyna, M. Dobrowolska, S. Lee, H. Rho, L.M. Smith, H. E. Jackson, E.M. James, Y. Xin and N.D. Browning, Phys. Rev. Lett. 85 (2000). 1124.

[21] S.A. Chaparro, Y. Zhang, J. Drucker, D. Chandrasekhar, and D. J. Smith, J. Appl. Phys. 87 (2000) 2245.

[22] T. Xu, L. Zhou, Y. Wang, A. S. Ozcan. K.F. Ludwig, D. J. Smith, and T. D. Moustakas, J. Appl. Phys. 102 (2007) 073517.

CHAPTER 4

# MICROSCOPIC INVESTIGATION OF MBE-GROWN DILUTE-NITRIDE ALLOYS OF $GaAsN_X$ (0.01<X<0.04) ON GaAs FOR PHOTOVOLTAIC SOLAR CELLS

This chapter presents a detailed investigation of dilute-nitride alloys of $GaAsN_x$ grown by molecular beam epitaxy (MBE) on GaAs substrates. This work was carried out in collaboration with the group of Professor Freundlich at University of Houston. Gopi Krishna at University of Houston performed the sample growth and PL measurements. My role has been the microstructural characterization using electron microscopy. The major results of this collaborative research will soon be submitted for publication.

## 4.1. Introduction

Dilute-nitride $GaAsN_x$ alloys have attracted much interest due to their attractive optoelectronic properties such as possible tuning of the band gap of alloy-based multi-junctions.[1] Nitrogen is insoluble in many III-V semiconductors such as GaAs,[2] but metastable N concentrations can be achieved using epitaxial growth at low temperature.[3] It appears that incorporating small amounts of nitrogen can significantly decrease the band gap of dilute $GaAs_{1-x}N_x$ alloys from ~1.3 eV to 0.9 eV.[1,4-8] This energy shift extends the range of applications of dilute-nitride alloys into longer wavelengths of the solar spectrum, making these materials attractive for a wider range of optoelectronic applications, such as absorbers for high-efficiency tandem solar cells in excess of 50% (under concentrated sunlight).[9] By incorporating these alloys into multi-junction photovoltaic solar cells, high photo-conversion efficiencies have been demonstrated.[10] A

previous study showed that the introduction of a sub-cell of lattice-matched material with a band gap in the range of 1 eV - 1.25 eV enhanced the performance of conventional three-junction devices.[3] In this present study, the growth of GaAs epilayers with nitrogen incorporated using plasma-assisted molecular/chemical beam epitaxy has been investigated.

Extensive studies of the epitaxial growth of dilute nitrides and their incorporation into optoelectronic devices have been reported during the past two decades, in particular to address doping issues[11] and to enhance minority carrier diffusion length.[12,13] A better understanding of how nitrogen is incorporated into dilute-nitride alloys is critical for better utilizing these materials in the fabrication of photovoltaic solar cells. High-angle annular-dark-field scanning transmission electron microscopy (HAADF-STEM) is a powerful characterization technique that allows compositional information to be obtained by scanning an atomic-scale focused probe across the sample.[14] Here, we report a systematic investigation of dilute-nitride GaAs thin films with increasing nitrogen content using HAADF-STEM and other transmission electron microscope (TEM) techniques.

## 4.2. Experimental details

Experimental details of sample growth were described in section 2.1.2 of Chapter 2. Most images shown here were recorded using high-angle annular-dark-field (HAADF) imaging in a JEOL-2010F field-emission STEM operated at 200 keV, which provided a nominal probe size of ~2 Å. High-resolution phase-contrast TEM images were also taken using a JEM-4000EX high-resolution transmission electron microscope operated at 400 keV, with a structural resolution of 1.7 Å.

4.3. Results & Discussion

Four dilute-nitride single-layer samples were investigated in this work, with increasing N concentrations of 1.44%, 1.82%, 3.05% and 3.67%, respectively, as determined using Vegard's Law and X-ray diffraction (XRD). However, according to a previous report, the measurement of dilute-nitride $GaAs_{1-x}N_x$ alloys by this method underestimates N concentrations at larger N composition (x>0.03).[17] This measurement discrepancy is attributed to the presence of interstitial N incorporated into the dilute-nitride films. The occurrence of significant amounts of interstitial N was also found by other techniques, such as Rutherford backscattering (RBS).[18] The corresponding band gaps of these four samples were measured to be 1.21 eV, 1.15eV, 1.02 eV and 0.92 eV, respectively, as determined by photoluminescence (PL) analysis described elsewhere.[19] These numerical findings are summarized for reference in the Table 4.1.

Table 4.1 Growth conditions, nitrogen concentrations measured using XRD, and band gap measured using PL.

| Sample | $H_2$ | Plasma Power (W) | $N_2$ Flow (sccm) | $[N_{As}]$ % | Eg-300K(eV) |
|---|---|---|---|---|---|
| C 1053 | Yes | 600 | 1 | 1.44 | 1.21 |
| C 1052 | No | 600 | 1 | 1.82 | 1.15 |
| C 1046 | No | 400 | 1 | 3.05 | 1.02 |
| C 1038 | No | 500 | 1 | 3.67 | 0.92 |

Figure 4.1(a) is a low-magnification HAADF-STEM image of the $GaAsN_{0.0144}$ film grown on GaAs (001), showing the typical cross-sectional morphology. The $GaAsN_{0.0144}$ epilayer clearly has brighter contrast than the GaAs buffer layer. Because of the Z-sensitivity of HAADF-STEM imaging, it thus seems that the epilayer must contain material of overall higher atomic weight. Thus, some nitrogen must have been incorporated into the $GaAsN_{0.0144}$ film, presumably by occupying interstitial positions within the GaAs crystal. Figure 4.1(b) is another HAADF-STEM image showing the interface region between the $GaAsN_{0.0144}$ film and the GaAs buffer layer at higher magnification. The formation of a thin, high-N-composition, quantum-well-like layer, is marked by the arrow. This layer was later found to be associated with ignition of the N plasma using the conventional shutter-controlled deposition system during growth. Figure 4.1(c) is a high-resolution HAADF-STEM lattice image showing perfect lattice-matching between the GaAs buffer layer and the $GaAsN_{0.0144}$ epilayer.

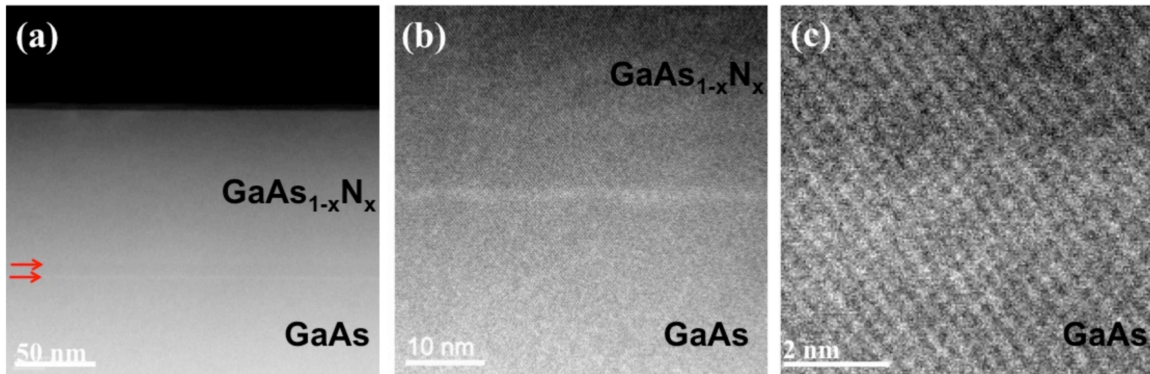


Fig.4.1: (a) Low-magnification HAADF-STEM image of $GaAsN_{0.0144}$ film grown on GaAs. Two interfaces are observed (as labeled by arrows). (b) HAADF image shows buffer-epi interface area. Two interfaces are visible, although the contrast of the upper one is extremely weak. Contrast of epilayer is slightly higher than that buffer layer. (c) HAADF-STEM lattice image from lower interface region. Brighter contrast but no lattice fringe disruptions.

Figure 4.2(a) is a typical low-magnification HAADF-STEM image of the $GaAsN_{0.0182}$ film. Careful examination revealed that the contrast of the epilayer was slightly higher than the GaAs buffer layer, again implying that a significant amount of interstitial nitrogen had been incorporated into the alloy film. Moreover, an N-rich parasitic layer is observed at the top of the GaAs buffer layer, before growth of the dilute nitride layer, as shown arrowed in Fig. 4.2(b). Figure 4.2(c) is a HAADF-STEM lattice image showing the interface region of the $GaAsN_{0.0182}$ film. The interface is not completely flat but appears to be free of interruptions.

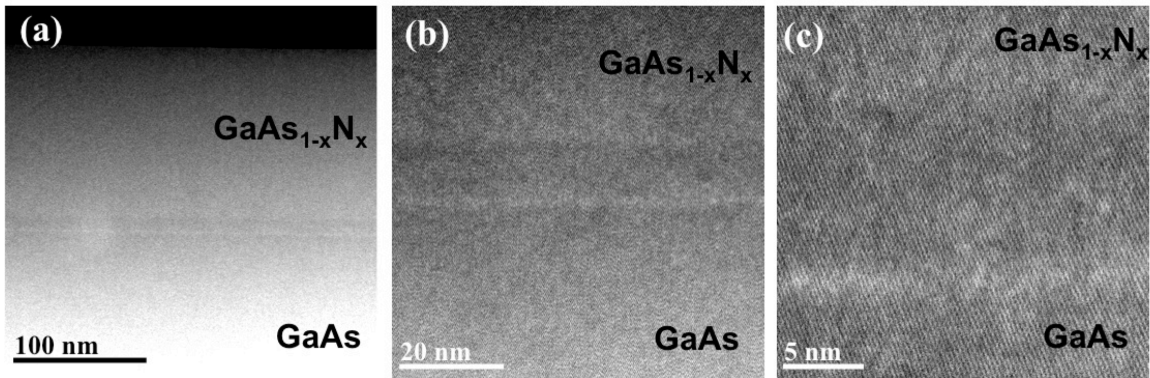


Fig. 4.2: (a) HAADF-STEM image shows two apparent interfaces between the GaAs buffer layer and the GaAsN epilayer. (b) HAADF-STEM image shows that epilayer contrast is slightly brighter than the buffer layer, which would imply that the nitrogen is interstitial. (c) HAADF-STEM image showing interface region. Brighter lower interface indicates overall higher atomic number material.

The $GaAsN_{0.0305}$ sample was characterized using TEM imaging and HAADF-STEM imaging. Figure 4.3(a) is a conventional phase-contrast TEM image showing the entire $GaAsN_{0.0305}$ epilayer, while Fig. 4.3(b) is a HAADF image showing the region of the interface between GaAs buffer layer and $GaAsN_{0.0305}$ epilayer. There are many variations in contrast present in the dilute-nitride alloy, as visible in Figs. 4.3(a) and 4.3(b), indicating the occurrence of significant N contamination of the GaAs barrier layer

caused by the shutter-controlled system. These would be likely to severely affect the carrier extraction and transport properties of this material. The parasitic N-rich layer was again present. Figure 4.3(c) is a high magnification HAADF image, and the inserted Fig. 4.3 (d) is a higher magnification HAADF lattice image showing the $GaAsN_{0.0305}$/GaAs interface region. As the nitrogen concentration has been increased, it is clear that the $GaAsN_{0.0305}$ epilayer appears much brighter than GaAs buffer layer, implying that even more nitrogen has been incorporated interstitially into the film.

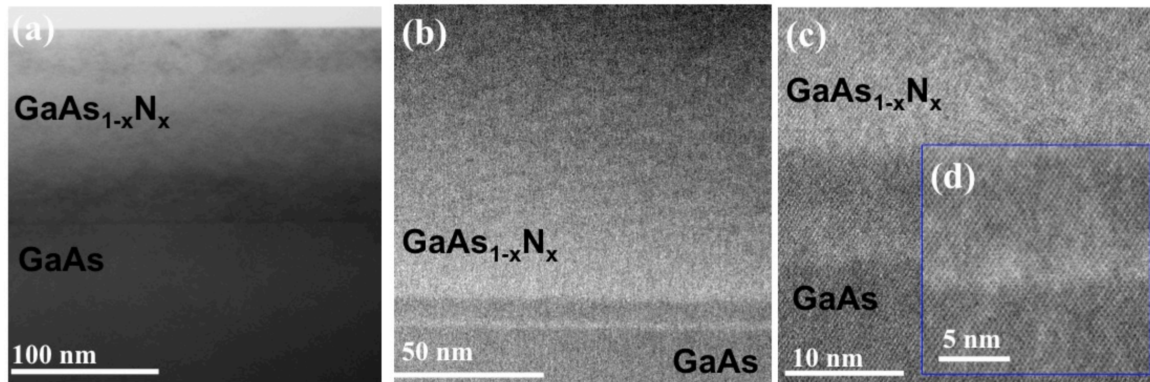


Fig. 4.3: (a) Conventional phase-contrast TEM image reveals variations in contrast in $GaAs_{1-x}N_x$ epilayer, whereas the contrast in the GaAs buffer layer is uniform by comparison. (b) HAADF-STEM image shows uniform contrast but local changes in contrast are visible in the $GaAs_{1-x}N_x$ epilayer. (c, d) HAADF-STEM lattice images of the interface region.

As more interstitial nitrogen was incorporated into the epilayer, the internal stress due to the presence of nitrogen can be expected to increase. Stress relief then occurred by cracking, as shown in Fig. 4.4(a), which is a low magnification HAADF image of the $GaAsN_{0.0367}$ epilayer. After extensive examination of many areas on several cross-sectional samples, it was found that these micro-cracks propagated predominantly along <110> directions. All of the cracks were open at the top surface, and they often penetrated through the entire dilute-nitride film into the GaAs buffer layer. Additionally,

it was significant that very few dislocations were observed in any of the dilute nitride samples. Thus, it seems that cracking must be the preferred relaxation mechanism for interstitial N-induced stress in these films. Figures 4.4(b-c) are high-magnification HAADF images revealing the interface region of the epitaxial $GaAsN_{0.0367}$ film. Similar to the previous three samples, the N-rich parasitic layer was still present beneath the dilute nitride film. The contrast in the Z-contrast images of the dilute-nitride film was higher than that of the GaAs buffer layer, again implying that a large amount of nitrogen was interstitial, consistent with the three previous samples.

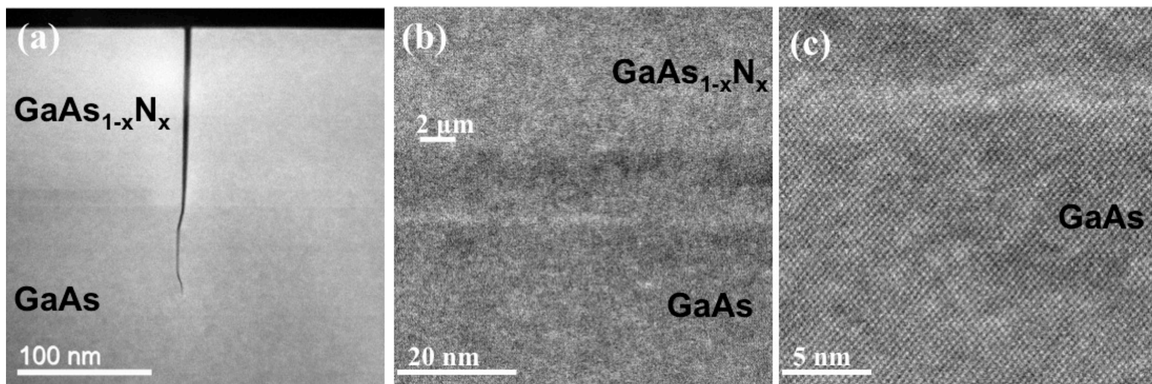


Fig. 4.4: (a) HAADF-STEM image shows a typical microcrack present in the epilayer, as sometimes observed in this highly N-doped $GaAs_{1-x}N_x$, which is attributed to the extra strain. (b, c) HAADF-STEM lattice images show interface region.

A quantitative method to determine the N content (x) in the dilute nitride $GaAsN_x$ films was applied, based on comparing the intensity differences between the $GaAsN_x$ epilayers and GaAs buffer layers. The intensity of ADF images is given by the expression $I=C[Z_e]^n$, where C is a normalization factor, $Z_e$ is the elemental atomic number, and the exponent n is considered to be 1.5 according to previous work.[24, 25] These measurements indicate that the x value is $0.56 \pm 0.02$ in $GaAsN_{0.0305}$ sample and $0.65 \pm 0.18$ in $GaAsN_{0.0367}$ sample. The large error bar for the $GaAsN_{0.0367}$ sample could be due to the

{110} microcracks causing local N variations in this sample. In order to rule out the possibility of strain affecting the contrast of the $GaAsN_x$ epilayers, a tilting experiment was performed for the $GaAsN_{0.0305}$ sample. The TEM specimen was tilted in the range of $\pm 2^o$ away from the zone axis in both X and Y directions. It was found that the higher contrast in $GaAsN_x$ epilayers compared with GaAs buffer layers was always observed regardless of the beam orientation. Thus, the higher contrast observed in $GaAsN_x$ epilayers in HAADF-STEM mode was primarily caused by the overall greater atomic weight.

Dilute-nitride quantum-well-based photovoltaic solar cells were fabricated, as shown by the schematic device structure in fig. 4.5(a). Figure 4.5(b) is a low magnification HAADF image showing the typical cross-sectional morphology of the fabricated device, which is in agreement with the expected sample structure. Figure 4.5(c) is a high-resolution HAADF image showing the *p*-doped AlGaAs epilayer of the quantum-well-based PV solar cell shown in Fig. 4.5(a). Four periods of the dilute-nitride $GaAsN_x$ ($x>0.03$) quantum well (QW) are visible in Fig. 4.5(d). Each period contained two dilute-nitride QWs with thicknesses of 6 nm and 4 nm, respectively. The high-resolution STEM lattice image in fig. 4.5(e) shows one period of the dilute-nitride QW, and confirms the high of the material crystallinity.

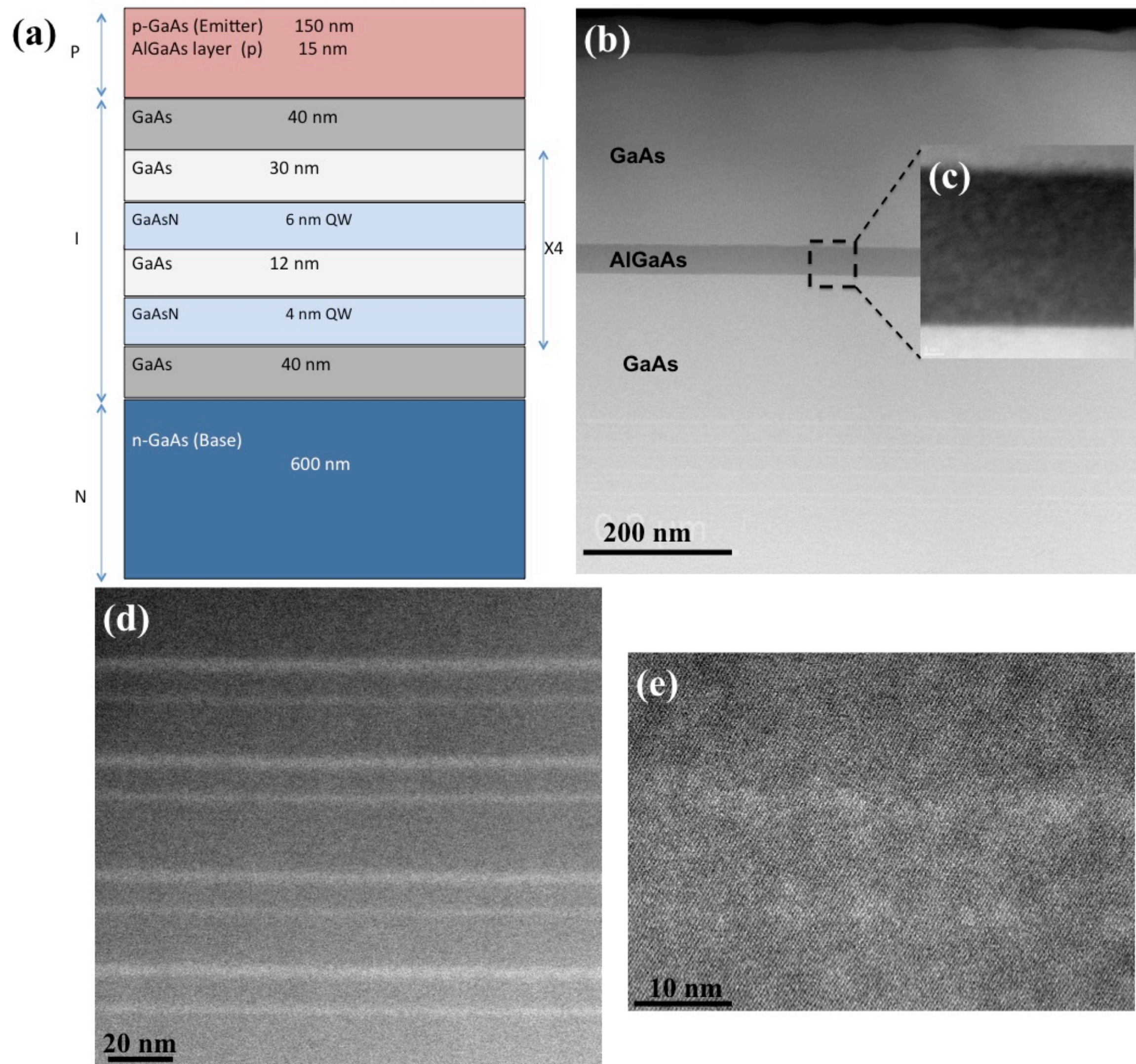


Fig. 4.5: (a) Structure schematic of dilute-nitride $GaAsN_x$ quantum-well-based solar cell. (b) HAADF-STEM image shows cross-section image showing upper part of fabricated solar cell with layers corresponding to the sample schematic. (c) HAADF-STEM lattice image showing the enlarged region of AlGaAs epilayer. (d) HAADF-STEM image showing four periods of the dilute-nitride asymmetric QW layers. (e) HAADF-STEM lattice image showing an enlarged view of one typical period of the dilute-nitride layer.

The luminescence properties of the GaAs quantum-well sample were measured by PL (see Fig. 4.6), and the dilute-nitride-based device showed a band gap energy of 1.19 eV (1040 nm). This value indicates that the high-nitrogen-content ($x>0.03$) alloy can play a functional role in this solar cell.

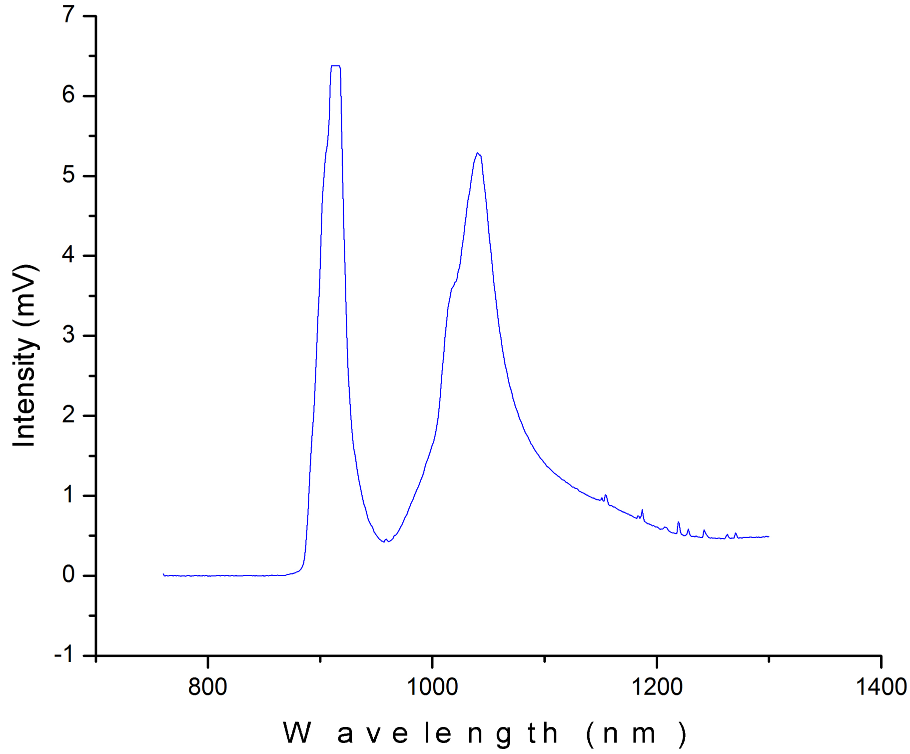


Fig. 4.6: PL spectrum from the dilute-nitride $GaAsN_x$ QW-based solar cell.

The incorporation of nitrogen into the dilute nitride $GaAsN_x$ layers is crucial for explaining the contrast of the HAADF-STEM images. It was significant that all of the $GaAsN_x$ layers had brighter contrast than the GaAs buffer layers, with the relative image contrast increasing with higher N concentration. Previous studies have assumed that N atoms occupied substitutional sites of the dilute-nitride alloy films, with static atomic displacement (SAD) around substitutional N atoms inducing strained $GaAs_{1-x}N_x$ layers which would cause higher contrast in HAADF-STEM images[20,21] due to enhanced scattering to high angle via a static Debye-Waller effect.[22] However, this mechanism does not seem satisfactory to explain the higher contrast of the relatively thick dilute nitride films (~100 nm) investigated in our study. Substantial interstitial N incorporation into the

dilute nitride epilayers would seem to be a more likely reason for the higher contrast of the HAADF-STEM images because it would cause higher overall atomic weight $GaAsN_x$ layers compared with the GaAs layers. According to previous studies, RBS channeling measurements showed significant concentrations of interstitial N in non-annealed dilute nitride films.[18] By comparing N concentrations measured by high-resolution X-ray diffraction and secondary-ion mass spectroscopy, it was found that a signification amount of nitrogen was incorporated interstitially into the dilute-nitride $GaAsN_x$ film.[17] Our present HAADF-STEM imaging results agree well with this finding. Although the current study does not provide any detailed information about the N configuration in the dilute nitride films, it is interesting to note that previous studies have suggested that the most likely arrangement of interstitial N is the N-As complex.[17,23]

## 4.4 Conclusions

In this study, dilute-nitride $GaAsN_x$ epilayers were grown using plasma-assisted molecular/chemical beam exitaxy. The formation of a thin (parasitic) N-doped layer which correlated with the plasma ignition process was observed. The nitrogen incorporated into the dilute-nitride film was found to be primarily interstitial, and local [N] composition fluctuations occurred during the dilute nitride growth. Post-growth partial relaxation of strain through the formation of {110}-oriented microcracks occurred in the sample with the highest nitrogen composition. The structural characterization of as-grown dilute nitride films revealed the conservation of pseudomorphism and widespread absence of strain-relieving dislocations.

REFERENCES


[1] G. Pozina, I. Ivanov, B. Monemar, J. V. Thordson, and T. G. Andersson, Journal of Applied Physics **84** (7), 3830 (1998).

[2] S. Zhang and S.-H. Wei, Physical Review Letters **86** (9), 1789 (2001).

[3] M. Weyers and M. Sato, Applied Physics Letters **62** (12), 1396 (1993).

[4] Y. Zhang, A. Mascarenhas, H. Xin, and C. Tu, Physical Review B **63** (16), 161303 (2001).

[5] K. Uesugi, N. Morooka, and I. Suemune, Applied Physics Letters **74** (9), 1254 (1999).

[6] U. Tisch, E. Finkman, and J. Salzman, Applied Physics Letters **81** (3), 463 (2002).

[7] T. Taliercio, R. Intartaglia, B. Gil, P. Lefebvre, T. Bretagnon, U. Tisch, E. Finkman, J. Salzman, M. A. Pinault, M. Laügt, and E. Tournié, Physical Review B **69** (7), 073303 (2004).

[8] V. Virkkala, V. Havu, F. Tuomisto, and M. J. Puska, Physical Review B **88** (3),035204 (2013).

[9] A. Freundlich, A. Fotkatzikis, L. Bhusal, L. Williams, A. Alemu, W. Zhu, J. A. H. Coaquira, A. Feltrin, and G. Radhakrishnan, Journal of Crystal Growth **301-302**, 993 (2007).

[10] M. A. Green, K. Emery, Y. Hishikawa, W. Warta, and E. D. Dunlop, Progress in Photovoltaics: Research and Applications **20** (1), 12 (2012).

[11] W. Li, M. Pessa, J. Toivonen, and H. Lipsanen, Physical Review B **64** (11), 113308 (2001).

[12] D. Kwon, R. J. Kaplar, S. A. Ringel, A. A. Allerman, S. R. Kurtz, and E. D. Jones, Applied Physics Letters **74** (19), 2830 (1999).

[13] S. Y. Xie, S. F. Yoon, and S. Z. Wang, Journal of Applied Physics **97** (7), 073702 (2005).

[14] S.J. Pennycook, P.D. Nellist, Microscopy and Microanalysis **6** (04), 343 (2000).

[15] M. A. Pinault, A. Freundlich, J. A. H. Coaquira, and A. Fotkatzikis, Journal of Applied Physics **98** (2), 023522 (2005).

[16] C. Wang, D. J. Smith, S. Tobin, T. Parodos, J. Zhao, Y. Chang, and S. Sivananthan, Journal of Vacuum Science & Technology A: Vacuum, Surfaces, and Films **24** (4), 995 (2006).

[17] W. J. Fan, S. F. Yoon, W. K. Cheah, W. K. Loke, T. K. Ng, S. Z. Wang, R. Liu, and A. Wee, Journal of Crystal Growth **268** (3-4), 470 (2004).

[18] S.G. Spruytte, M. C. Larson, W. Wampler, C.W. Coldren, H.E. Petersen, J.S. Harris, Journal of Crystal Growth **227-228**, 506 (2001).

[19] G. K. Vijaya, A. Freundlich, D. Tang, and D. J. Smith, Jour. Vac. Sco. Tech. B (2014), submitted.

[20] X. Wu, M. D. Robertson, J. A. Gupta, and J. M. Baribeau, Journal of Physics: Condensed Matter **20** (7), 075215 (2008).

[21] T. Grieb, K. Muller, R. Fritz, M. Schowalter, N. Neugebohrn, N. Knaub, K. Volz, and A. Rosenauer, Ultramicroscopy **117**, 15 (2012).

[22] D. D. Perovic, C. J. Rossouw, and A. Howie, Ultramicroscopy **52** (3-4), 353 (1993).

[23] M. Herrera, Q. Ramasse, D. Morgan, D. Gonzalez, J. Pizarro, A. Yáñez, P. Galindo, R. Garcia, M. H. Du, S. Zhang, M. Hopkinson, and N.J. Browning, Physical Review B **80** (12), 125211 (2009).

[24] S. Chung, Characterization of electrostatic potential of compound semiconductors using off-axis electron holography (2009).

[25] L Li, Determination of electrostatic potential and charge distribution of semiconductor nanostructures using off-axis electron holography (2011).

# CHAPTER 5

# INVESTIGATION OF MONOLAYER/MULTI-LAYER InAs QUANTUM DOTS ON $GsAs_{1-x}Sb_x$/GaAs COMPOSITE SUBSTRATES FOR PHOTOVOLTAIC SOLAR CELLS

The research described in this chapter was carried out in collaboration with Yeongho Kim, Dr. Nikolai Faleev and Prof. Christiana Honsberg in the School of Electrical, Computer and Energy Engineering at Arizona State University. The primary purpose of this research has been to contribute towards the development of an absorber layer for intermediate-band solar cells (IBSC). My role in this work has been to perform microstructural characterization using electron microscopy, and to correlate structural properties with optoelectronic behavior. The MBE growth, the XRD and PL measurements described in this chapter were carried out by Yeongho Kim in Prof. Christiana Honsberg's group.

## 5.1 Introduction

Intermediate-band solar cells (IBSC) based on a single-junction layer were predicted to possess conversion efficiencies in excess of 60 % under maximum concentration of sunlight.[1,2] This possibility attracted much attention as a radically different approach towards the realization of photovoltaic solar cells with high conversion efficiencies overcoming the Shockley-Queisser (SQ) limit.[3] In order to implement the IBSC, self-assembled quantum dots (SAQDs) were preferred rather than quantum wells, because they provide a true null density of states between the

intermediate band (IB) and the conduction band (CB), and allow for light absorption from the IB to the CB.[4,5] Since this concept was first proposed, prototype IBSCs using various types of III-V compound semiconductor quantum dots (QDs) grown on GaAs substrates have been reported.[6-10] Among these, InAs/GaAs QDs are widely used as a test-bed material system. However, the relatively large valence band offset (VBO) of InAs/GaAs results in a significant loss of open circuit voltage ($V_{oc}$).[11] In addition, the large lattice mismatch between InAs and GaAs (~7%) causes the generation of misfit and/or threading dislocations as strain builds up in thicker layers. Moreover, the degraded performance of single-junction InAs/GaAs cells, which is due to the relatively weak absorption coefficients of the VB-IB and IB-CB transitions, requires the achievement of a high volumetric concentration of QDs in order to enhance the overall photon absorption. One typical approach to overcoming these problems is to induce a strain-reduced (SR) barrier layer capping the InAs QDs, such as GaAsSb, which is in tensile strain, to offset the residual compressive strain associated with the QDs/wetting layers (WLs). The InAs/GaAsSb QD system is considered as one of the most promising candidates to be utilized for IBSCs since GaAsSb barrier layers can minimize the VBO of the whole QD system by variation of the Sb content.[12,13] In addition, the InAs/GaAsSb material system has also been demonstrated to enhance optical properties because of high QD density and improved QD size uniformity.[14]

In this work, the structure-performance properties of single-layered and multi-layered InAs/$GaAs_{1-x}Sb_x$ QD system has been investigated as a function of different Sb concentrations and layer periods. The structural properties were determined using various electron microscopy techniques, as well as high-resolution X-ray diffraction (XRD)

analysis and atomic force microscopy (AFM). The optoelectronic properties were measured by photoluminescence (PL) spectra, specifically by continuous-wave PL and time-resolved PL. Detailed correlations between the microscopy results and the PL measurements have been made and are also briefly discussed.

## 5.2 Results & Discussion

### 5.2.1 Characterization of single-layered InAs/GaAsSb QDs

A group of five single-layered InAs/GaAsSb QD structures incorporated with a Si delta (δ) doping layer were grown, as described in section 2.1.3 of Chapter 2. The structure of these single-layered samples is illustrated in Fig. 5.1. The InAs QDs consist of 2 monolayers (ML) of InAs embedded in 20-nm-thick GaAsSb barrier layers with two different Sb concentrations, which are 8% and 20%, respectively. According to previous study, InAs/$GaAs_{0.92}Sb_{0.08}$ QDs possess type-I energy band alignment, and InAs/$GaAs_{0.8}Sb_{0.2}$ QDs possess type-II energy band alignment.[11] The Si δ-doping layer introduced beneath the QD layer plays an important role in controlling the occupied subbands of the InAs/GaAsSb system by acting as a carrier reservoir. The key parameters of the five samples (intended Sb concentration, δ-doping density, and expected energy band alignment) are summarized for reference in Table 5.1.

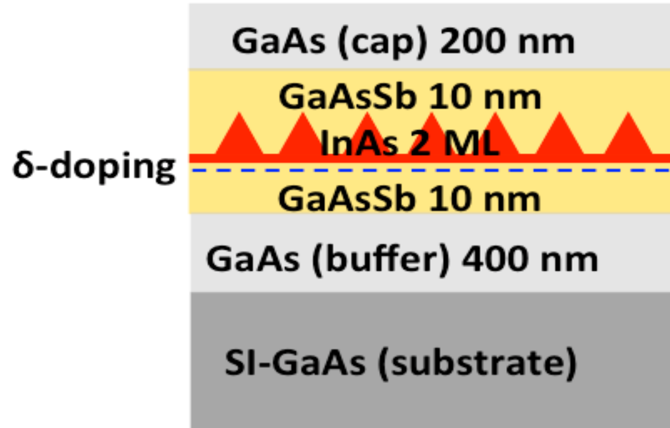


Fig. 5.1 Structural schematic of single-layered InAs/GaAsSb QDs.

Table 5.1 Five single-layered InAs/GaAsSb QDs incorporated with a Si delta layer, with their corresponding responding δ-doping density, intended Sb content and expected type of energy band alignment.

| Sample | δ-doping density ($cm^{-2}$) | Intended Sb content (%) | Expected energy band alignment |
|---|---|---|---|
| 1 | $5 \times 10^{10}$ | 8 | Type-I |
| 2 | $2 \times 10^{12}$ | | |
| 3 | $5 \times 10^{10}$ | 20 | Type-II |
| 4 | $2 \times 10^{12}$ | | |
| 5 | 0 | | |

Figure 5.2 is a typical high-resolution HAADF-STEM image showing the cross-sectional morphology of the single-layered InAs/GaAsSb structure with highest Sb concentration and δ-doping density (sample #4). The image clearly shows the InAs QDs embedded in the GaAsSb barrier layer, as marked by the red arrows. The Si δ-doping line is shown right underneath the InAs QDs layer. No significant growth defects were

observed after characterizing many areas on two different TEM specimens, which confirmed that the GaAsSb barrier layer played an important role in relaxing the strain between InAs and GaAs. After examining many different areas, no significant structural differences between the highest Sb content sample (#4) and lowest Sb content sample (#2) were observed. This observation indicates that although the Sb concentration plays a role in controlling the energy band structure there is no effect on the overall morphology. However, it was also interesting to observe that the lower interface between the GaAs buffer layer and the GaAsSb barrier layer was relatively much flatter compared with the upper one between the GaAsSb barrier layer and the GaAs capping layer, which is presumably because the curvature of the upper interface was strongly affected by the InAs QDs because of residual strain remaining in the GaAsSb barrier layer. This curvature may also affect the morphology of lateral grown InAs QDs as the multiple-layered QD structure is built up.

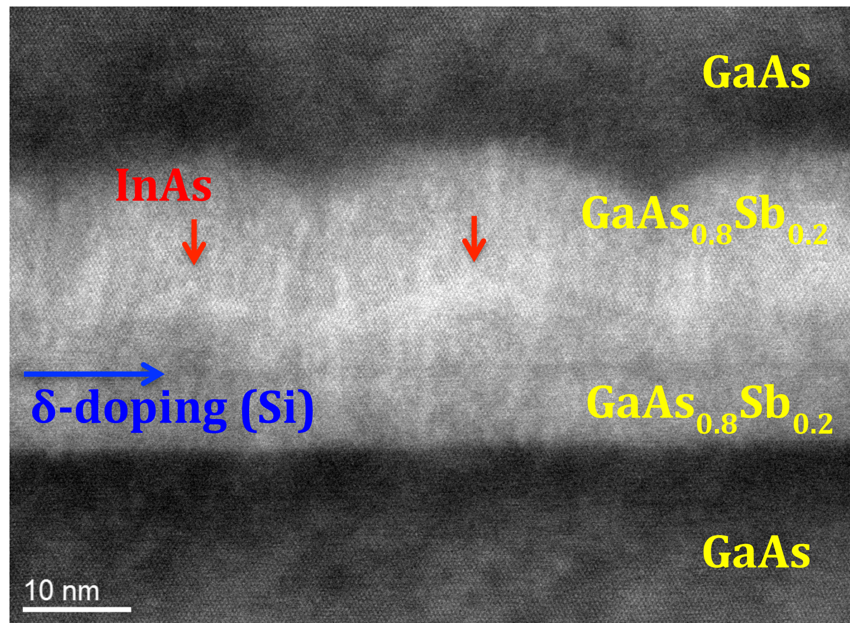


Fig. 5.2 High-resolution HAADF-STEM image of self-assembled single-layered InAs QDs on GaAsSb/GaAs.

5.2.2 Characterization of multi-layered InAs/GaAsSb QDs with different Sb concentration

To enhance absorption efficiency, high volumetric concentrations of InAs were achieved by growing multi-layered QDs. A group of three multi-layered InAs/GaAsSb QD samples (10×) with different Sb concentration was grown by varying the Sb to As flux ratio during growth. The sample structures of these three multi-layered InAs/GaAsSb QD samples are illustrated in the schematic of Fig. 5.3.

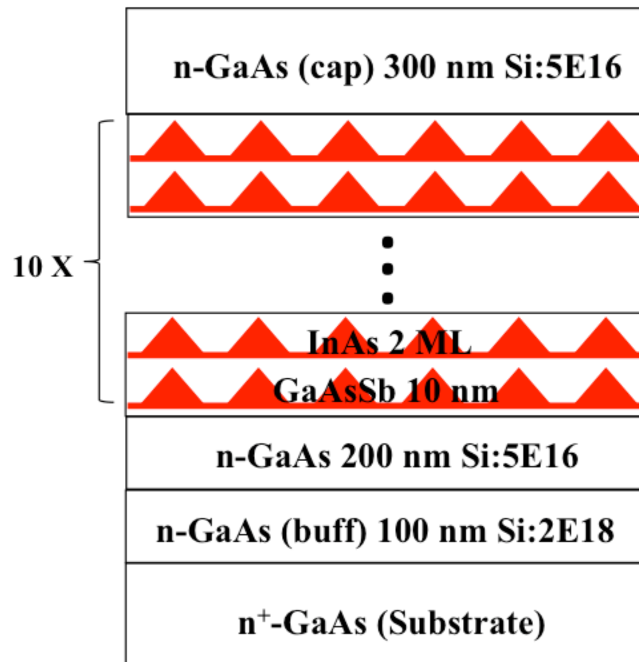


Figure 5.3 Structural schematic of multi-layered (10×) InAs/GaAsSb QD samples.

Before examination of these three samples by electron microscopy, high-resolution XRD was used for composition analysis and defect analysis. Figures 5.4-5.6 show the XRD patterns of these three multi-layered InAs QD samples using double crystal ω-2θ scans. The simulation results (red curves) below each measurement agree closely with the experimental data (blue curves). The Sb concentrations in the GaAsSb

barriers layers of those three samples were intended to be 7%, 10% and 15%, respectively. However, as shown in Fig. 5.7, which is a HR-XRD double crystal ω-2θ scans patterns of all three samples, the Sb compositions of these samples were determined using curve fitting and Vegard's law to be 7.25% (G13-069), 9.8% (G13-070) and 10.2% (G13-071), respectively.

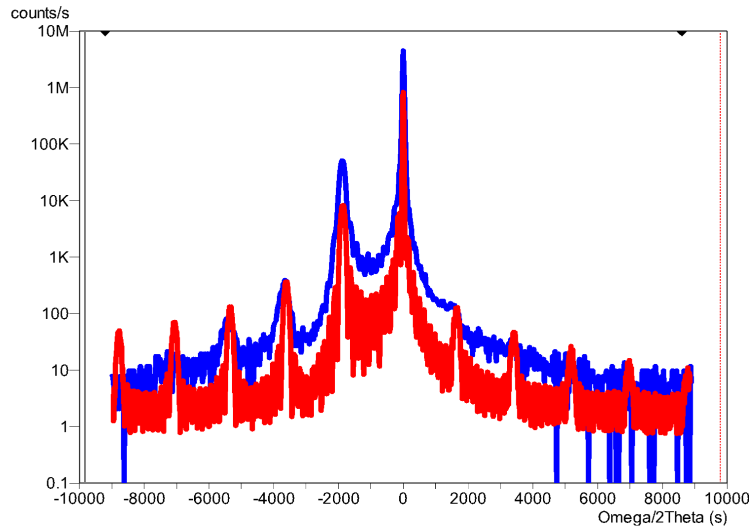


Fig. 5.4 XRD pattern (blue curve) of sample G13-069 using double crystal ω-2θ scan with its corresponding simulated pattern (red curve).

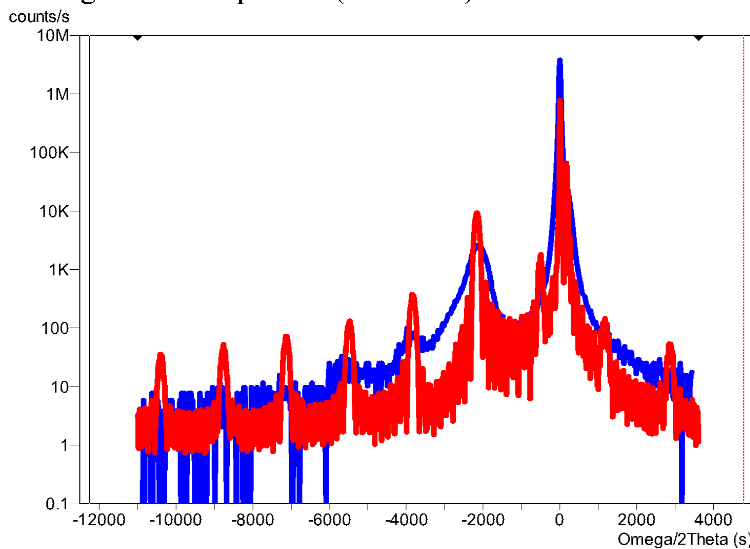


Fig. 5.5 XRD pattern of sample G13-070 using double crystal ω-2θ scan with its corresponding simulated pattern (red curve).

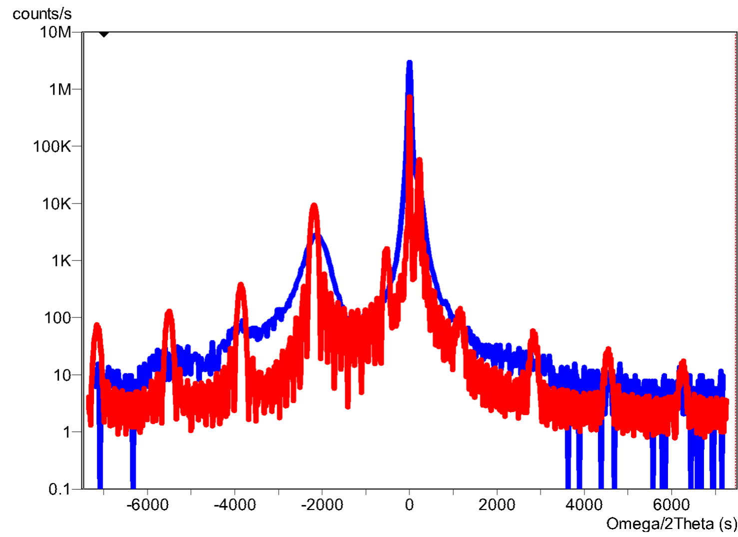


Fig. 5.6 XRD pattern of sample G13-071 using double crystal ω-2θ scan with its corresponding simulated pattern (red curve).

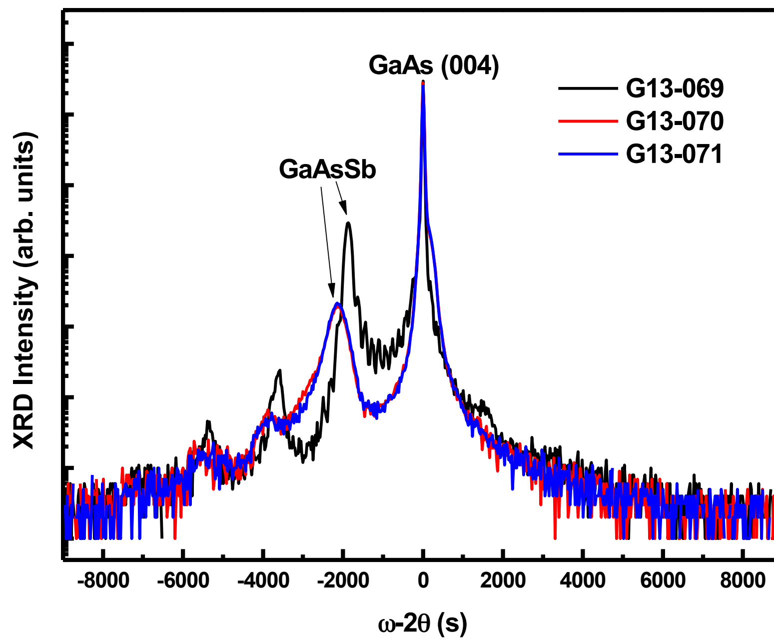


Fig. 5.7 XRD patterns for three multi-layered InAs QD samples (G13-069, G13-070, G13-071) using double crystal ω-2θ scans.

Detailed analysis of the XRD curves was further used for estimating the dislocation densities of the three samples, as shown in Fig. 5.8, which is a XRD ω-scan The peak (blue curve) for sample G13-069 appears to have a primary peak and a secondary peak, and the density of dislocation loops is calculated to be $8 \times 10^4$ (primary) and $1.6 \times 10^8$ (secondary), respectively, based on the full width at half maximum (FWHM) of these two peaks. The value of $8 \times 10^4$ based on measurement of the primary peak should represent the dislocation density for this sample according to the TEM characterization results that are discussed later. The densities of dislocation loops for samples G13-070 and G13-071 were calculated to $2 \times 10^9$ and $3.6 \times 10^9$, respectively. The strain relaxation in the GaAsSb barrier layers was also estimated using XRD reciprocal space maps (RSMs): the percentage of strain relaxation in the GaAsSb barrier layers of these three samples was determined based on (224) asymmetric scans, as shown in Figs 5.9 (a-c). Figure 5.9 (a) is the reciprocal space map for the lowest Sb content sample (G13-069), and shows that the GaAs peak almost lines up with the GaAsSb peak, which indicates very small relaxation in the GaAsSb barrier layer. With increasing Sb composition (G13-070 and G13-071), diffraction spots around the GaAs peak were elongated along the ω-direction due to the increased lattice mismatch between GaAs and GaAsSb, as marked by the red arrows in Figs. 5.9 (b-c). This indicates partial strain relaxation with increasing Sb composition. The percentages of strain relaxation in the GaAsSb barrier layers of these three samples were calculated to be 0% (G13-069), 18% (G13-070) and 23 % (G13-071), respectively. These numerical findings are summarized in Table 5.2 for reference.

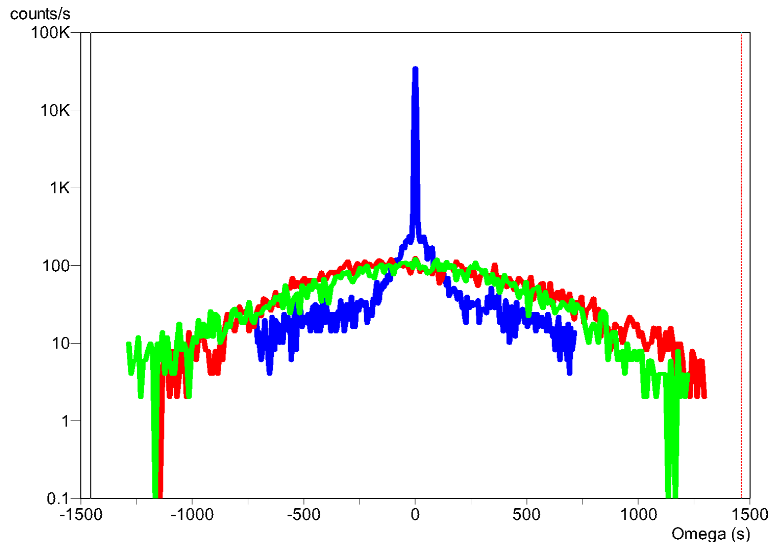


Fig.5.8 XRD patterns of samples G13-069 (blue), G13-070 (red) and G13-071 (green) used for determining dislocation densities.

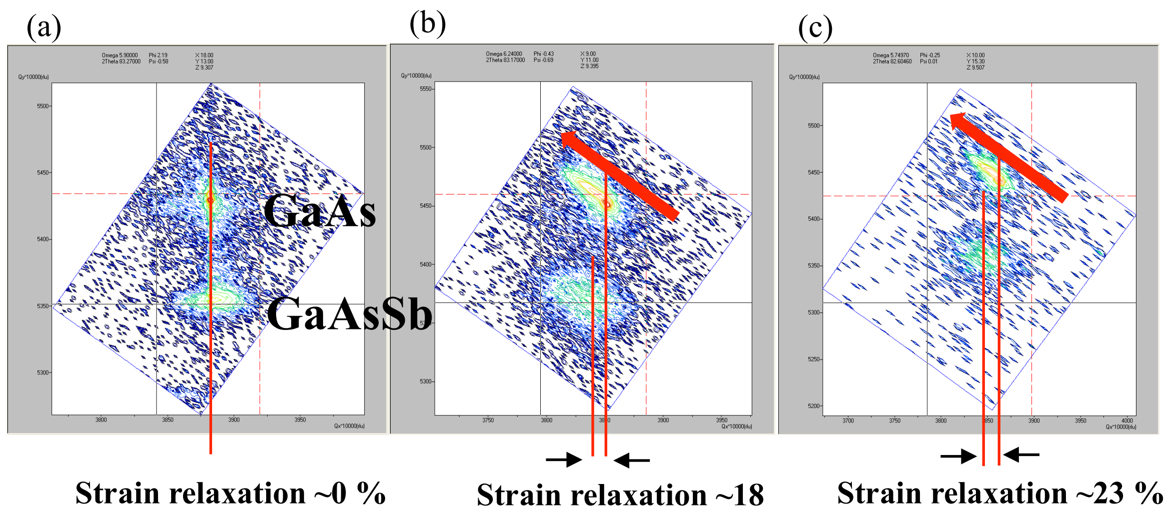


Fig. 5.9 XRD reciprocal space maps based on (224) asymmetric scan for samples (a) G13-069, (b) G13-070, and (c) G13-071.

Table 5.2 Measurement of Sb content, relaxation and dislocation density for three multi-layered (10×) InAs/GaAsSb QD samples.

| Sample | Expected Sb content (%) | Measured Sb content (%) | Relaxation (%) | Density of Dislocation Loops ($cm^{-2}$) |
|---|---|---|---|---|
| G13-069 | 7 | 7.25 | ~8 | $8 \times 10^4$<br>$1.6 \times 10^8$ |
| G13-070 | 10 | 9.80 | ~18 | $2 \times 10^9$ |
| G13-071 | 15 | 10.20 | ~23 | $3.6 \times 10^9$ |

It was interesting that the Sb concentration of G13-071 was almost the same as in G13-070 even though the Sb to As flux ratio during growth of the former was higher than the latter. This might be due to Sb incorporation in the GaAs barrier layers under the same growth conditions, which resulted in similar concentrations. According to previous study of this particular InAs/GaAsSb QD system, the band alignment transition from type-I to type-II occurred between 13% and 15% of Sb concentration, based on the observation of blue-shift and carrier lifetime increment in PL spectra.[11] Similar to previous results, all three of the multi-layered QD samples in this study were found to have type-I band alignments.

The three multi-layered InAs/GaAsSb QD samples were prepared for cross-sectional TEM characterization. Figures 5.10 are typical HAADF-STEM images showing the cross-sectional morphologies of these samples. From these micrographs, it is clear that the self-assembled InAs QDs are lined up along the growth direction for the full 10 periods. From comparing these three Z-contrast images, it seems that sample 069 has

smaller contrast differences between the GaAs buffer layer and the GaAsSb barrier layers relative to samples 070 and 071, which confirmed that sample 069 had lowest Sb concentration.

InAs wetting layers for deposition of each individual QD layer were observed clearly in HAADF-STEM images, such as Fig. 5.11, which indicated the Stranski-Krastanov growth mode of these QDs. However, as predicted from characterization of the single-layered QD samples, the wetting layers became more and more interrupted as the QD layers build up, which might be due to residual strain induced by the QDs underneath. The trend of curvature of the InAs wetting layers is clear in Fig. 5.12, which shows four higher-magnification HAADF-STEM images with ten well-aligned self-assembled QDs for the specific QD column observed in Fig. 5.11. It is also interesting to notice that the shapes of the InAs QDs has evolved from well-defined to not-well-defined as the number of layers builds up, as clearly shown in Fig. 5.11.

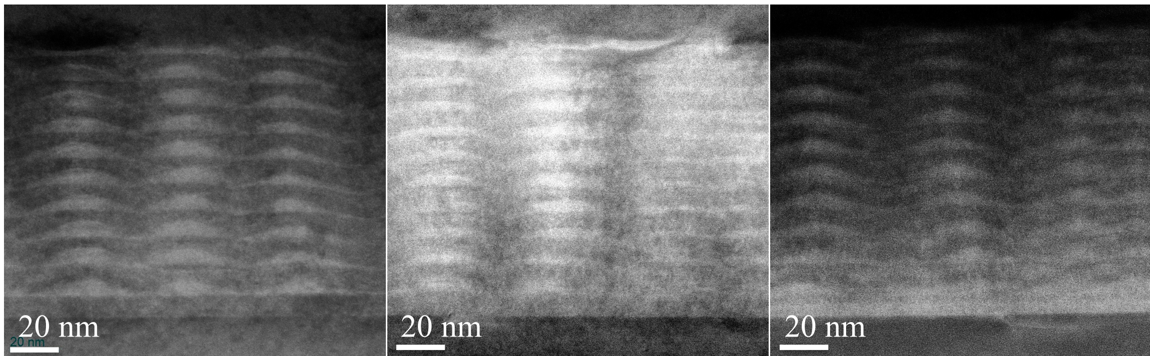


Fig. 5.10 (a) HAADF-STEM image showing sample 069 with 10 periods of self-assembled InAs QDs on $GaAs_{0.93}Sb_{0.07}$ barrier layers; (b) HAADF-STEM image showing sample 070 with 10 periods of self-assembled InAs QDs on $GaAs_{0.90}Sb_{0.10}$ barrier layers; (c) HAADF-STEM image showing sample 071 with 10 periods of self-assembled InAs QDs on $GaAs_{0.85}Sb_{0.15}$ barrier layers.

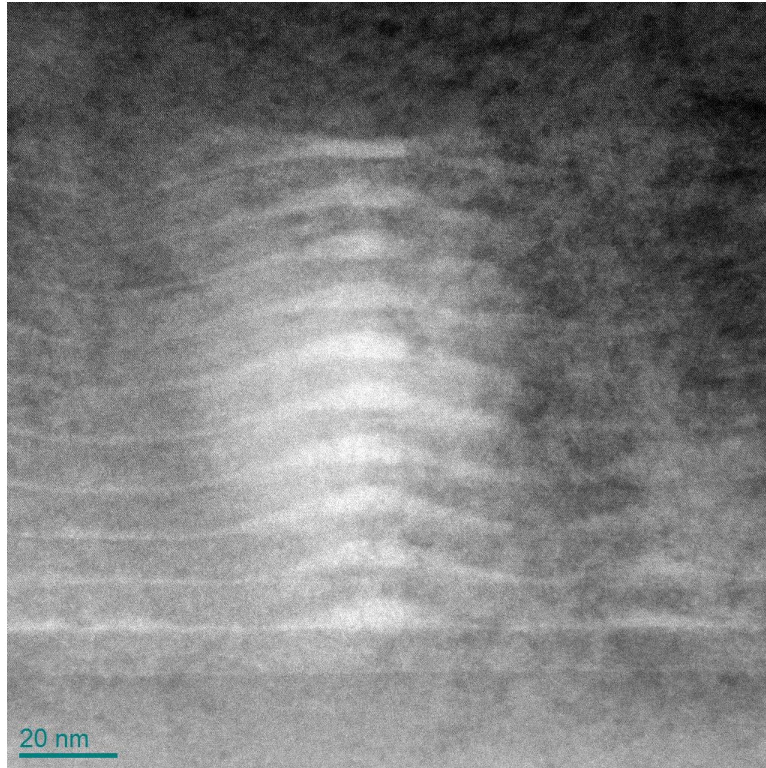


Fig. 5.11 HAADF-STEM image showing a single column of self-assembled InAs QDs on $GaAs_{0.93}Sb_{0.07}$ barrier layers.

High-resolution HAADF-STEM imaging was also used for studying individual InAs QDs, as shown in Fig. 5.12. Figure 5.12 (a) is a HAADF-STEM lattice image showing typical InAs QDs in the first, second and third layers. It is clearly revealed that the QD in the first layer has a well-defined triangular shape with flat InAs wetting layer underneath. However, the QDs above the second layer become elongated, which is most likely caused by the curved InAs wetting layer beneath. The curvature of the InAs wetting layers and the elongation of InAs QDs appeared more and more obvious as the QD stacks build up, as shown in Figs. 5.12 (b-d). It was also noticed that the contrast of GaAsSb barriers layers was not uniform, as clearly observed in the lattice images of Figs 5.12 (c-d). These contrast variations could be due to the overlap of multiple QDs along the beam direction or residual strain in the GaAsSb barrier layers. Careful examination of

the other two multi-layered InAs/GaAsSb QDs samples was also performed. Similar trends in shape during QD evolution were also observed.

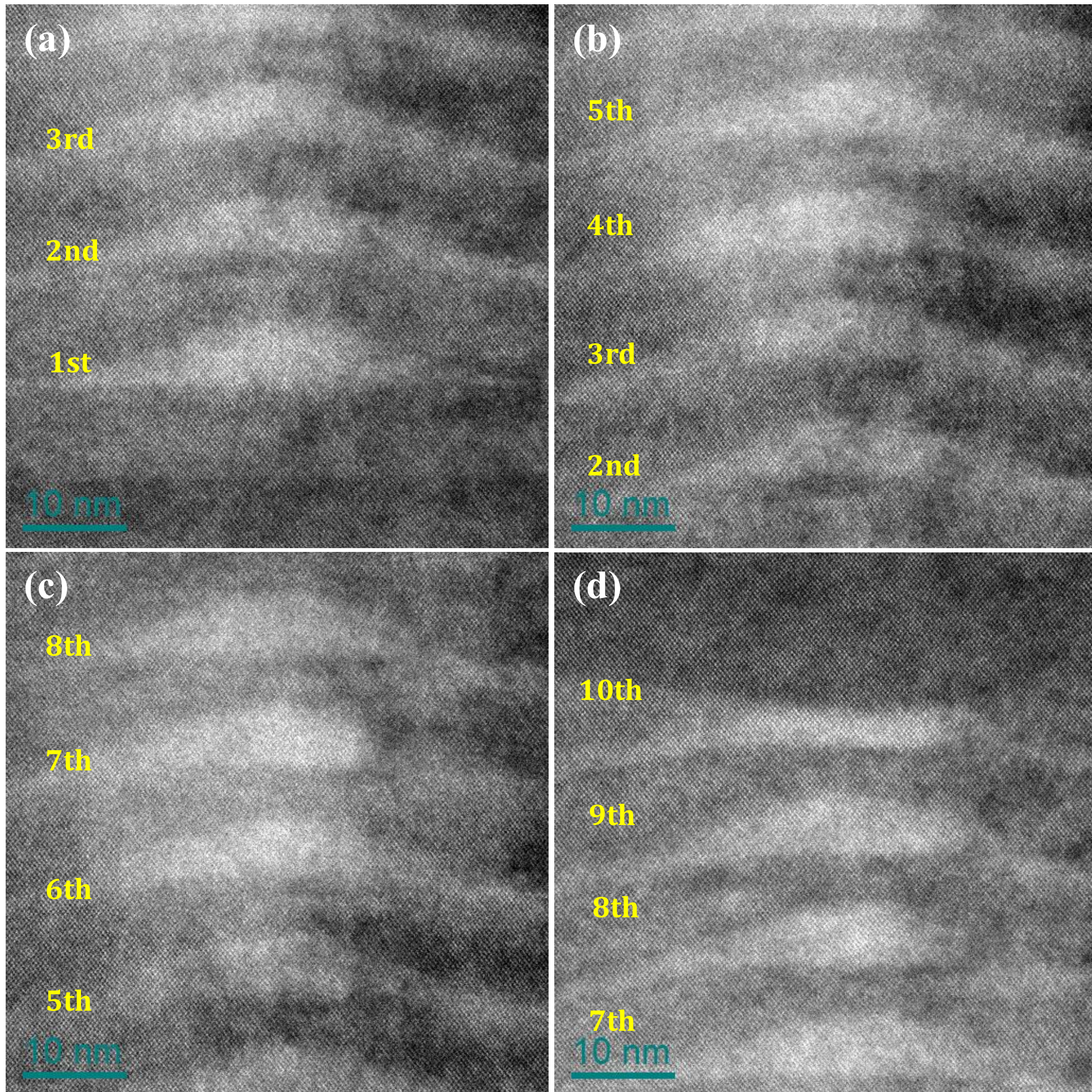


Figure 5.12 HAADF-STEM images showing ten well-aligned InAs QDs on $GaAs_{0.93}Sb_{0.07}$ in the specific QD column observed in Fig. 5.11.

These three InAs QD on GaAsSb barrier layers samples were also examined using TEM imaging. Figures 5.13 (a-c) are diffraction-contrast TEM images showing the cross-sectional morphologies of the three samples (069, 070 and 071). Sample 069 with lowest

Sb concentration did not show any dislocations after examining extensive areas on this sample, indicating that the dislocation density of this sample must be very low. Reconsidering the calculated dislocation density using XRD, it seems that the calculated value of $8 \times 10^4$ for the primary peak should be a reasonable number compared with the calculated value of $1.6 \times 10^8$ for the secondary peak, since the dislocations would be easily observed if the dislocation density was really so high. Figures 5.13 (b and c) are the TEM images showing the cross-sectional morphologies of sample 070 and sample 071. Although they have similar Sb concentrations according to XRD, it is clear that sample 071 has higher dislocation density than sample 070, which is consistent with the calculated dislocation densities from XRD. These dislocations are likely to act as recombination centers for electron-hole pairs, which would degrade the optical performance of QD-based IBSCs.

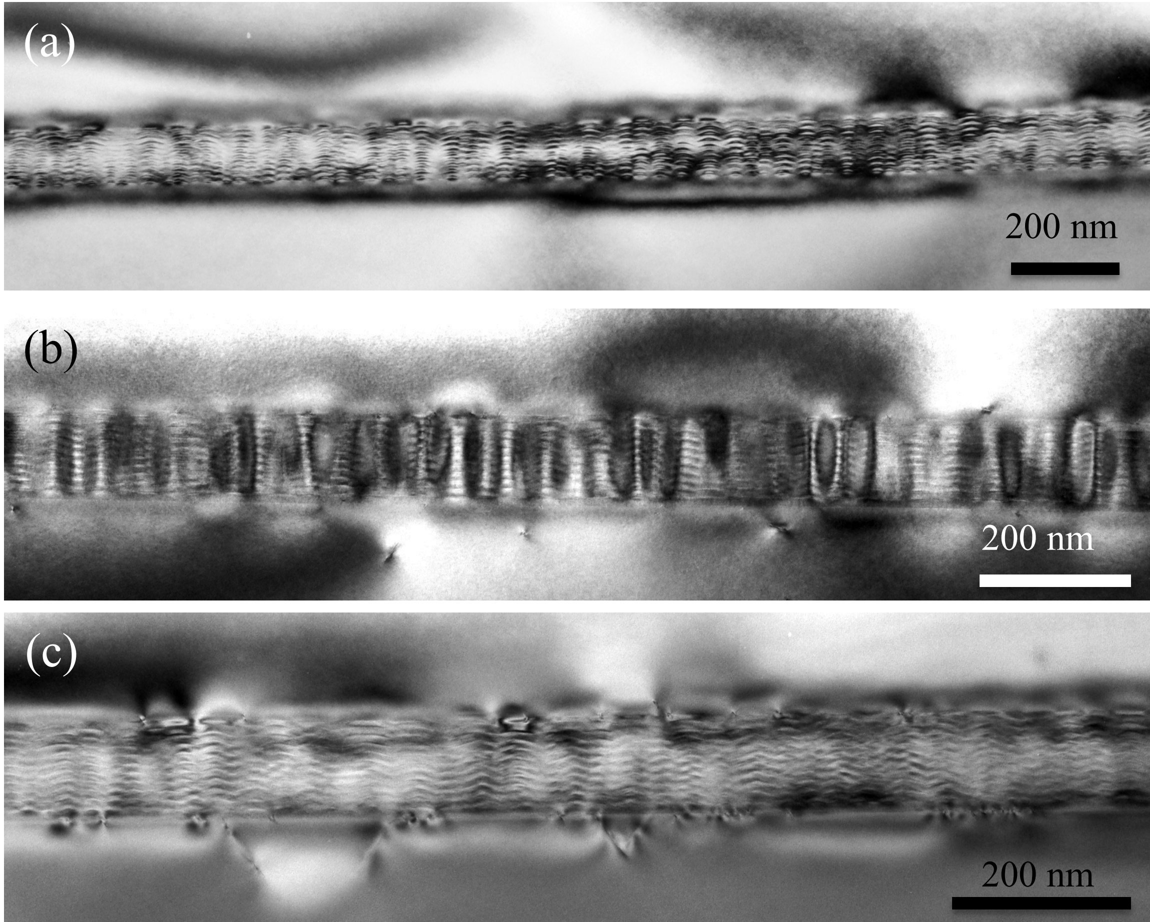


Fig. 5.13 (a) HR-TEM image showing sample 069 with 10 periods of self-assembled InAs QDs on $GaAs_{0.93}Sb_{0.07}$ barrier layers; (b) HR-TEM image showing sample 070 with 10 periods of self-assembled InAs QDs on $GaAs_{0.90}Sb_{0.10}$ barrier layers; (c) HR-TEM image showing sample 071 with 10 periods of self-assembled InAs QDs on $GaAs_{0.85}Sb_{0.15}$ barrier layers.

Continuous-wave PL (cw-PL) spectra for these three samples were obtained, as shown in Fig. 5.14. The PL peak energies of these three samples were calculated to be 1.168 eV (G13-069), 1.117 eV (G13-070) and 1.123 eV ((G13-071), respectively. The PL emission peak of sample 070 is red-shifted by ~51 meV with respect to the peak of sample 069, and the PL emission peak of sample 071 is red-shifted by ~45 meV with respect to the peak of sample 069, as marked in Fig. 5.14. This red-shift can be explained by the increased strain relief provided in the InAs QDs samples with increased Sb

concentration in the barrier layers. However, the emission peak of sample 071 is blue-shifted by ~6 meV compared to sample 070, which may be due to the large strain relaxation of GaAsSb barrier layers provided by the extra dislocations.

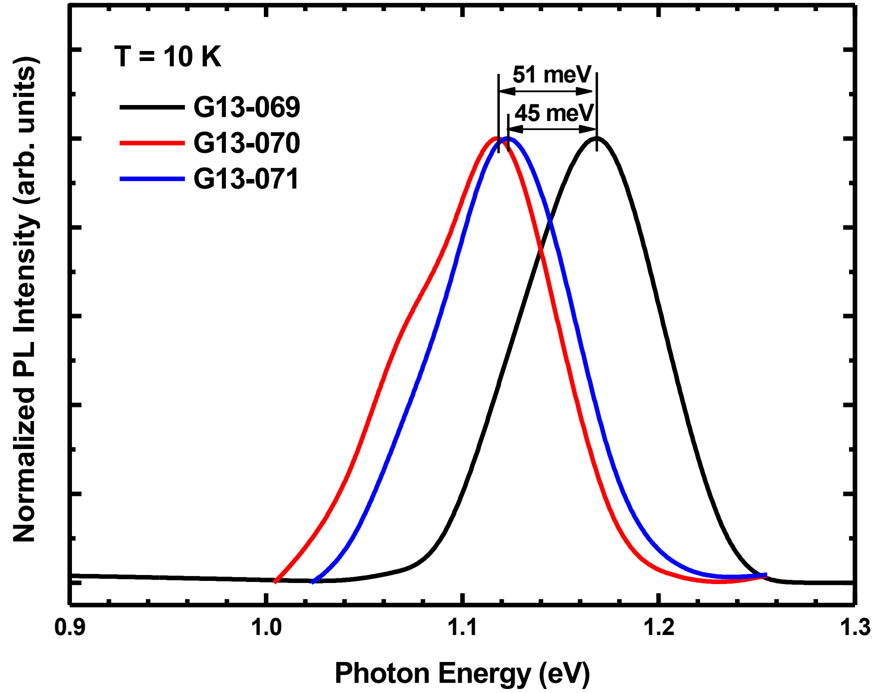


Fig. 5.14 cw-PL spectra of samples 069 (black curve), 070 (red curve) and 071 (blue curve) recorded at 10 K. Peak shift to lower energy corresponds to longer wavelength emission.

It was pointed out previously that the band alignment in InAs/GaAsSb QDs can be shifted from type-I to type-II by varying the Sb concentration in GaAsSb barrier layers.[11,13] Furthermore, the type of band alignment must be identified from the emission peak shift in the excitation power-dependent PL. For these reasons, the PL spectra for these three samples were obtained for a series of increasing excitation powers from 0.05 mW up to 10 mW at 10 K, as shown in Figs. 5.15 (a-c). It is clearly shown that sample 069 possesses a red shift of about ~0.04 eV, while sample 070 and sample 071 possess significant blue shift about ~0.05 eV and ~ 0.07 eV, respectively. As a result, it can be

concluded that sample 070 and 071 have type II band alignment. This means that there is spatial separation between electrons in the InAs QDs and holes in the GaAsSb barrier layers, resulting in the band bending induced by the electric field across the InAs/GaAsSb interface and the observed blue shift reported earlier.[11,15-17]

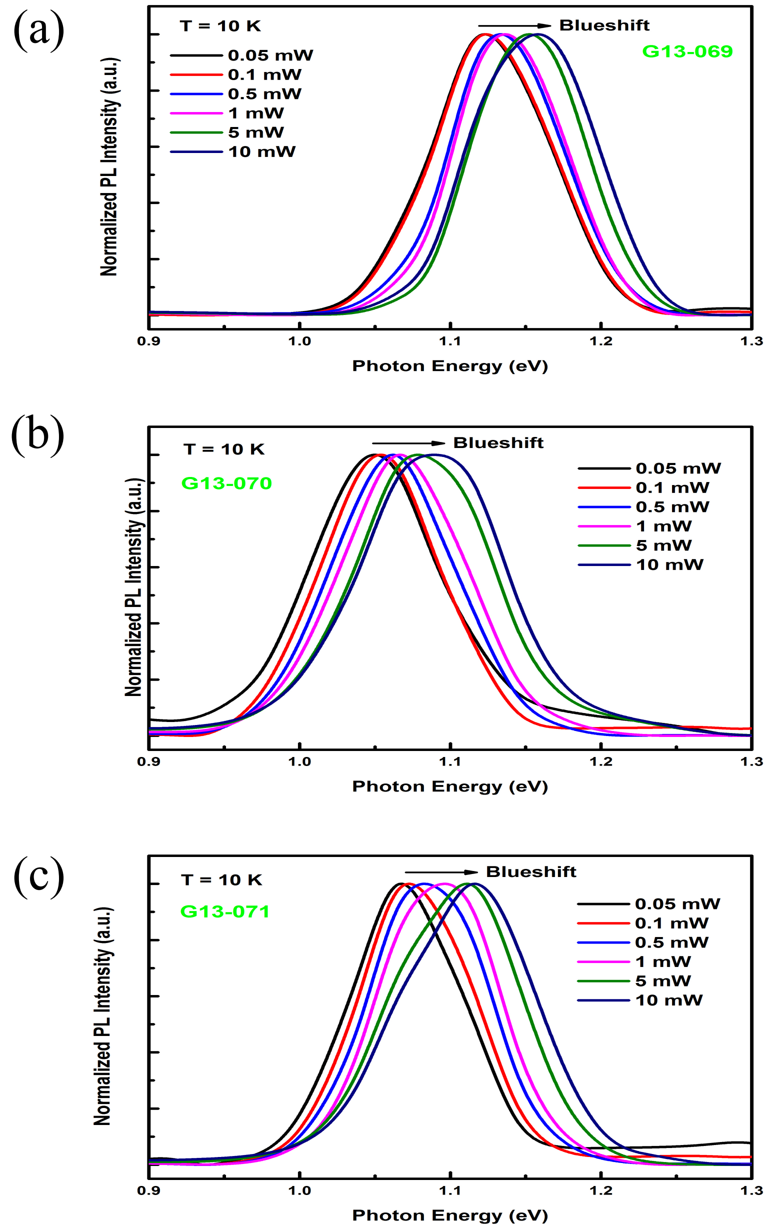


Fig. 5.15 Power-dependent PL spectras of samples (a) 069, (b) 070 and (c) 071.

5.2.3 Characterization of multi-layered InAs/GaAsSb QDs with different layer periods

In order to determine the optimal number of QD layer stacks for growing an IBSC absorber, a group of four multi-layered InAs/$GaAs_{0.8}Sb0_{.2}$ samples was further grown, with different number of stack periods increasing from 5 to 30 in steps of 5. The sample structure of this sample set is illustrated in Fig. 5.16, which is a schematic showing the overall structure of this sample set.

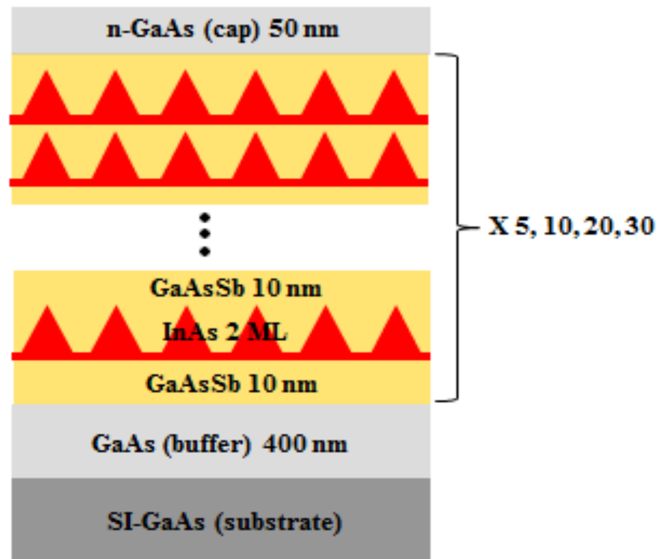


Fig. 5.16 Structural schematic of multi-layered InAs/$GaAs_{0.80}Sb0_{.20}$ QDs with different numbers of QD stacks.

All of the samples in this sample set were prepared for cross-sectional microscopy characterization. Figure 5.17 is a low-magnification HAADF-STEM image showing the cross-sectional morphology of the five-layered (5×) InAs/$GaAs_{0.8}Sb_{0.2}$ QD sample. It is interesting to notice the dark shadow-like contrast surrounding each QD column, which could indicate residual strain between the InAs QDs and the GaAsSb barrier layers. This type of dark contrast also appeared along the interface between GaAs buffer layer and the first InAs/GaAsSb QD layer, and at the interface between the fifth InAs/GaAsSb QD

layer and GaAs capping layer, which could be attributed to lattice mismatch between GaAs and InAs.

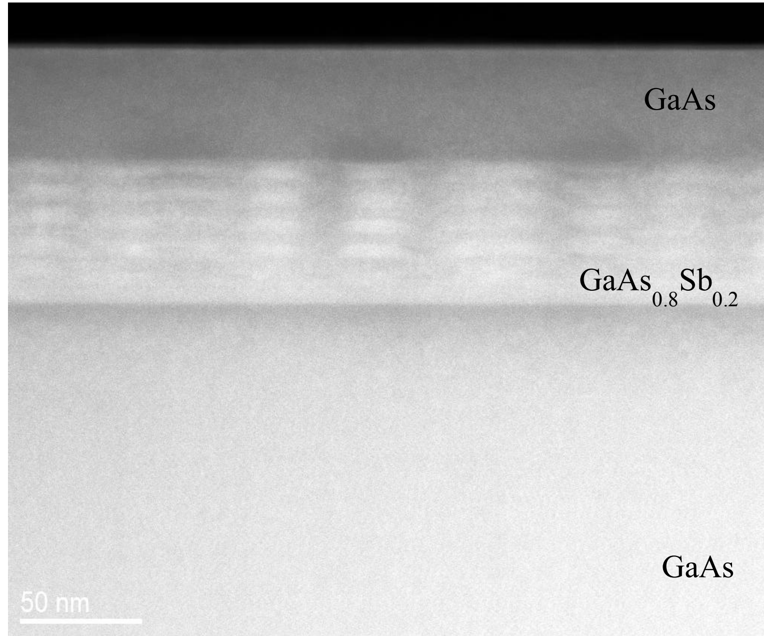


Fig. 5.17 HAADF-STEM image of 5× InAs/$GaAs_{0.8}Sb_{0.2}$ QD sample.

Figure 5.18 is a low-magnification HAADF-STEM image showing the cross-sectional morphology of the twenty-layered (20×) InAs/$GaAs_{0.8}Sb_{0.2}$ QD sample. It clearly shows that a lot of defects such as stacking faults and dislocations occurred in the first QD layer extending up to the top QD layer. This generation of significant amounts of defects must be due to the accommodation of residual strain in the GaAsSb barrier layers. These defects will most likely cause degraded device performance. More HR-TEM observations are still needed for charactering these defects in more detail.

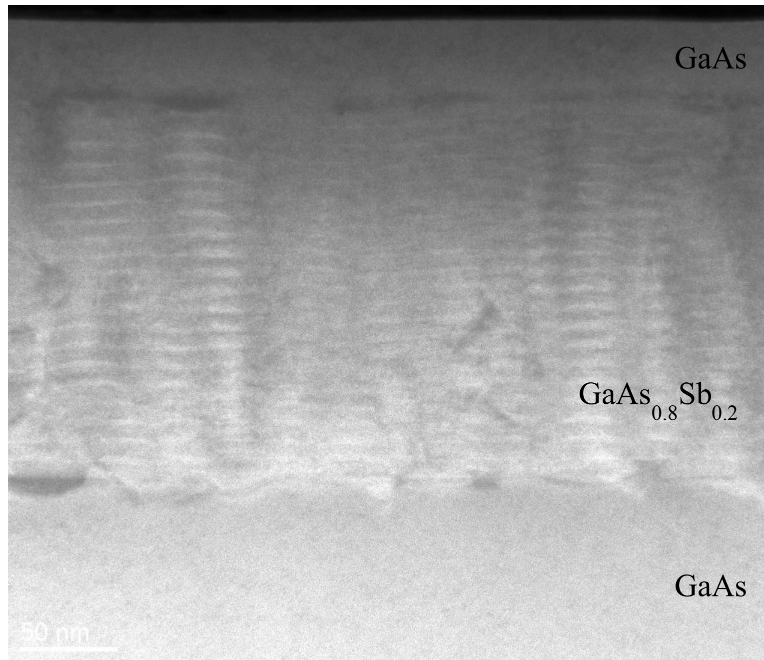


Fig. 5.18 HAADF-STEM image of 20× $InAs/GaAs_{0.8}Sb0_{.2}$ QD sample.

5.3 Conclusions

The structural properties of the InAs/GaAsSb QD system have been investigated systematically using electron microscopy techniques. The Sb concentrations played an important role for tuning the energy band alignments based on PL spectra, but without greatly impacting the structural morphology. The residual strain of the InAs QDs can be partially offset by the GaAsSb barrier layers. According to both XRD measurement and electron microscopy, the densities of dislocation increases as the Sb concentration increases and the number of QD layers builds up. These dislocations could act as nonradioactive recombination centers for electron-hole pairs which would decrease the photogenerated carriers, and lead to further degradation of carrier lifetime in the QD-based IBSCs. Additionally, the shape of the InAs QDs evolved from a well-defined to less-well-defined due to residual strain beneath the QDs, which may be the starting point for generating additional defects that could degrade the performance of the IBSCs.

REFEREMCE


[1] A. Luque and A. Marti, Physical Review Letters **78** (26), 5014 (1997).

[2] A. Luque, A. Marti, and L. Cuadra, IEEE T Electron Dev **48** (9), 2118 (2001).

[3] W. Shockley and H. J. Queisser, Journal of Applied Physics **32** (3), 510 (1961).

[4] A. Marti, L. Cuadra, and A. Luque, IEEE T Electron Dev **48** (10), 2394 (2001).

[5] S. Tomic, T. S. Jones, and N. M. Harrison, Applied Physics Letters **93** (26) (2008).

[6] A. Marti, E. Antolin, C. R. Stanley, C. D. Farmer, N. Lopez, P. Diaz, E. Canovas, P. G. Linares, and A. Luque, Physical Review Letters **97** (24) (2006).

[7] P. G. Linares, A. Marti, E. Antolin, and A. Luque, Journal of Applied Physics **109** (1) (2011).

[8] V. Popescu, G. Bester, M. C. Hanna, A. G. Norman, and A. Zunger, Physical Review B **78** (20) (2008).

[9] Q. Shao, A. A. Balandin, A. I. Fedoseyev, and M. Turowski, Applied Physics Letters **91** (16) (2007).

[10] M. Y. Levy and C. Honsberg, IEEE T Electron Dev **55** (3), 706 (2008).

[11] K.-Y. Ban, D. Kuciauskas, S. P. Bremner, and C. B. Honsberg, Journal of Applied Physics **111** (10), 104302 (2012).

[12] K. Akahane, N. Yamamoto, and N. Ohtani, Physica E **21** (2-4), 295 (2004).

[13] H. Y. Liu, M. J. Steer, T. J. Badcock, D. J. Mowbray, M. S. Skolnick, P. Navaretti, K. M. Groom, M. Hopkinson, and R. A. Hogg, Applied Physics Letters **86** (14) (2005).

[14] K.-Y. Ban, S. P. Bremner, G. Liu, S. N. Dahal, P. C. Dippo, A. G. Norman, and C. B. Honsberg, Applied Physics Letters **96** (18), 183101 (2010).

[15] T. T. Chen, C. L. Cheng, Y. F. Chen, F. Y. Chang, H. H. Lin, C. T. Wu, and C. H. Chen, Physical Review B **75** (3) (2007).

[16] Q. Liu, S. Derksen, A. Linder, F. Scheffer, W. Prost, and F. J. Tegude, Journal of Applied Physics **77** (3), 1154 (1995).

[17] Y. S. Chiu, M. H. Ya, W. S. Su, and Y. F. Chen, Journal of Applied Physics **92** (10), 5810 (2002).

# CHAPTER 6

# MICROSCOPIC CHARACTERIZATION OF InAs QUANTUM DOTS INCORPORATED WITH AlAs/GaAs SPACER LAYERS

The research described in this chapter was carried out in collaboration with Manori Gunasekera and Prof. Alex Freundlich at the Center for Advanced Materials at University of Houston. The primary purpose of this research has been to contribute towards the development of near-wetting layer-free (Volmer-Weber type) InAs quantum dots on GaAs. My role in this work has been to carry out microstructural characterization using electron microscopy to investigate the structural properties. The MBE growth described in this chapter was carried out by Prof. Freundlich's group.

## 6.1 Introduction

Self-assembled quantum dots (QDs) are formed in many semiconductor compounds of III-V material family using the Stranski-Krastanov (SK) growth mode.[1] Using this approach, it has been demonstrated that In(Ga)As QDs are formed on GaAs (100) substrates by InAs deposition above a certain critical thickness followed by GaAs overgrowth.[2] These In(Ga)As/GaAs compound materials can be used for various optoelectronic applications in the 1.3-1.55 μm wavelength range,[3-5] such as photovoltaic solar cells. However, it is impossible to obtain 0-dimensional (0D) carrier confinement, and the QD properties are generally uncontrollable, due to the presence of a wetting layer, for growth of InAs QDs via the SK mode.[6] Recently, a molecular beam epitaxy (MBE) growth regime has been found based on the deposition of sub-critical InAs coverage for

obtaining InAs QDs, suggesting a transition from the Stranski-Kranstanov (SK) mode to a V-W-like QD arrangement.[7] The near-wetting layer-free InAs QDs or V-W-like QDs may possess desired and controllable optoelectronic properties, as well as 0D carrier confinement, due to the absence of InAs wetting layer, which may lead to improvement in the performance of InAs QD-based photovoltaic applications.[6]

This work describes the growth of near-wetting layer-free InAs QDs carried out using the approach of insertion of AlAs or GaAs spacer layers between the InAs wetting layers and subsequent QDs. The structural properties of these near-wetting layer-free QDs incorporated with spacer layers have been studied and correlated with the optoelectronic properties measured by photoluminescence (PL). This study also contributes towards understand the growth kinetics of InAs QDs and the QD transition between the SK and VW-like growth modes.

## 6.2 Results & Discussion

Three samples were designed for this study containing both conventional SK InAs QDs and near-wetting layer-free QDs, as described in section 2.1.4 of Chapter 2.

Two types of InAs QDs were targeted during the material growth, one type was the conventional InAs QD grow on GaAs (100), and the other was the near-wetting layer-free InAs QDs incorporated with AlAs or GaAs spacer layer. The evolution of the reflection high-energy electron diffraction (RHEED) patterns for both types of QDs in terms of average facet orientation, dot size, strain and anisotropic behavior were monitored during the QD formation as a function of the targeted spacer layer thickness, as shown in Fig. 6.1. Figure 6.1(a) is the RHEED pattern for conventional InAs QDs

grown on GaAs showing the QD formation followed the SK mode with higher base/height aspect ratio bound by lower index planes {137} and dot diameters in the range of 4-5 nm. Figure 6.1 (b) is a typical RHEED pattern for InAs QDs incorporated with AlAs/GaAs spacer layers with relatively lower base/height aspect ratio bound by index planes {11n} (1<n<2) and dot diameters in the range of 4-9 nm. This pattern further suggests that the InAs QDs incorporated with the spacer layer were near-wetting layer free followed by the VW growth mode.

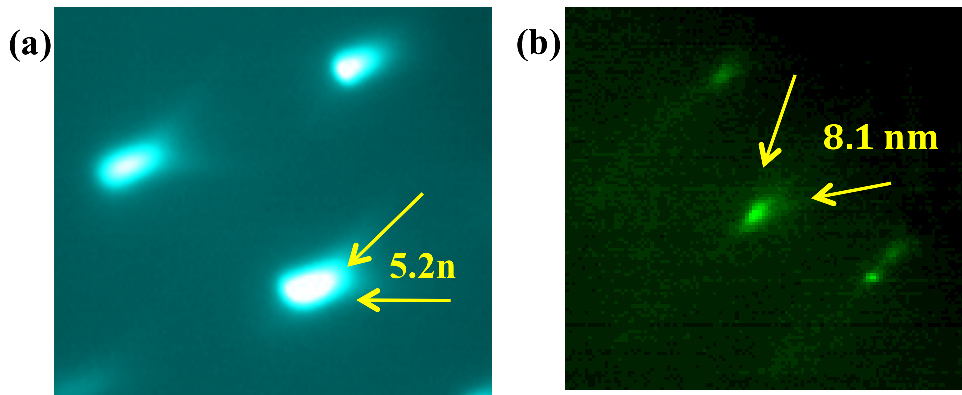


Fig. 6.1 (a) RHEED pattern for conventional InAs QDs on GaAs (100) (b) RHEED pattern for InAs QDs incorporated with GaAs spacer layer on GaAs (100).

These observations were complemented by post-growth AFM analysis of uncapped InAs dots, as shown in Figs. 6.2 (a-c), which are (a) plan-view AFM images of conventional InAs QDs on GaAs (100), (b) InAs QDs incorporated with 3 ML GaAs spacer layer and (c) InAs QDs incorporated with 3 ML AlAs spacer layer, respectively. The scales of these three AFM images are 0.05 μm × 0.05 μm. A detailed tomographic analysis based on AFM was performed and the numerical findings of major parameters, such as density, mean height, base length and base width of QDs were made, as summarized in table 6.1. Based on the AFM analysis, it was revealed that the InAs QDs

incorporated with spacers layer had smaller dot density and more symmetrical large sizes, with an apparent bimodal size distribution (two distinct families of large and small dots), comparied with conventional InAs QDs without spacer layer. Moreover, the conventional InAs QDs had a large dot density and appeared to be elongated along [110], as shown in Fig.6.2 (a).

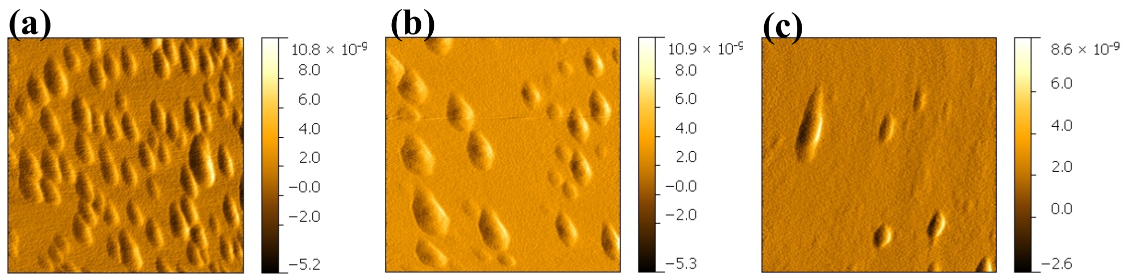


Fig. 6.2 (a) AFM image showing conventional InAs QDs grown on GaAs (100). (b) AFM image showing InAs QDs incorporated with 3 ML GaAs spacer layer on GaAs (100). (c) AFM image showing InAs QDs incorporated with 3 ML AlAs spacer layer on GaAs (100). Scales of three AFM images are 0.05 μm × 0.05 μm.

Table 6.1 Numerical findings of density, mean height, base length and base width of QDs.

| | QD Density ($nm^{-2}$) | Mean Height (nm) | Base Length (nm) | Base Width (nm) |
|---|---|---|---|---|
| Conventional InAs QDs | $2.3 \times 10^{-4}$ | 4-8 | 40-80 | 30-40 |
| InAs QDs incorporated with GaAs spacer | $0.94 \times 10^{-4}$ | 3-9 | 50-60 | 21 |
| InAs QDs incorporated with AlAs spacer | $0.6 \times 10^{-4}$ | 3-4 | 70 | 30 |

6.2.1 Characterization of InAs QDs incorporating with AlAs spacer layer

The first sample (#1) contained the conventional embedded SK-type InAs QDs and the near-wetting layer-free InAs QDs incorporated with AlAs spacer layer. Both

capped near-wetting layer-free QDs and uncapped near-wetting layer-free QDs were grown in this sample. Detailed sample schematic is illustrated in Fig. 6.3.

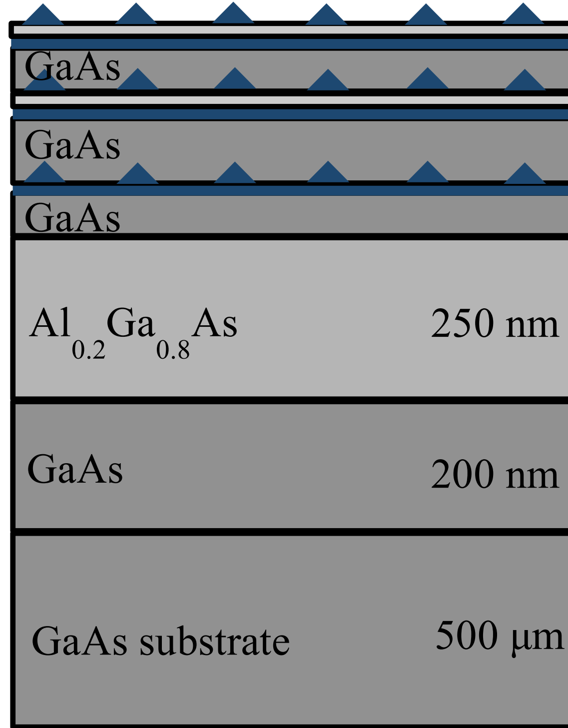


Fig 6.3 Structural schematic of sample #1 containing embedded conventional SK-type InAs QDs, embedded VW-type InAs QDs incorporated with AlAs spacer layer, and uncapped VW-type InAs QDs incorporated with AlAs spacer layer.

Figure 6.4 is a low-magnification TEM image showing the cross-sectional structure of sample #1. Three QD layers are expected to be observed as marked by the red arrows on this image. The first QD layer is the uncapped near-wetting layer-free InAs QDs incorporated with AlAs spacer layer, the second QD layer is the embedded near-wetting layer-free InAs QDs incorporated with AlAs spacer layer, and the third QD layer is the embedded conventional SK-type InAs QDs. From this image, it is clearly seen that the second and third layers exist. However, after carful examination on many areas from several samples, the uncapped near-wetting layer-free InAs QD layer (first layer) was not

observed. By comparing the embedded near-wetting layer-free InAs QDs (second layer) with the conventional SK-type InAs QDs (third layer), it seemed that the density of SK-type QDs was higher than near-wetting layer-free QDs and these QDs also had larger size. This observation is consistent with the AFM measurements of uncapped conventional SK type InAs QDs and uncapped near-wetting layer-free InAs QDs, as shown in Table 6.1. Defects such as <111> stacking faults, appeared obviously in both QD layers.

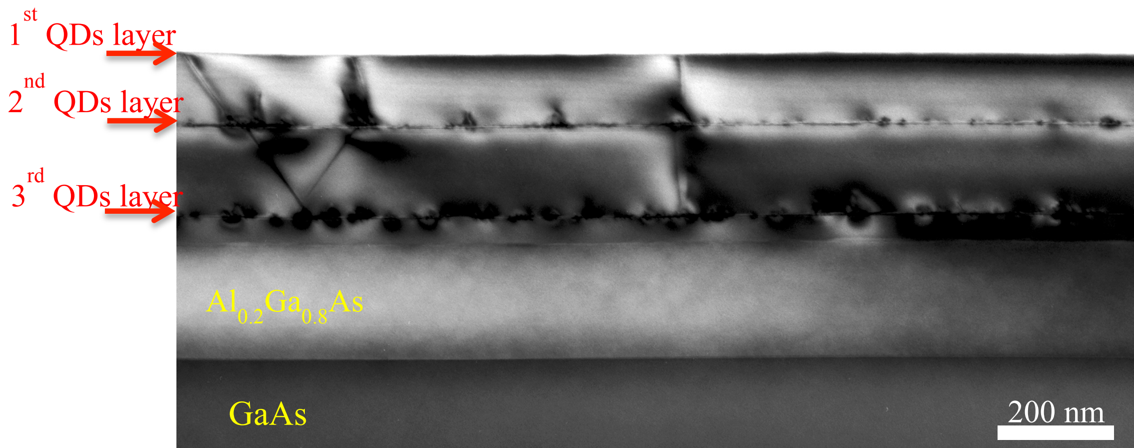


Figure 6.4 HR-TEM image of sample #1 containing uncapped VW-type InAs QDs (1st layer), capped near-wetting layer-free InAs QDs (2nd layer) and conventional embedded SK-type InAs QDs (3rd layer).

Figure 6.5 (a) is a low-magnification HAADF-STEM image of the same sample. An EDS linescan was performed along the direction of blue arrow in Fig. 6.5 (a) and the compositional profiles are shown in Fig. 6.5(b). From these line profile, Ga, As and Al signals were observed consistent with the sample structure. However, the In signal was not clearly visible. From HAADF-STEM images, it was revealed that only two embedded InAs QD layers were observed, and the uncapped near-wetting layer-free InAs QDs incorporated with AlAs spacer layer on the top surface of the sample were not observed in agreement with the TEM characterization. The absence of any observation of the

surface QDs may be due to oxidation in air, because AlAs is extremely hydrophilic. The oxidized AlAs layer is very brittle and likely to peel off, so that any surface InAs QDs are removed. The HAADF-STEM image also gave clear Z-contrast of the InAs wetting layers, as marked by the red arrows.

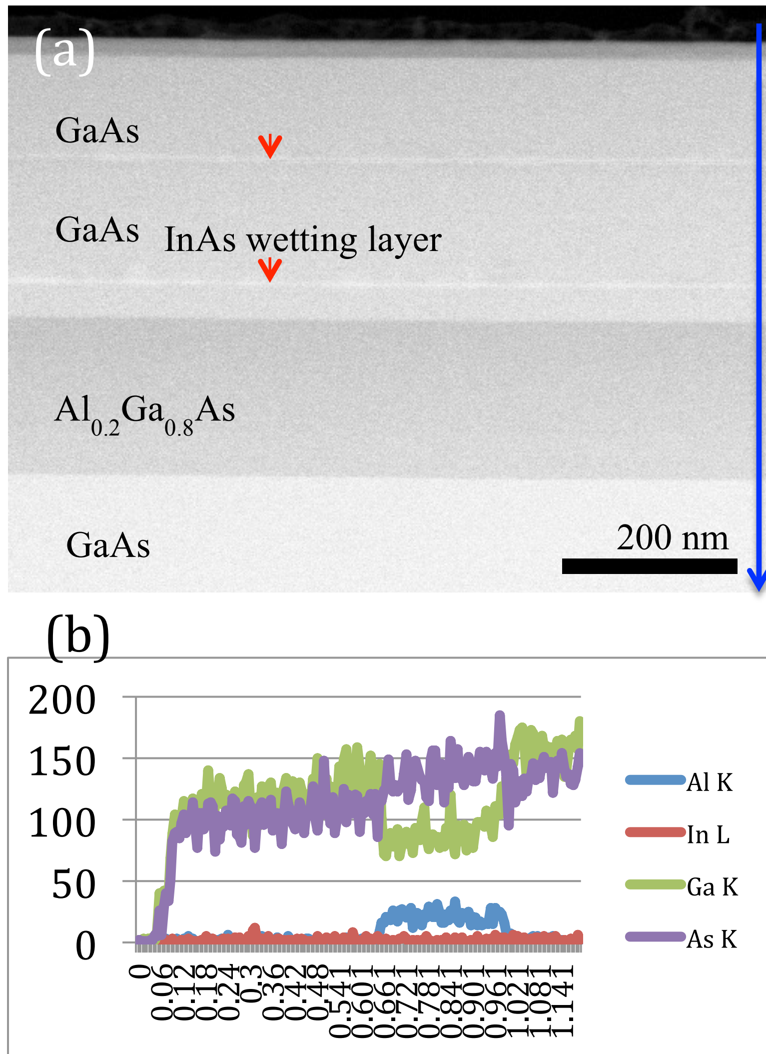


Figure 6.5 (a) Low-magnification HAADF-STEM image showing the structure of sample #1. (b) EDS line-scan profile along the direction of blue arrow in (a).

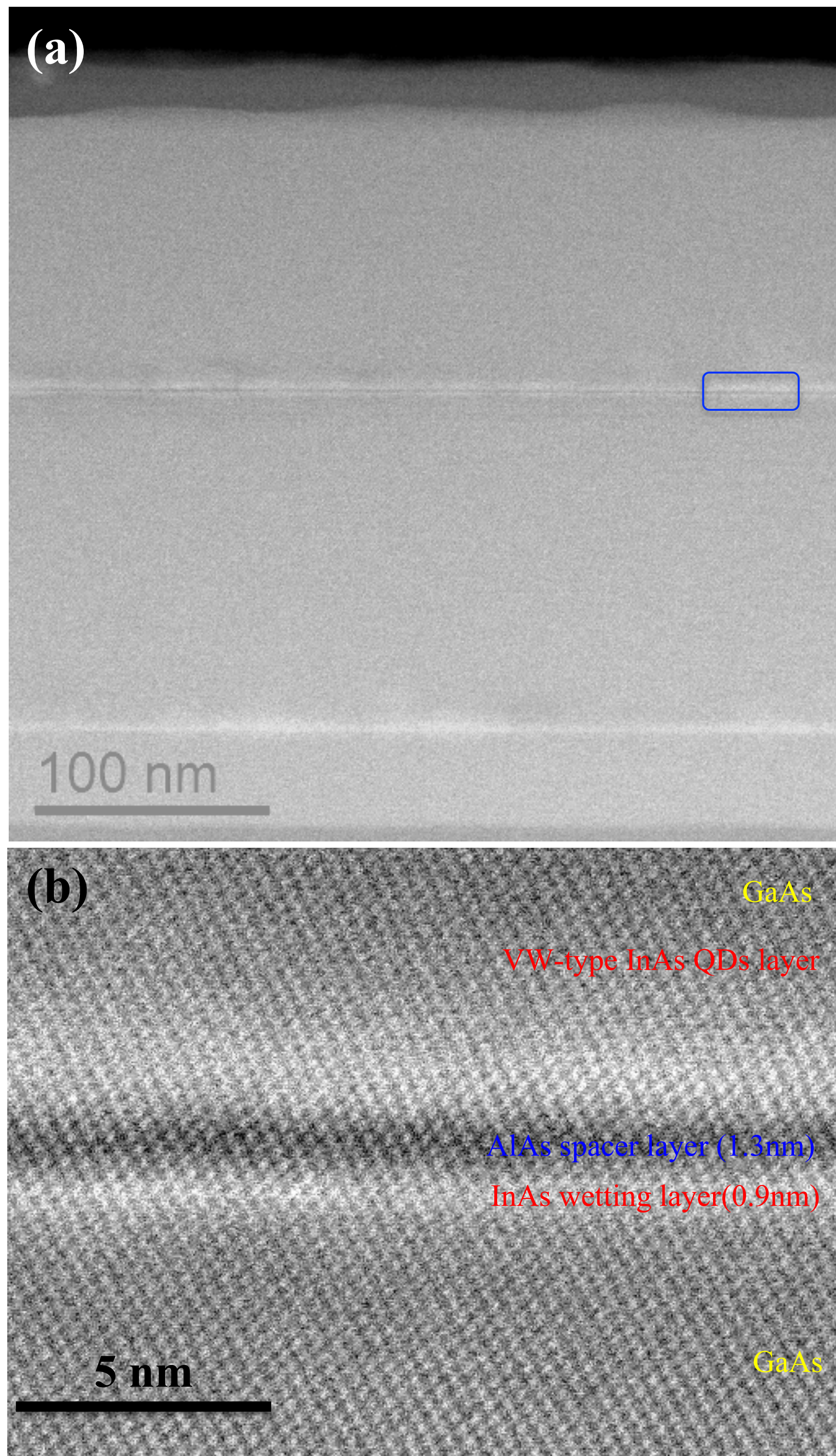


Figure 6.6 (a) Medium-magnification HAADF-STEM image showing the embedded near-wetting layer-free InAs QDs and embedded conventional SK-typed QDs. (b) HAADF-STEM lattice image showing the AlAs spacer layer for near-wetting layer-free InAs QDs.

Figure 6.6 (a) is a medium-magnification HAADF-STEM image showing the two embedded InAs QD layers. This image clearly shows that the second QD layer was incorporated with the AlAs spacer layer, which shows darker contrast in the image. The AlAs spacer layer was much more clearly visible in Fig. 6.6 (b), which is a high-resolution HAADF-STEM lattice image. The thickness of AlAs spacer layer were measured as 1.3 nm on average, and the InAs wetting layer thickness was measured to be 0.9 nm on average. From Fig. 6.6 (a), it seems that the sizes of near-wetting layer-free QDs incorporated with the AlAs spacer layer are smaller than the conventional SK-type QDs. The observation is more obvious in Figs. 6.7 (a-b), which are higher-magnification HAADF images showing near-wetting layer-free QDs (a) and SK-type QDs (b), as marked by the yellow arrows. This observation in HAADF-STEM is consistent with HR-TEM imaging as shown in Fig. 6.4. Besides the size, it also seems that SK-type QDs possess a more well-defined shape compared with near-wetting layer-free QDs, as shown in Fig. 6.7. The SK-type QDs showed triangular shapes, and a similar shape observation was also reported in the research in chapter 5. For near-wetting layer-free In QDs, the shape is flatter.

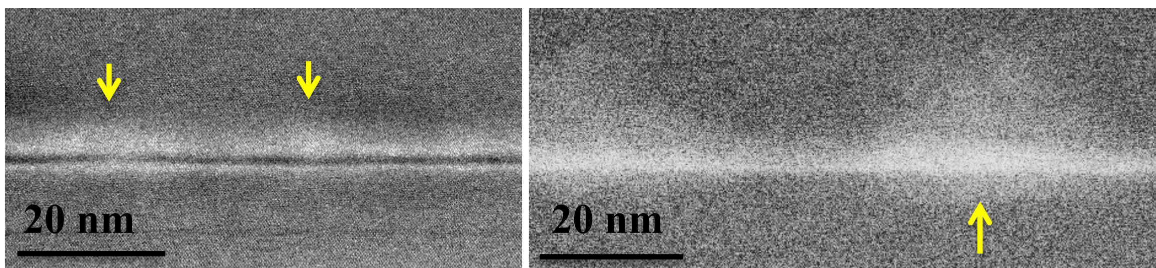


Fig. 6.7 (a) Medium-magnification HAADF-STEM image showing embedded InAs QDs incorporated with AlAs spacer layer. (b) Medium-magnification HAADF-STEM image showing conventional embedded InAs QDs.

TEM characterization was also used to investigate the QD shapes. Figure 6.8 (a) is a diffraction-contract TEM image showing typical near-wetting layer-free InAs QD incorporated with AlAs spacer layer (upper) and conventional SK-type InAs QD (lower), as marked by red arrows. In agreement with the STEM characterization, the sizes of SK-type QDs are larger than near-wetting layer-free QDs. Figure 6.8 (b) is another TEM image showing the SK-type InAs QDs. Besides the <111> stacking faults, dislocations were also observed near the interfaces between InAs and GaAs, which is quite common in many large-lattice-mismatch systems.

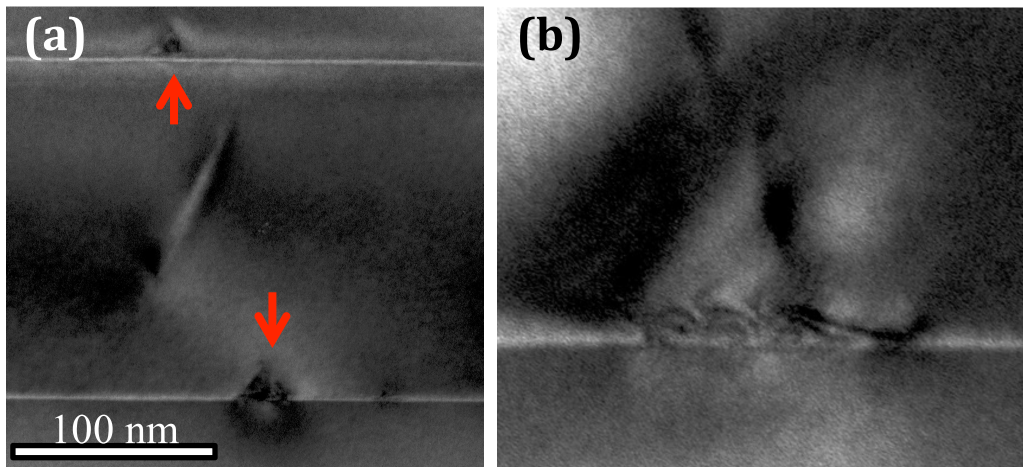


Fig. 6.8 (a) Diffraction-contract TEM image showing typical near-wetting layer-free InAs QD incorporated with AlAs spacer layer (upper) and conventional SK-type InAs QD (lower). (b) TEM image showing a typical conventional SK-type InAs QD with <111> stacking fault and dislocation.

6.2.2 Characterization of InAs QDs incorporating with GaAs spacer layer

The second sample (#2) in this study contained the conventional embedded SK-typed InAs QDs and the near-wetting layer-free InAs QDs incorporated with GaAs spacer layer, as illustrated in Fig. 6.9, which is a structural schematic for this sample. The first QD layer is the layer of conventional InAs QDs without and incorporating spacer layer. Based on the RHEED analysis, this sample incorporated a 1.5 ML of wetting layer

(critical thickness for SK-type QDs) with subsequent growth of about 0.8-0.9 ML equivalent of InAs, which leads to the formation of QDs bounded by {136} or {137} facets. The second layer of QDs was then incorporated with a relatively thick GaAs spacer layer (3 ML), after the deposition of 1.5 ML of InAs. Based on RHEED analysis during growth, this process lead to islands with steeper facets {11n} where 1<n<2. The third layer of QDs contained uncapped InAs QDs incorporated with GaAs spacer layer, which is identical to the second QD layer.

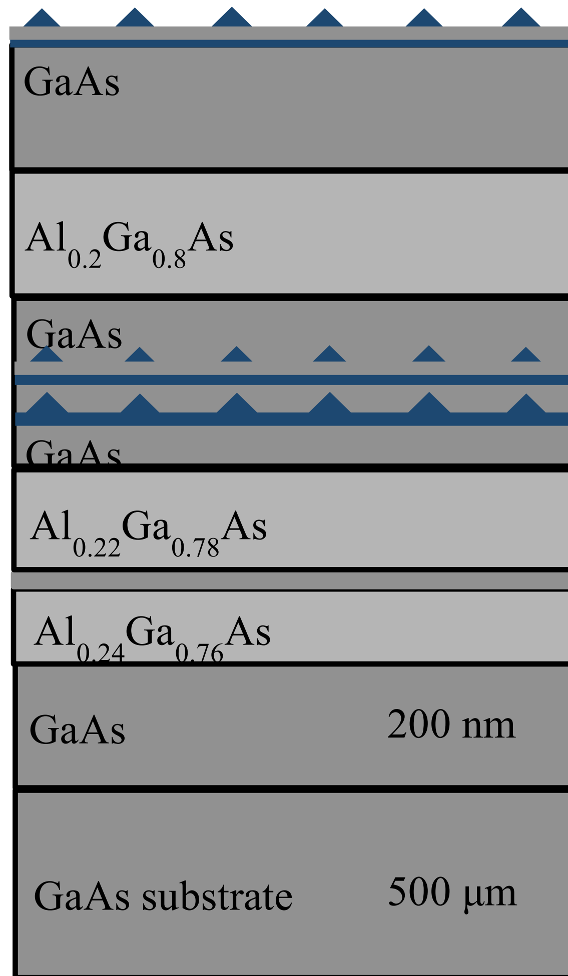


Fig. 6.9 Structural schematic of sample #2 containing embedded VW-type InAs QDs incorporated with GaAs spacer layer, and uncapped VW-type InAs QDs incorporated with GaAs spacer layer.

Figure 6.10 is a low-magnification HAADF-STEM image showing the overall cross-sectional morphology of sample #2. Two embedded InAs-contained layers were observed clearly with the highest contrast. Examining the sample top carefully, it was revealed that many surface bumps appeared on the sample surface, which might indicate the existence of uncapped near-wetting layer-free InAs QDs incorporated with the GaAs spacer layer.

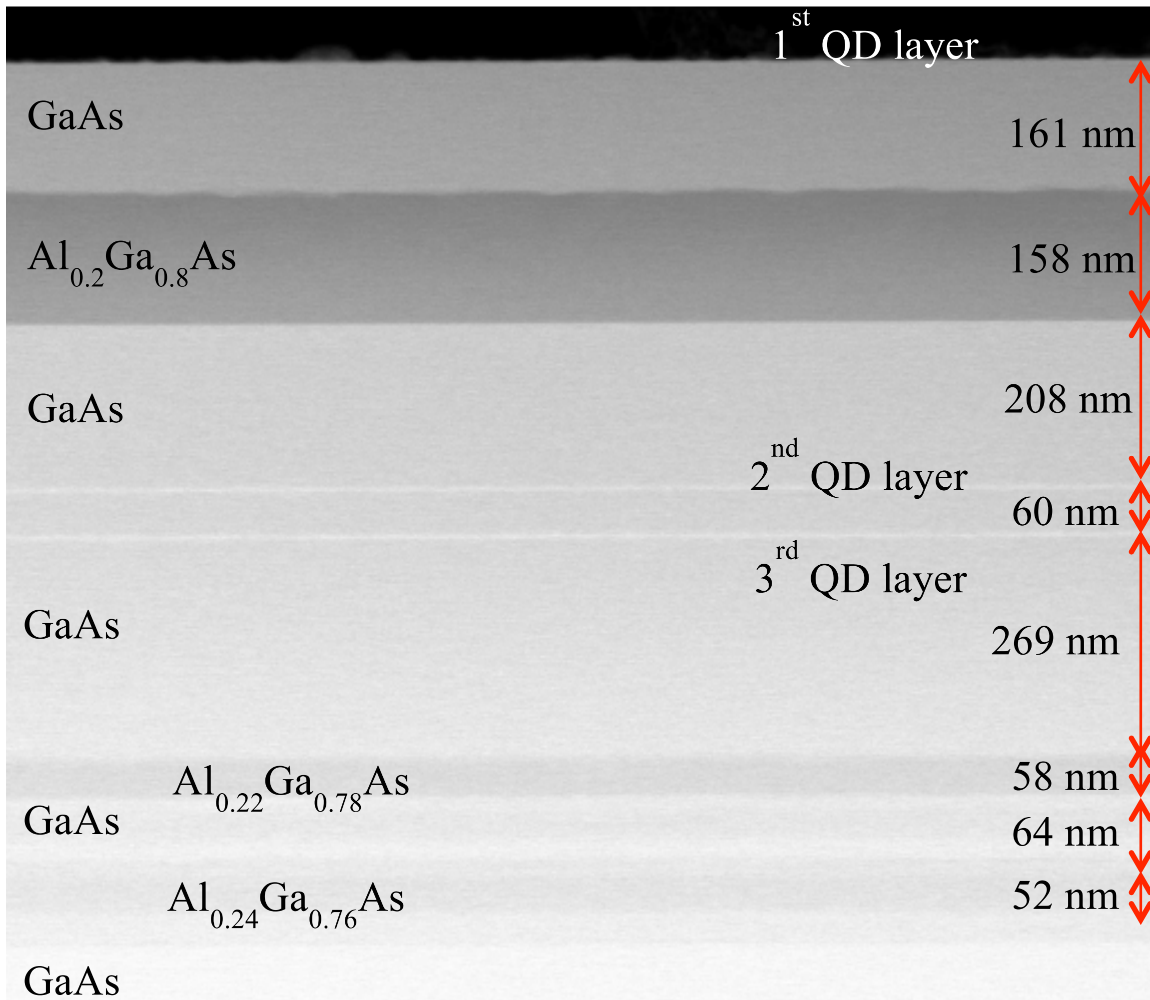


Fig. 6.10 Low-magnification HAADF-STEM image of sample #2 containing embedded VW-type InAs QDs incorporated with GaAs spacer layer, and uncapped VW-type InAs QDs incorporated with GaAs spacer layer.

Figure 6.11 (a) is a HAADF-STEM image showing two embedded InAs QDs, which are conventional SK-type InAs QDs (bottom layer) and near-wetting layer-free QDs incorporating with GaAs spacer layer (upper layer), respectively. Figure 6.11 (b) is the corresponding TEM image in a similar area. The typical QDs were marked by the red arrows, as shown in these two images. From Fig. 6.11 (a), it seemed that the QDs were not obvious on the HAADF-STEM image, although some contrast variations were observed that may indicate the presence of InAs QDs, as labeled by the red arrows. From the TEM image in Fig. 6.11 (b), the presence of QDs was more clear due to strain contrast. Additionally, it seemed that the QD density of the upper embedded layer (near-wetting layer-free InAs QDs incorporating with GaAs spacer layer) was higher than the bottom embedded layer (conventional SK-type InAs QDs), which seems contradictory with the conclusion of QD densities measured by AFM. It needs to be pointed out here that the region of these two layers along the beam direction was relatively very thick because these two layers are buried about half micrometer down from the top surface. Therefore, characterization of these two embedded layers was very difficult. As a result, the presence of GaAs spacer layer was not clear in this area, although the difference in QD morphologies was obvious.

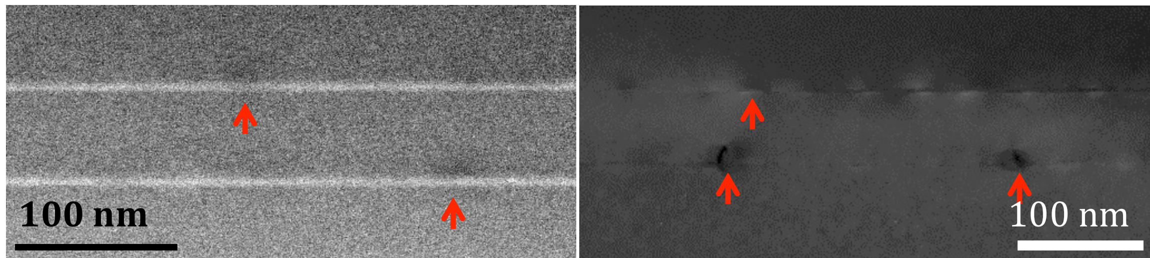


Fig. 6.11 (a) Medium-magnification HAADF-STEM image of embedded InAs QDs. (b) Medium-magnification TEM image of embedded InAs QDs.

Detailed examination of the uncapped near-wetting layer-free InAs QDs incorporated with GaAs spacer layer was performed, as shown in Fig. 6.12 (a), which is a HAADF-STEM image showing the layer of uncapped conventional InAs QDs. A very thin oxide capping layer (~5 nm) was grown on top of the InAs QD layer in order to preserve the QDs, as observed in this image. From this image, it is revealed that the InAs QDs varied in size, as shown in Fig. 6.12 (a-c). This observation is further confirmed by HR-TEM characterization in Fig. 6.13 which will be discussed later. From HAADF-STEM images, the InAs wetting layer was observed, as marked in Fig. 6.12 (a). However, based on both HAADF-STEM and HR-TEM imaging there was again no distinct evidence showing the incorporated GaAs spacer layer. It may be due to the difference in contrast between InAs QDs and GaAs spacer layer is not large enough, which is caused by a small volumetric InAs amount and a large volumetric GaAs amount that resulting in a similar total atomic weight, in the beam direction. Furthermore, according to the previous AFM analysis, it was confirmed that the InAs QDs incorporated with GaAs spacer layers had bimodal size distribution. This observation was confirmed by TEM characterization in both cross-section and plan-view. Figure 6.12 (b) is a HAADF-STEM lattice image showing a typical relatively small InAs QD. Figure 6.12 (c) is another HAADF-STEM lattice image showing a smaller QD overlapping with one or two bigger QDs along the beam direction, which again confirmed the presence of two distinct families of large and small dots. The fact of bimodal size distribution is further confirmed by cross-sectional and plan-view TEM characterization, which are discussed latter.

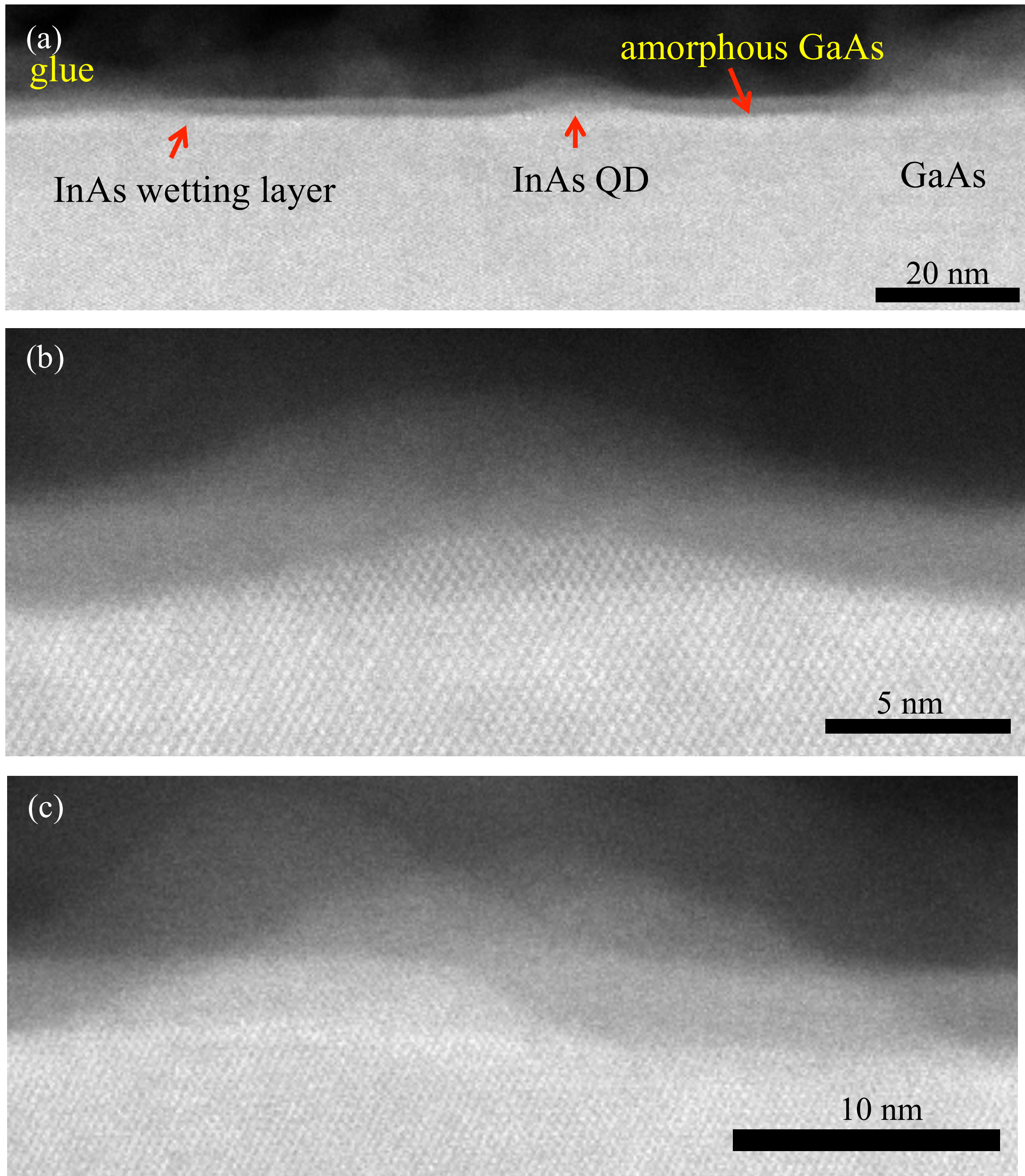


Figure 6.12 (a) HAADF-STEM image showing the uncapped InAs QDs with size variation; (b) HAADF-STEM lattice image showing a typical InAs QD; (c) HAADF-STEM lattice image showing a typical InAs QD overlapping with a bigger QD.

Figure 6.13 (a) is a HR-TEM image showing the uncapped near-wetting layer-free InAs QDs incorporated with GaAs spacer layer, as marked by the red arrows. Two distinct InAs QDs were obvious on this image, which reveals the different sizes. Figure 6.13 (b) is a HR-TEM lattice image showing the left QD from Fig. 6.13 (a), and Fig. 6.13 (c) is a HR-TEM lattice image showing the right QD from Fig. 6.13 (a). From the HR-TEM characterization, it appears that smaller InAs QDs incorporated with GaAs spacer layer had well-defined triangular shapes, but the larger InAs QDs had relatively poorly-defined shapes. It was also noticed that once the QDs became larger, dislocations were always present, as shown in Fig. 6.13 (d) which is an enlarged HR-TEM lattice image from Fig. 6.13 (c) showing a typical dislocation marked by the red arrow.

The plan-view morphology of uncapped near-wetting layer-free InAs QDs incorporated with GaAs spacer layer was also examined by TEM, as shown in Fig. 6.14. Figure 6.14 (a) is a plan-view TEM image showing the uncapped near-wetting layer-free InAs QDs incorporated with the GaAs spacer layer, and Fig. 6.14 (b) is a plan-view HAADF-STEM image showing the uncapped near-wetting layer-free InAs QDs incorporated with the GaAs spacer layer. From these two images, it again shows that these near-wetting layer-free InAs QDs did not possess the same well-defined shape as conventional InAs QDs or other IV-IV QDs. The dislocations were noticed more clearly in these two plan-view images with black contrast in TEM images and white contrast in HAADF-STEM images. Additionally, it again showed the two distinct bimodal size distributions are again apparent consistent with the AFM analysis and cross-sectional TEM characterization. However, the plan-view TEM characterization did not show that

the InAs QDs incorporated with GaAs spacer layer had elongated shapes along [110], as visible in the AFM images.

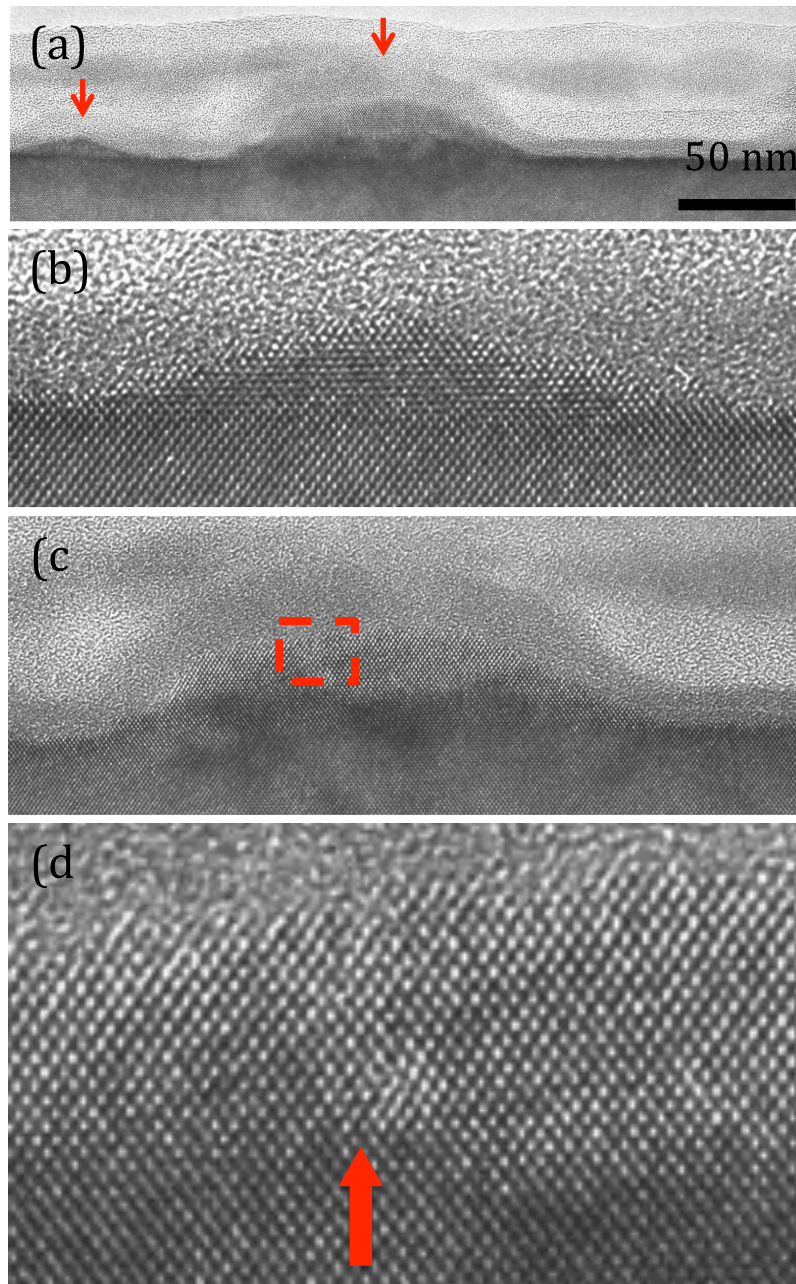


Fig. 6.13 (a) TEM image showing the near-wetting layer-free InAs QDs incorporated with GaAs spacer layer. (b) HR-TEM image showing the left QD on (a). (c) HR-TEM image showing the right QD on (a). (d) HR-TEM image showing a typical dislocation in the larger InAs QDs incorporated with GaAs spacer layer.

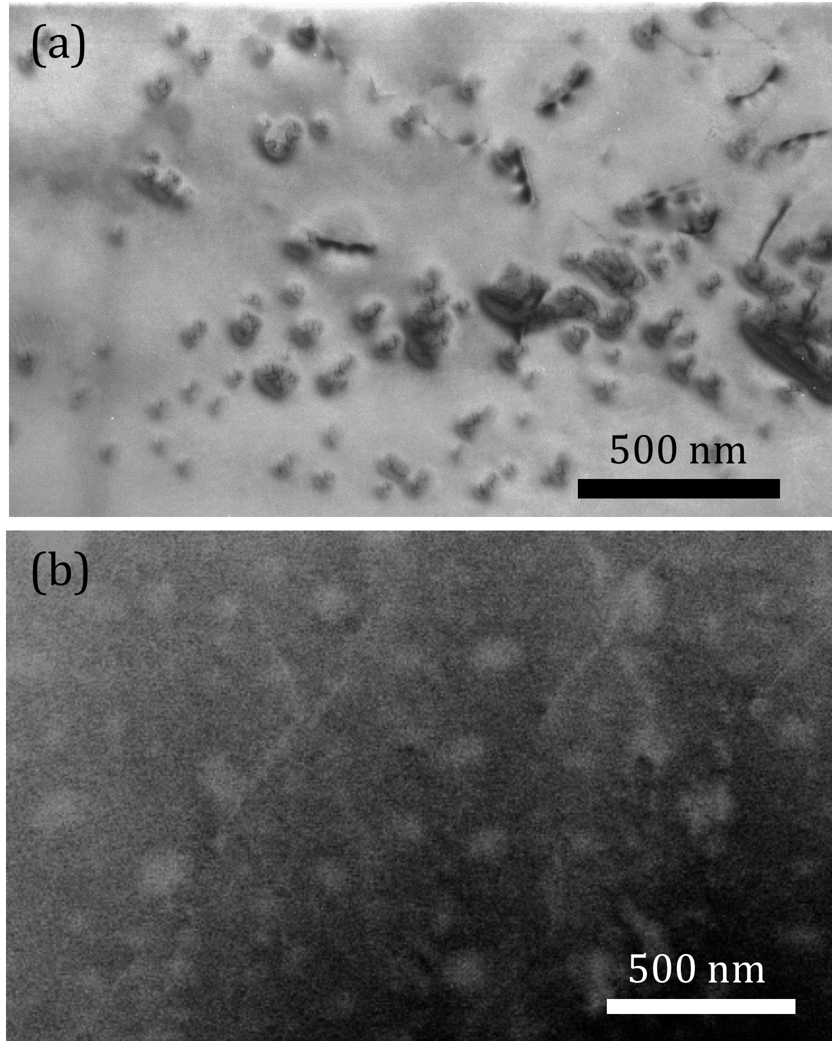


Fig. 6.14 (a) Plan-view TEM image showing the near-wetting layer-free InAs QDs incorporated with GaAs spacer layer. (b) Plan-view HAADF-STEM image showing the near-wetting layer-free InAs QDs incorporated with GaAs spacer layer.

## 6.3 Conclusions

In summary, both embedded near-wetting layer-free InAs QDs incorporated with AlAs/GaAs spacer layers and embedded conventional SK-type InAs QDs were studied. It was found that conventional SK-type InAs QDs had a more well-defined triangular shape and the InAs QDs incorporated with AlAs spacer layer had a relatively non-well-defined shape. According to AFM analysis and plan-view TEM characterization, it was revealed

that InAs QDs incorporated with a spacer layer had smaller dot density and more symmetrical large sizes with bimodal size distribution (two distinct families of large and small dots) compared with the conventional InAs QDs without spacer layer.

REFERENCES

[1] L. Krastanow and I. N. Stranski, Z Kristallogr **99** (5), 444 (1938).

[2] L. Goldstein, F. Glas, J. Y. Marzin, M. N. Charasse, and G. Leroux, Applied Physics Letters **47** (10), 1099 (1985).

[3] R. P. Mirin, J. P. Ibbetson, K. Nishi, A. C. Gossard, and J. E. Bowers, Applied Physics Letters **67** (25), 3795 (1995).

[4] D. L. Huffaker, G. Park, Z. Zou, O. B. Shchekin, and D. G. Deppe, Applied Physics Letters **73** (18), 2564 (1998).

[5] H. Saito, K. Nishi, and S. Sugou, Applied Physics Letters **73** (19), 2742 (1998).

[6] M. Markiewicz and H. Vo, *Electronic states in three dimensional quantum dot/wetting layer structures*, [Elektronische Ressource], preprint (Vorabdruck) ed. (Techn. Univ. Hamburg-Harburg, Hamburg).

[7] H. Z. Song, T. Usuki, Y. Nakata, N. Yokoyama, H. Sasakura, and S. Muto, Physical Review B **73** (11) (2006).

# CHAPTER 7

# SUMMARY AND FUTURE WORK

## 7.1 Summary

The work described in this dissertation has involved extensive structural characterization of MBE-grown II-VI and III-V compound semiconductor quantum dots (QDs), and dilute-nitride $GaAsN_x$-based thin films using transmission electron microscopy (TEM) techniques. Correlation between growth, TEM studies and other techniques, such as XRD and AFM, have been performed in order to determine the structure-growth-performance properties of these materials systems which are intended for photovoltaic applications.

For the II-VI compound QD system, the structural characterization of CdTe QDs grown on ZnTe/GaSb hybrid substrates using the post-annealing MBE approach was systematically studied. The effect of CdTe deposition thickness and ZnTe capping layers were two controlled parameters that were investigated. Extensive analysis of cross-sectional and plan-view micrographs revealed that the shapes of CdTe QDs grown by this method were not well-defined, regardless of the amount of CdTe deposition and use of ZnTe capping. Thus, the CdTe/ZnTe system resembles former QD studies of the II-VI systems, such as CdSe/ZnSe. However, it was found that the size of the QDs and the density of <110> stacking faults in the ZnTe capping layer increased with the amount of CdTe deposition. Overall, the structural properties of the CdTe/ZnTe QD system observed in this work strongly indicated that the process of self-assembly of II-VI

semiconductor materials using the post-annealing MBE approach is significantly different from the mechanism prevailing for most III-V and IV-IV materials.

For the dilute-nitride system, microscopic investigations of dilute-nitride alloys of epitaxial $GaAsN_x$ ($0.01<x<0.04$) were performed. The formation of a thin parasitic N-doped layer was observed which was found to be correlated with the plasma ignition process. More important, a significant amount of nitrogen incorporated into the dilute-nitride films was found by Z-contrast imaging to be primarily interstitial, and local nitrogen composition fluctuations also occurred during the dilute-nitride growth. {110}-oriented micro-cracks, which were associated with strain relaxation, were observed in the sample with the highest N concentration ([N]~3.7%). Significant N contamination of the GaAs barrier layers was observed in all samples, and could severely affect the carrier extraction and transport properties of targeted devices based on these materials.

The InAs/GaAsSb QD system was investigated systematically using electron microscopy techniques. The results showed that the GaAsSb barrier layers played an important role in tuning the energy band alignments based on PL results but without changing the overall structural morphology. The evolution of InAs QDs was studied extensively as a function of Sb concentration and the total number of QD layers. The densities of dislocations increased as the number of QD layers built up, according to both XRD measurements and electron microscopy. In addition, the shapes of the InAs QDs evolved from well-defined to not-well defined due to residual strain beneath the QDs, which further generated defects and degraded the optical performance of devices.

The structural properties of near-wetting layer-free InAs QDs incorporated with AlAs/GaAs spacer layer grown by MBE were studied using TEM and STEM, in contrast

with the InAs QDs grown by conventional Stranski-Krastanov (SK) type InAs QDs. It was found that conventional SK-type InAs QDs had a more well-defined triangular shape and the InAs QDs incorporated with AlAs/GaAs spacer layer had a relatively non-well-defined shape. According to AFM analysis and plan-view TEM characterization, it was revealed that InAs QDs incorporated with spacer layers had smaller dot density and more symmetrical large sizes with bimodal size distribution compared with conventional InAs QDs without spacer layers.

## 7.2 Future work

### 7.2.1 Minimization of ion-milling damage and re-deposition during ion-milling

The damage caused by argon ion-milling (dislocations and surface amorphization) has been a critical ongoing issue for atomic-scale electron microscopy of many II-VI and III-V materials, particular for GaAs and ZnTe. Structural damage induced by argon-ion milling was observed in many of the TEM and STEM images presented in this dissertation, even though the samples were milled at relatively low energy (~2.5 keV) and held properly at liquid nitrogen temperature. In order to solve this problem, better ion-milling instruments are needed to satisfy the demand for decent TEM specimens, particular for aberration-corrected electron microscopes that are nowadays in widespread use. For example, Gatan has developed a revolutionary, enhanced Ion-milling system (PIPS II) which has the capability to mill the sample with beam energies as low as 300 eV with a guaranteed stable beam energy and small beam crossover (~ 1 mm). In addition, Fischione provides a much more powerful specimen preparation system called NanoMill (Model 1040) which integrates a basic SEM with gaseous ion sources, that provides ion

energies as low as 50 eV and a beam size as small as 1μm. Ion-milling carried out by these instruments should provide decent TEM specimens that satisfy the demanding sample requirements for modern electron microscopy.

Due to the lengthy ion-milling process caused by using relatively low beam energy and by holding the sample at liquid nitrogen temperature, serious Cu re-deposition occurred easily due to the Cu TEM grids/washers commonly used to mount the sample. The Cu re-deposition often caused difficulties in high-resolution and high-magnification characterization, particular in HAADF-STEM mode, since the Cu nanoparticles gave sharp contrast which made image interpretation more difficult. Although the Cu re-deposition can be removed by low-energy re-milling for a short period, the need for thinning the desired area sometimes ruined the entire TEM sample. Moreover, this re-milling method didn't work particularly well when very serious re-deposition had occurred. TEM grids made of harder materials, such as Mo, are highly recommended to be used, particular for preparing II-VI and III-V samples such as GaAs and ZnTe. The TEM samples prepared for the work in Chapter 5 were glued on Mo TEM grids, which meant that no re-deposition problems ever occurred during ion-milling.

### 7.2.2 Detection and atomic incorporation of nitrogen atoms in dilute-nitride alloys

Crystalline materials containing light elements attract tremendous interest due to the scientific and technological importance. Understanding the mechanism for incorporating N atoms in the dilute-nitride films is essential for film nucleation, which further influences the material properties and device performance. With the development of new instrumental microscopy techniques, light elements, even doped light elements, might be imaged directly by modern TEM, particular using annular BF (ABF) and

monochromatic EELS in aberration-corrected microscopes. Individual N atoms might be detected. Hence, the complete distribution and atomic incorporation of N atoms would be obtained.

### 7.2.3 Interfacial diffusion and intermixing in II-VI and III-V QD systems

In chapters 3, 5 and 6, the structural properties of CdTe/ZnTe, InAs/GaAsSb, and InAs/AlAs/GaAs QD systems, respectively, have been investigated. In chapter 3, it seems that there is Cd interdiffusion in the ZnTe epilayer. And in chapter 5, the interface of GaAsSb deposited on GaAs was revealed to be sharper than the interface of GaAs deposited on GaAsSb due to residual strain. The asymmetry in interface roughness may have a direct impact on the electronic and optical properties of QD-based photovoltaic devices. Thus, systematic studies should be made of the interface roughness and residual strain analysis of these samples.

To determine the interfacial sharpness and to perform accurate strain analysis, aberration-corrected S/TEM should be used since it provides much better capability to resolve individual atomic columns of crystalline materials. The high quality of micrographs obtained by aberration-corrected microscope further ensures strain measurements with spatial resolution down to the sub-nanometer scale. Various strain measurement/mapping techniques have been developed, particular Geometric Phase Analysis (GPA), which is able to achieve strain measurements with good precision and nanometer scale resolution.[1,2] Careful use of the GPA method might provide better insight into the structural properties of II-VI and III-V QD systems.

REFERENCES

[1] M. J. Hytch, E. Snoeck, and R. Kilaas, Ultramicroscopy **74** (3), 131 (1998).

[2] J. L. Rouviere and E. Sarigiannidou, Ultramicroscopy **106** (1), 1 (2005).

LIST OF REFERENCES

J. R. Balfour, M. L. Shaw, and S. Jarosek, *Introduction to photovoltaics*. (Jones & Bartlett Learning, Burlington, 2013).

C. S. Solanki, *Solar photovoltaics : fundamentals, technologies and applications*, Second edition ed. (PHI Learning, New Delhi, 2011).

A. Luque and S. Hegedus, *Handbook of photovoltaic science and engineering*, 2nd ed. (Wiley, Chichester, West Sussex, U.K., 2011).

A. G. Aberle, Thin Solid Films **517** (17), 4706 (2009).

S. K. Deb, Renew Energ **8** (1-4), 375 (1996).

http://www.solarlightaustralia.com.au/.

U. Rau, D. Abou-Ras, T. Kirchartz, and MyiLibrary., (Wiley-VCH,, Weinheim, Germany, 2011).

D. Y. Goswami, F. Kreith, J. F. Kreider, and F. Kreith, *Principles of solar engineering*, 2nd ed. (Taylor & Francis, Philadelphia, PA, 2000).

G. H. Bauer, Appl Surf Sci **70-1**, 650 (1993).

A. Goetzberger and C. Hebling, Sol Energ Mat Sol C **62** (1-2), 1 (2000).

M. Bosi and C. Pelosi, Progress in Photovoltaics: Research and Applications **15** (1), 51 (2007).

M. A. Green, K. Emery, Y. Hishikawa, W. Warta, and E. D. Dunlop, Progress in Photovoltaics: Research and Applications **21** (1), 1 (2013).

A. W. Bett, F. Dimroth, G. Stollwerck, and O. V. Sulima, Appl Phys a-Mater **69** (2), 119 (1999).

M. R. Brozel, G. E. Stillman, and INSPEC (Information service), *Properties of gallium arsenide*, 3rd ed. (INSPEC, London, 1996).

H. M. Manasevit, Journal of Crystal Growth **55** (1), 1 (1981).

D. J. Smith, Journal of Electronic Materials **42** (11), 3168 (2013).

C. S. Ferekides, U. Balasubramanian, R. Mamazza, V. Viswanathan, H. Zhao, and D. L. Morel, Solar Energy **77** (6), 823 (2004).

M. Afzaal and P. O'Brien, Journal of Materials Chemistry **16** (17), 1597 (2006).

J. Venables, *Introduction to surface and thin film processes*. (Cambridge University Press, Cambridge, UK ; New York, 2000).

http://en.wikipedia.org/wiki/Stranski-Krastanov_growth.

K. Oura, V. G. Lifshits, A. A. Saranin, A. V. Zotov, and M. Katayama, *Surface science : an introduction*. (Springer, Berlin etc., 2010).

A. Pimpinelli and J. Villain, *Physics of crystal growth*. (Cambridge University Press, Cambridge, 1998).

K. Oura, *Surface science : an introduction*. (Springer, Berlin ; New York, 2003).

J. R. Arthur, Surf Sci **500** (1-3), 189 (2002).

K. Seshan, *Handbook of thin-film deposition processes and techniques : principles, methods, equipment and applications*, 2nd ed. (Noyes Publications / William Andrew Pub., Norwich, N.Y., 2002).

R. E. Pimpinella, A. M. Mintairov, X. Liu, T. H. Kosel, J. L. Merz, J. K. Furdyna, and M. Dobrowolska, J Vac Sci Technol B **29** (3) (2011).

F. Tinjod, B. Gilles, S. Moehl, K. Kheng, and H. Mariette, Applied Physics Letters **82** (24), 4340 (2003).

L. Krastanow and I. N. Stranski, Z Kristallogr **99** (5), 444 (1938).

M. A. Pinault, A. Freundlich, J. A. H. Coaquira, and A. Fotkatzikis, Journal of Applied Physics **98** (2), 023522 (2005).

D. J. Smith, Ultramicroscopy **108** (3), 159 (2008).

D. J. Smith, Microscopy and Microanalysis **14** (1), 2 (2008).

D. J. Smith, Micron **43** (4), 504 (2012).

D. J. Smith, T. Aoki, J. Mardinly, L. Zhou, and M. R. McCartney, Microscopy-Jpn **62**, S65 (2013).

P. R. Buseck, J. M. Cowley, and L. Eyring, *High-resolution transmission electron microscopy and associated techniques*. (Oxford University Press, New York ; Toronto, 1992).

B. R. S.J. Pennycook, P.D. Nellist, Microscopy and Microanalysis **6** (04), 343 (2000).

D. B. Williams and C. B. Carter, *Transmission electron microscopy : a textbook for materials science*, 2nd ed. (Springer, New York, 2008).

S. J. Pennycook and P. D. Nellist, *Scanning transmission electron microscopy : imaging and analysis*. (Springer, New York, 2011).

L. A. Giannuzzi, *Introduction to focused ion beams : instrumentation, theory, techniques, and practice*. (Springer, New York, 2005), p.357 S.

F. Tinjod, B. Gilles, S. Moehl, K. Kheng, and H. Mariette, Appl. Phys. Lett. 82 (2004) 4340.

G. Karczewski, S. Mackowski, M. Kutrowski, T. Wojtowicz, and J. Kossut, Appl. Phys. Lett. 74 (1999) 3011.

Collaboration: Authors and editors of the volumes III/17B-22A-41B: *Cadmium telluride (CdTe) band structure*. Madelung, O., Rössler, U., Schulz, M. (ed.). SpringerMaterials - The Landolt-Börnstein Database (http://www.springermaterials.com). DOI: 10.1007/10681719_621.

S. Wang, D. Ding, X. Liu, X.-B. Zhang, D.J. Smith, J.K. Furdyna, and Y.-H. Zhang, J. Cryst. Growth 311 (2009) 2116.

R. E. Pimpinella, A. M. Mintairov, X. Liu, T. H. Kosel, J. L. Merz, J. K. Furdyna, and M. Dobrowolska, J. Vac. Sci. Technol. B 29 (2011) 03C119.

G. Karczewski, S. Mackowski, M. Kutrowski, T. Wojtowicz and J. Kossut, Appl. Phys. Lett. 74 (1999) 3011.

Y. Terai, S. Kuroda, K. Takita, T. Okuno, and Y. Masomoto, Appl. Phys. Lett. 73 (1998) 3757.

S. Mackowski, G. Karczewski, T. Wojtowicz, J. Kossut, S. Kret, A. Szczepanska and P. Dluzewski, Appl. Phys. Lett. 78 (2001) 3884.

H. Kuwabara, A. Unno, K. Kouga, T. Watanabe, W. Tomoda, Y. Nakanishi, and H. Tatsuoka, Appl. Surf. Sci. 175-176 (2001) 643.

M.S. Jang, S.H. Oh, H.S. Lee, J.C. Choi, H.L. Park, T.W. Kim, D.C. Choo, and D.U. Lee, Appl. Phys. Lett. 81 (2002) 993.

E.H. Lee, K.H. Lee, J.S. Kim, H.L. Park, and T.W. Kim, Appl. Phys. Lett. 83 (2003) 5536.

Y.S. No, T.W. Kim, H.S. Lee, and H.L. Park, Appl. Surf. Sci. 243 (2005) 143.

H.S. Lee, H.L. Park, and T.W. Kim, J. Cryst. Growth 291 (2006) 442.

L. Marsal, L. Besombes, F. Tinjod, K. Kheng, A. Wasiela, B. Gilles, J.-L. Rouviere and H. Mariette, J. Appl. Phys. 91 (2002) 4936.

F. Tinjod, B. Gilles, S. Moehl, K. Kheng, and H. Mariette, Appl. Phys. Lett. 82 (2003) 4340.

R.E. Pimpinella, X. Liu, J. K. Furdyna, M. Dobrowolska, A. M. Mintairov, and J. L. Merz, J. Electron. Mater. 39 (2010) 992.

I.N. Stranski and L. Krastanow, Sitzungsber. Akad. Wiss. Wien, Math.-Naturwiss. Kl., Abt. IIb 146 (1938) 797.

C. Wang, D. J. Smith, S. Tobin, T. Parodos, J. Zhao, Y. Chang, and S. Sivananthan, J. Vac. Sci. Technol. A 24 (2006) 995.

D. J. Smith, D. Chandrasekhar, S. A. Chaparro, P. A. Crozier, J. Drucker, M. Floyd, M.R. McCartney, and Y. Zhang, J. Cryst. Growth 259 (2003) 232.

C.S. Kim, M. Kim, J.K. Furdyna, M. Dobrowolska, S. Lee, H. Rho, L.M. Smith, H. E. Jackson, E.M. James, Y. Xin and N.D. Browning, Phys. Rev. Lett. 85 (2000). 1124.

S.A. Chaparro, Y. Zhang, J. Drucker, D. Chandrasekhar, and D. J. Smith, J. Appl. Phys. 87 (2000) 2245.

T. Xu, L. Zhou, Y. Wang, A. S. Ozcan. K.F. Ludwig, D. J. Smith, and T. D. Moustakas, J. Appl. Phys. 102 (2007) 073517.

G. Pozina, I. Ivanov, B. Monemar, J. V. Thordson, and T. G. Andersson, Journal of Applied Physics **84** (7), 3830 (1998).

S. Zhang and S.-H. Wei, Physical Review Letters **86** (9), 1789 (2001).

M. Weyers and M. Sato, Applied Physics Letters **62** (12), 1396 (1993).

Y. Zhang, A. Mascarenhas, H. Xin, and C. Tu, Physical Review B **63** (16), 161303 (2001).

K. Uesugi, N. Morooka, and I. Suemune, Applied Physics Letters **74** (9), 1254 (1999).

U. Tisch, E. Finkman, and J. Salzman, Applied Physics Letters **81** (3), 463 (2002).

T. Taliercio, R. Intartaglia, B. Gil, P. Lefebvre, T. Bretagnon, U. Tisch, E. Finkman, J. Salzman, M. A. Pinault, M. Laügt, and E. Tournié, Physical Review B **69** (7), 073303 (2004).

V. Virkkala, V. Havu, F. Tuomisto, and M. J. Puska, Physical Review B **88** (3) (2013).

A. Freundlich, A. Fotkatzikis, L. Bhusal, L. Williams, A. Alemu, W. Zhu, J. A. H. Coaquira, A. Feltrin, and G. Radhakrishnan, Journal of Crystal Growth **301-302**, 993 (2007).

M. A. Green, K. Emery, Y. Hishikawa, W. Warta, and E. D. Dunlop, Progress in Photovoltaics: Research and Applications **20** (1), 12 (2012).

W. Li, M. Pessa, J. Toivonen, and H. Lipsanen, Physical Review B **64** (11), 113308 (2001).

D. Kwon, R. J. Kaplar, S. A. Ringel, A. A. Allerman, S. R. Kurtz, and E. D. Jones, Applied Physics Letters **74** (19), 2830 (1999).

S. Y. Xie, S. F. Yoon, and S. Z. Wang, Journal of Applied Physics **97** (7), 073702 (2005).

S.J. Pennycook, P.D. Nellist, Microscopy and Microanalysis **6** (04), 343 (2000).

M. A. Pinault, A. Freundlich, J. A. H. Coaquira, and A. Fotkatzikis, Journal of Applied Physics **98** (2), 023522 (2005).

C. Wang, D. J. Smith, S. Tobin, T. Parodos, J. Zhao, Y. Chang, and S. Sivananthan, Journal of Vacuum Science & Technology A: Vacuum, Surfaces, and Films **24** (4), 995 (2006).

W. J. Fan, S. F. Yoon, W. K. Cheah, W. K. Loke, T. K. Ng, S. Z. Wang, R. Liu, and A. Wee, Journal of Crystal Growth **268** (3-4), 470 (2004).

G. K. Vijaya, A. Freundlich, D. Tang, and D. J. Smith, Jour. Vac. Sco. Tech. B (2014), Submitted.

X. Wu, M. D. Robertson, J. A. Gupta, and J. M. Baribeau, Journal of Physics: Condensed Matter **20** (7), 075215 (2008).

T. Grieb, K. Muller, R. Fritz, M. Schowalter, N. Neugebohrn, N. Knaub, K. Volz, and A. Rosenauer, Ultramicroscopy **117**, 15 (2012).

D. D. Perovic, C. J. Rossouw, and A. Howie, Ultramicroscopy **52** (3-4), 353 (1993).

S. G. Spruytte, M. C. Larson, W. Wampler, C. W. Coldren, H. E. Petersen, and J. S. Harris, Journal of Crystal Growth **227-228**, 506 (2001).

M. Herrera, Q. Ramasse, D. Morgan, D. Gonzalez, J. Pizarro, A. Yáñez, P. Galindo, R. Garcia, M. H. Du, S. Zhang, M. Hopkinson, and N. Browning, Physical Review B **80** (12), 125211 (2009).

S. Chung, Characterization of electrostatic potential of compound semiconductors using off-axis electron holography (2009).

L Li, Determination of electrostatic potential and charge distribution of semiconductor nanostructures using off-axis electron holography (2011).

A. Luque and A. Marti, Physical Review Letters **78** (26), 5014 (1997).

A. Luque, A. Marti, and L. Cuadra, IEEE T Electron Dev **48** (9), 2118 (2001).

W. Shockley and H. J. Queisser, Journal of Applied Physics **32** (3), 510 (1961).

A. Marti, L. Cuadra, and A. Luque, IEEE T Electron Dev **48** (10), 2394 (2001).

S. Tomic, T. S. Jones, and N. M. Harrison, Applied Physics Letters **93** (26) (2008).

A. Marti, E. Antolin, C. R. Stanley, C. D. Farmer, N. Lopez, P. Diaz, E. Canovas, P. G. Linares, and A. Luque, Physical Review Letters **97** (24) (2006).

P. G. Linares, A. Marti, E. Antolin, and A. Luque, Journal of Applied Physics **109** (1) (2011).

V. Popescu, G. Bester, M. C. Hanna, A. G. Norman, and A. Zunger, Physical Review B **78** (20) (2008).

Q. Shao, A. A. Balandin, A. I. Fedoseyev, and M. Turowski, Applied Physics Letters **91** (16) (2007).

M. Y. Levy and C. Honsberg, IEEE T Electron Dev **55** (3), 706 (2008).

K.-Y. Ban, D. Kuciauskas, S. P. Bremner, and C. B. Honsberg, Journal of Applied Physics **111** (10), 104302 (2012).

K. Akahane, N. Yamamoto, and N. Ohtani, Physica E **21** (2-4), 295 (2004).

H. Y. Liu, M. J. Steer, T. J. Badcock, D. J. Mowbray, M. S. Skolnick, P. Navaretti, K. M. Groom, M. Hopkinson, and R. A. Hogg, Applied Physics Letters **86** (14) (2005).

K.-Y. Ban, S. P. Bremner, G. Liu, S. N. Dahal, P. C. Dippo, A. G. Norman, and C. B. Honsberg, Applied Physics Letters **96** (18), 183101 (2010).

L. Krastanow and I. N. Stranski, Z Kristallogr **99** (5), 444 (1938).

L. Goldstein, F. Glas, J. Y. Marzin, M. N. Charasse, and G. Leroux, Applied Physics Letters **47** (10), 1099 (1985).

R. P. Mirin, J. P. Ibbetson, K. Nishi, A. C. Gossard, and J. E. Bowers, Applied Physics Letters **67** (25), 3795 (1995).

D. L. Huffaker, G. Park, Z. Zou, O. B. Shchekin, and D. G. Deppe, Applied Physics Letters **73** (18), 2564 (1998).

H. Saito, K. Nishi, and S. Sugou, Applied Physics Letters **73** (19), 2742 (1998).

M. Markiewicz and H. Vo*, *Electronic states in three dimensional quantum dot/wetting layer structures*, [Elektronische Ressource], preprint (Vorabdruck) ed. (Techn. Univ. Hamburg-Harburg, Hamburg).

H. Z. Song, T. Usuki, Y. Nakata, N. Yokoyama, H. Sasakura, and S. Muto, Physical Review B **73** (11) (2006).

M. J. Hytch, E. Snoeck, and R. Kilaas, Ultramicroscopy **74** (3), 131 (1998).

J. L. Rouviere and E. Sarigiannidou, Ultramicroscopy **106** (1), 1 (2005).